IMPERIAL

Investigation of the Limit-Stable Operating Conditions of Centrifugal Turbocharger Compressors

David Schwarz

London, October 2025

Supervised by Professor Ricardo Martinez-Botas

Imperial College London
Department of Mechanical Engineering

A thesis submitted for the degree of
Doctor of Philosophy
and
Diploma of Imperial College

"It is the glory of God to conceal a thing:
but the honour of kings is to search out a matter."

-Proverbs 25:2-

Declaration of Originality

I, Mr. David Schwarz, declare that this PhD thesis is my own work. Where appropriate, citations are included to acknowledge the work of others.

Signature Place, Date

Copyright Declaration

The copyright of this thesis rests with the author. Unless otherwise indicated, its contents are licensed under a Creative Commons Attribution-Non Commercial 4.0 International Licence (CC BY-NC). Any third-party copyright material remains the property of its respective owner(s) and is licensed under its existing terms.

Under this licence, you may copy and redistribute the material in any medium or format. You may also create and distribute modified versions of the work. This is on the condition that: you credit the author and do not use it, or any derivative works, for a commercial purpose.

When reusing or sharing this work, ensure you make the licence terms clear to others by naming the licence and linking to the licence text. Where a work has been adapted, you should indicate that the work has been changed and describe those changes.

Please seek permission from the copyright holder for uses of this work that are not included in this licence or permitted under UK Copyright Law.

Acknowledgements

First and foremost, I would like to express my deepest gratitude to my supervisor, Professor Ricardo Martinez-Botas, for giving me the opportunity to pursue this PhD. His continuous support, insightful discussions, and understanding have been invaluable throughout this journey.

I am also sincerely thankful to my internal supervisor and former manager at DT AG, Dr. Galin Nakov. Working with him has been a true pleasure- his enthusiasm for turbomachinery and good humor made the work not only productive but genuinely enjoyable.

Special thanks go to my colleagues at DT AG: Matthias, Clemens, Jens and Michael. It was a real pleasure working with you and I am very thankful for all the discussions we had and the insights you shared.

I would also like to thank the test bench engineers Chris Noon from ICL and Alexander Schuch from DT AG. Thank you for helping me carry out all the shenanigans on your rigs. Without your support, none of this would have been possible. I also extend my appreciation to the test bench operators Ercan, Andreas, and Naser, who endured the long hours and large data testing alongside me.

I am grateful to the CFD department at DTICI for their continuous support and dedication in setting up the simulations. Vivek, Tom, and Soma- you rock!

To all the amazing people I've met along the way and who have become good friends- thank you. To everyone in CAGB 676 and Building 128, I'm grateful for your support, the engaging discussions, the laughter, and the fun we shared.

And finally, Anni- thank you for your loving support, your help, and for saying yes. I am so thankful to have you by my side.

Abstract

Turbochargers are a key component to achieve today's challenging requirements for commercial vehicle engines. They recover energy from the exhaust gases and supply denser air to the engine, improving efficiency and thus reducing fuel consumption. CO2 and emission regulations and the challenging customer demands require highest turbo efficiency and broad operating range.

Three of the most crucial design targets for turbochargers are: efficiency and pressure ratio for optimal performance and fuel economy, maximum choke mass flow for brake performance, and sufficient surge margin to allow safe engine operation.

While compressor performance at design conditions and close to choke can be predicted with reasonable accuracy, predicting surge remains challenging. This introduces significant risk in compressor development, often leading to application of conservative design rules, limiting the theoretically achievable performance. Therefore, a comprehensive understanding of surge is crucial.

In this work, surge is first investigated on component level using a validated URANS simulation. Findings indicate that a combination of diffuser stall and disturbed inlet flow conditions due to the ported shroud is the surge trigger.

Subsequently, the system level is examined by considering pulsating environments and engine operation, with experiments conducted on a hot gas test rig and an engine test rig. Results show that surge margin shifts are heavily dependent on operating conditions and specific compressor design features. These findings reconcile seemingly contradictory results in literature and bridge the gap between industry experience and academic research.

Finally, the findings are integrated into a fully automated compressor optimization scheme that considers all thermodynamic aspects of compressor performance. The optimization process yields superior results compared to the previous design, significantly enhancing efficiency while improving map width.

This work adresses a critical gap in compressor development, contributing to more efficient and cleaner engines and provides an experimental foundation for future research in transient environments.

Contents

List of Figures V

List of Tables IX

Nomenclature XI

1. Introduction 1

1.1. Turbocharged Engine . . . 1
1.2. Thermodynamic Requirements of a Turbocharger Compressor . . . 2
1.3. Compressor Prediction Limitations . . . 4
1.4. Research Aim and Objectives . . . 4
1.5. Structure of the Work . . . 5

2. Fundamental Knowledge 7

2.1. Fundamentals of Fluid Mechanics . . . 7
2.1.1. Conservation Equations . . . 8
2.1.2. Laminar and Turbulent Flows . . . 9
2.1.3. Boundary Layers . . . 10
2.2. Fundamentals of Turbomachinery . . . 11
2.2.1. Fundamentals of Radial Compressors . . . 11
2.2.2. Thermodynamic Parameters . . . 13
2.2.3. Fundamentals of Commercial Vehicle Exhaust Gas Turbochargers . . . 15
2.3. Fundamentals of Stall and Surge in Centrifugal Compressors . . . 16
2.3.1. Compressor Stall . . . 17
2.3.2. Compressor Surge . . . 19
2.3.3. Surge in Transient Environments . . . 22
2.3.4. Operating Range Enhancement . . . 23
2.4. Fundamentals of Design Optimization . . . 25
2.4.1. Design of Experiments . . . 25
2.4.2. Training Data Acquisition . . . 26
2.4.3. Model Identification and Validation (Metamodelling) . . . 27
2.4.4. Optimization Methodologies . . . 28

3. Methods 31

3.1. Testing . . . 31
3.1.1. Hot Gas Test Rig . . . 31
3.1.2. Electric Test Rig . . . 32
3.1.3. Engine Test Rig . . . 33
3.2. Computational Fluid Dynamics . . . 34
3.2.1. Reynolds Averaging . . . 34
3.2.2. Turbulence Models . . . 35
3.2.3. Discretization and Computational Grid . . . 36

3.2.4. Rotor Interaction and Interfaces . . . 38
3.2.5. Boundary Conditions . . . 38
3.2.6. Transient Simulation . . . 39

4. Analysis of the Surge Trigger of a High-Performance Compressor 41
4.1. Compressor Design . . . 41
4.1.1. Hardware Setup . . . 42
4.2. Validation of the URANS Setup . . . 43
4.2.1. Grid Independence Study . . . 43
4.2.2. Comparison with Electric Test Rig Data . . . 43
4.2.3. Comparison with HGTR Data . . . 46
4.3. Analysis of the Surge Trigger Mechanism . . . 46
4.3.1. Physical Evaluation and Comparison with Literature . . . 46
4.3.2. Conclusion . . . 52
4.4. Compressor Improvement Recommendations . . . 53
4.4.1. Ported Shroud . . . 53
4.4.2. Impeller Optimization . . . 53
4.4.3. Diffuser Optimization . . . 56
4.4.4. Volute Optimization . . . 56
4.5. Addendum: Investigation of Automated Surge Trigger Detection . . . 58
4.5.1. Backflow Method . . . 59
4.5.2. Entropy-based Methods . . . 59
4.5.3. Stability Parameter Method . . . 60
4.5.4. Conclusion . . . 62
4.6. Summary . . . 62

5. Compressor Operation in Transient Environments 65
5.1. Compressor Geometries . . . 65
5.2. Measurements with the Pulsating Flow Device . . . 65
5.2.1. Surge Margin Shift Definitions . . . 67
5.2.2. Influence of a Ported Shroud . . . 68
5.2.3. Influence of Orifice Size on Vaned and Vaneless Diffuser Type Compressors . . . 69
5.2.4. Pulsation Influence . . . 71
5.2.5. Summary . . . 73
5.3. Characterization of the Engine Test Rig Environment . . . 74
5.3.1. Engine Hardware . . . 74
5.3.2. Surge Testing Procedure . . . 75
5.3.3. Effects of the Surge Testing Procedure on the Compressor Operating Point . . . 75
5.4. Conclusions . . . 77

6. Reduced Order Modeling and Optimization 79
6.1. Compressor Performance Prediction Model . . . 80
6.1.1. Pressure Ratio Surrogate Model Stabilization . . . 80
6.1.2. Analytical Extrapolation . . . 83
6.1.3. Efficiency Modeling . . . 84
6.1.4. Validation of the Methodology . . . 85
6.1.5. Suitability for Prediction . . . 87
6.1.6. Addendum: Detection of Erroneous Geometry and Test Bench Stall by the Compressor Performance Prediction Model . . . 89
6.1.7. Summary . . . 92
6.2. 1D System Model . . . 93
6.2.1. Compression System 1D Modeling Approach . . . 93
6.2.2. Model Data Acquisition . . . 98
6.2.3. Comparison of Measurements with Surge Calculations . . . 101
6.2.4. Summary . . . 103
6.3. Surge Feedback for Surrogate-Model-Based Compressor Design Approaches 103
6.3.1. Surge Feedback Methodology . . . 104
6.3.2. Optimization Convergence . . . 106
6.3.3. Design Selection . . . 108
6.3.4. FEA Evaluation . . . 110
6.3.5. Measurements at the HGTR: Optimization Outcome . . . 111
6.3.6. Comparison with an Unconstrained Optimization Run . . . 115
6.3.7. Summary . . . 117
6.4. Design Space Investigation and Manual Optimization . . . 117
6.5. Conclusion . . . 121

7. Summary 123

Bibliography 131

A. Radial Equilibrium Theory 143

B. Program Flow Chart- Compressor Performance Prediction Surrogate Model 145

C. False Color Comparison G1849, G675 146

List of Figures

1.1. functional principle of an exhaust-gas turbocharger . . . 1
1.2. requirements of a turbocharger compressor . . . 3

2.1. laminar and turbulent flow field . . . 9
2.2. boundary layer transition . . . 10
2.3. fundamental velocity considerations . . . 12
2.4. compressor map . . . 15
2.5. cross-section of a turbocharger . . . 16
2.6. stall and surge in compressors . . . 16
2.7. basic stall principles . . . 17
2.8. surge event . . . 19
2.9. Greitzer compression system . . . 20
2.10. pulsating flow device [1] . . . 22
2.11. ported shroud . . . 23
2.12. DoE methods . . . 26
2.13. optimization algorithms . . . 29

3.1. hot gas test rig . . . 32
3.2. electric test rig . . . 33
3.3. engine test rig . . . 34
3.4. near wall modeling . . . 37
3.5. CFD mesh . . . 38

4.1. fluid volume compressor B . . . 42
4.2. hardware compressor B . . . 42
4.3. time step independence study . . . 43
4.4. steady static pressure, diffuser hub . . . 44
4.5. comparison of test and URANS transient pressure data . . . 45
4.6. comparison between URANS and test- diffuser sensor . . . 45
4.7. instantaneous velocity fields . . . 47
4.8. instantaneous static pressure fields . . . 47
4.9. exducer stall . . . 48
4.10. instantaneous mass flow rate during stall . . . 49
4.11. exducer stall inception . . . 49
4.12. relevant flow fields for investigation of flow structure "b" . . . 50
4.13. origin and formation of flow feature "b" . . . 51
4.14. surge trigger mechanism . . . 52
4.15. flow incidence angle at s.b. leading edge . . . 55
4.16. volute improvement, RANS result . . . 57
4.17. volute recirculation channel . . . 58
4.18. entropy-based surge detection . . . 60
4.19. transient SP plot . . . 61

5.1. comparison of compressors B, V . . . 66
5.2. HGTR with PFD . . . 66
5.3. definition of absolute and corrected surge margin shift . . . 67
5.4. absolute and corrected surge margin shift of compressors with ported shroud 68
5.5. absolute and corrected surge margin shift of compressors with and without ported shroud . . . 69
5.6. influence of pulsation amplitude on surge margin shift . . . 70
5.7. influence of pulsation on surge margin . . . 71
5.8. influence of pulsation on surge margin - heatmap . . . 72
5.9. OM471 test engine . . . 74
5.10. change of operating conditions during engine surge testing . . . 75
5.11. crankshaft resolved p_2 at ETR . . . 76

6.1. reduced order modeling and optimization approach . . . 79
6.2. comparison of compressors A, B . . . 80
6.3. test data and surrogate model- compressor A . . . 81
6.4. surrogate model optimization procedure . . . 82
6.5. constrained and coupled surrogate models- compressor A . . . 84
6.6. shaft work surrogate model and HGTR measurement . . . 85
6.7. surrogate model regression and HGTR result- pressure ratio, compressor A . 86
6.8. surrogate model regression and HGTR result- efficiency, compressor A 87
6.9. surrogate model prediction and HGTR result- pressure ratio, compressor B . 88
6.10. surrogate model prediction and HGTR result- efficiency, compressor B 89
6.11. HGTR result: erroneous hardware, compressor B . . . 90
6.12. impeller GOM scan . . . 90
6.13. HGTR result: new impeller, compressor B . . . 91
6.14. Turbodyna 1D domain . . . 95
6.15. Turbodyna: mass flow sensitivity on shaft work . . . 97
6.16. data samples for outlet throttle characterization . . . 100
6.17. measured vs. calculated surge mass flow . . . 102
6.18. surge constraint compressor optimization scheme . . . 104
6.19. CFD domains for the upper and lower limit case of the design space . . . 106
6.20. surge constraint optimization convergence -constraints and objectives 107
6.21. surge constraint optimization convergence - parameters . . . 108
6.22. 3D Pareto front and 2D projections . . . 109
6.23. comparison of compressor B, G1849 and G675 . . . 109
6.24. FEA analysis: principal stresses G1849 at maximum speed . . . 110
6.25. Campbell diagram of G1849 . . . 111
6.26. compressor map G1849 . . . 113
6.27. difference map: G1849 - compressor B, absolute values . . . 113
6.28. compressor map G675 . . . 114
6.29. difference map: G675 - compressor B, absolute values . . . 114
6.30. comparison of different design methods . . . 115
6.31. efficiency comparison - G1849, G675, comp. B* . . . 116

6.32. compressor map compressor C 119
6.33. difference map: compressor C - compressor B, absolute values 120
6.34. manual optimization improvements 121

B.1. program flow chart 145

C.1. false color comparison G1849 Prototype vs. CAD 146
C.2. false color comparison G675 Prototype vs. CAD 146

List of Tables

4.1. URANS simulatuation - relevant time steps 46
4.2. RANS results of impeller splitter blade optimization 54

6.1. optimization objectives and constraints 105
6.2. specification of the design space 106
6.3. geometry parameters G1849, G675 110
6.4. map width defining points - optimization results 112
6.5. geometry parameters compressor C 119

Nomenclature

Abbreviations

EGR Exhaust Gas Recirculation

BC Boundary Condition

CFD Computational Fluid Dynamics

CPU Central Processing Unit

DES Detached Eddy Simulation

DoE Design of Experiments

ETR Engine Test Rig

FFT Fast Fourier Transformation

FVM Finite Volume Method

HGTR Hot Gas Test Rig

LES Large Eddy Simulation

MRF Moving Reference Frame

NLPQL Nonlinear Programming by Quadratic Lagrangian

ODE Ordinary Differential Equation

PDE Partial Differential Equation

PFD Pulsating Flow Device

PIV Particle Image Velocimetry

RANS Reynolds-Averaged Navier Stokes

RET Radial Equilibrium Theory

RSM Reynolds Stress Model

URANS Unsteady Reynolds-Averaged Navier Stokes

Greek Letters

α	absolute flow angle	deg
β	relative flow angle	deg
ϵ	dissipation rate	$\frac{m^2}{s^3}$
η	efficiency	$-$
λ	thermal conductivity	$\frac{W}{mK}$

μ	dynamic viscosity	$\frac{kg}{ms}$
ν	kinetic viscosity	$\frac{m^2}{s}$
ν_T	eddy viscosity	$\frac{m^2}{s}$
ω	turbulent characteristic frequency; angular velocity	s^{-1}
Φ	non-dimensional pressure ratio	–
Π	pressure ratio	–
Ψ	non-dimensional mass flow	–
ρ	density	$\frac{kg}{m^3}$
τ	shear stress; time constant (Greitzer model)	$\frac{N}{m^2}$ / -

Latin Letters

A	area	m^2
a	speed of sound	$\frac{m}{s}$
B	Greitzer stability parameter	–
c	velocity; Buehler et al. model: quasi-steady compressor characteristic	$\frac{m}{s}$ / $\frac{s}{kg}$
c_p	specific heat capacity	$\frac{J}{kgK}$
CoD	coefficient of determination	–
CoP	coefficient of prognosis	–
e	internal energy	$\frac{J}{kg}$
F	force	N
f	frequency	Hz
g	gravitational acceleration; Buehler et al. model: quasi-steady throttle characteristic	$\frac{m}{s^2}$ / $\frac{s}{kg}$
h	specific enthalpy	$\frac{J}{kg}$
k	turbulent kinetic energy	$\frac{J}{kg}$
l, L	length	m
M	torsional moment	Nm
Ma	Mach number	–
n	rotational speed	$\frac{1}{s}$
p	pressure	Pa

R	ideal gas constant	$\frac{J}{K \cdot mol}$
r	radius	m
Re	Reynolds number	–
sm	surge margin	$\frac{kg}{s}$
SP	stability parameter	–
SS_E	sum of squares (error)	–
SS_T	sum of squares (total)	–
T	temperature	K
t	time	s
u, v, w	velocity	$\frac{m}{s}$
V	volume	m^3
W_{shaft}	shaft work	W
x, y	spatial direction	m
Y	specific work	$\frac{m^2}{s^2}$
$y+$	non-dimensional wall distance	–
b	width	m
Cp	static pressure recovery coefficient	–
s	specific entropy	$\frac{J}{kgK}$

Subscripts

1	inlet domain of control volume
2	outlet domain of control volume
c	compressor
is	isentropic
m	meridional
p	plenum
qs	quasi-steady
ref	referenced
S	static
T	total
t	throttle

1. Introduction

With the increasing globalization and technological advancements worldwide, the demand for transporting goods has become increasingly critical. Between 2015 and 2024, the total transported mass increased by a factor of 1.7, reaching 92.1 billion tonnes [2]. Projections for global road transport indicate a sixfold increase from 2010 to 2050 [3]. Even in heavily industrialized countries like Germany, the logistics sector, measured by revenue, ranks second, surpassing both the engineering and chemical industries [4].

Given the sector's dominance, it exerts significant economic and environmental impacts. Since the transported weight is directly proportional to the energy required for movement, even marginal improvements in engine efficiency can yield substantial benefits. Consequently, the development of heavy-duty commercial vehicle engines has become one of the most challenging fields, with manufacturers striving to optimize fuel consumption and durability, while minimizing emissions of carbon dioxide, NOx, fine particulates, and other pollutants.

As a result, turbochargers have become an essential component of diesel engine design. Currently, turbocharged engines have achieved complete market penetration in the medium- and heavy-duty segments [5, 6].

1.1. Turbocharged Engine

The functional principle of an exhaust gas turbocharger is shown in Figure 1.1. Turbocharging enhances engine performance in two ways: it increases the oxygen available for combustion and provides higher inlet pressure (I), and recovers energy from exhaust gases that would otherwise be lost (II).

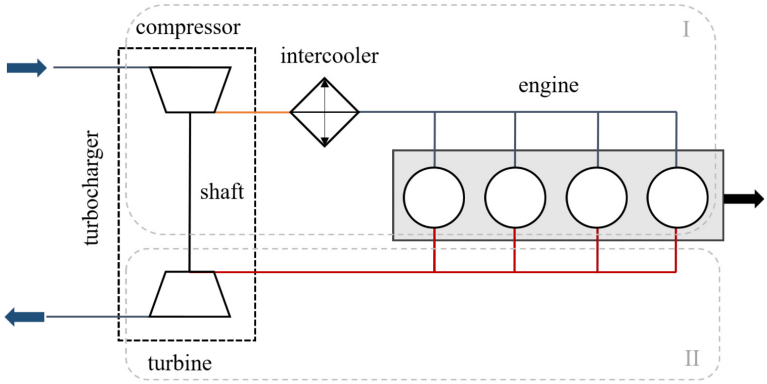


Figure 1.1.: functional principle of an exhaust-gas turbocharger

The increased oxygen in the combustion chamber allows for more fuel to be burned, thereby increasing engine power [5]. The amount of available oxygen is directly propor-

tional to the air density. Following ideal gas law:

$$\rho = \frac{p}{R \cdot T} \tag{1.1}$$

an increase in air density ρ is proportional to pressure p and inversely proportional to temperature T. Therefore, high-pressure, low-temperature air is advantageous for the engine.[5]

In addition to the oxygen increase, higher intake pressure also raises the effective volumetric compression ratio. Although the geometric compression ratio of the engine remains unchanged, beginning the compression stroke at a higher absolute pressure and density leads to a correspondingly higher density and temperature at the end of the stroke. This improves the thermodynamic conditions for the subsequent combustion process and contributes to higher overall efficiency.

The second benefit of turbocharging is the recovery of energy from the exhaust gases. In naturally aspirated engines, the expansion process is limited by piston motion. When the piston reaches bottom dead center, the exhaust gases are released while their pressure still exceeds ambient, leaving residual expansion work unused. In turbocharged engines, this remaining energy is utilized by expanding the exhaust gases through a turbine that drives the compressor [5]. Although the turbine increases the exhaust backpressure seen by the engine and therefore raises pumping losses, the amount of recovered energy is considerably higher, resulting in a net improvement in overall efficiency.

Beyond these thermodynamic advantages, turbocharging also enables engine downsizing. For a given power output, a smaller displacement engine can be used. Smaller engines exhibit lower mechanical friction and reduced mass, both of which further contribute to improved fuel consumption of the vehicle.

1.2. Thermodynamic Requirements of a Turbocharger Compressor

Compressor maps are essential tools for evaluating and comparing compressor performance. They provide detailed information about the compressor's pressure ratio and efficiency at specific speeds and mass flow rates under quasi-steady conditions. Figure 1.2 illustrates a typical commercial vehicle compressor map, overlaid with the typical requirements for a new compressor design.

The primary requirement for a compressor is its efficiency at the engine design point. Commercial vehicles predominantly operate within a narrow range of conditions. Even minor improvements in this area can significantly reduce fuel consumption, particularly when considering a fleet of vehicles, as demonstrated in [7]. Additionally, an increased pressure ratio at the design point positively impacts overall engine performance.

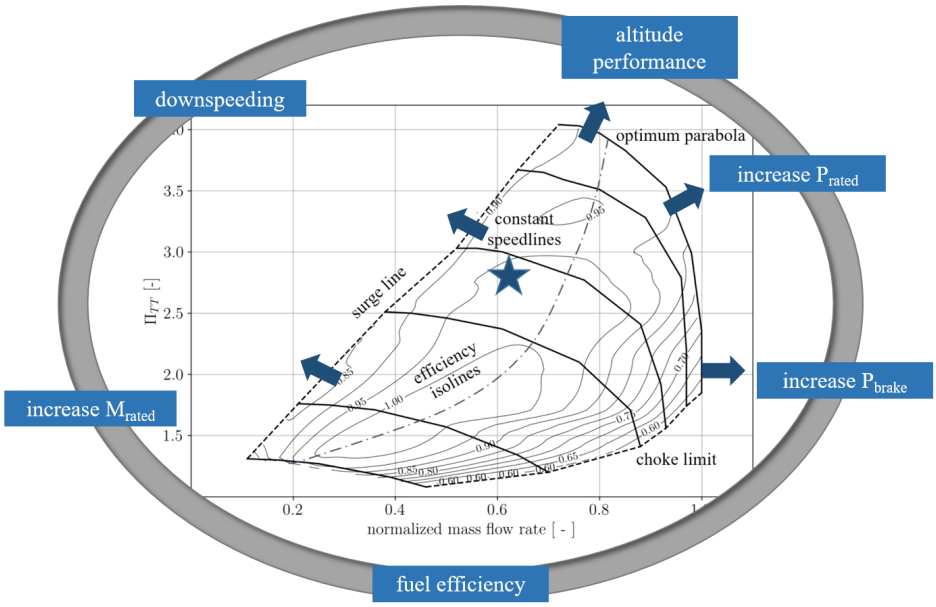


Figure 1.2.: requirements of a turbocharger compressor

The second requirement is a high choke mass flow for the engine brake. Unlike mechanical friction brakes, engine brakes utilize air compression, effectively turning the combustion engine into a large displacement-type compressor. This method allows vehicles to decelerate with reduced mechanical wear and heat generation, thereby lowering maintenance costs and enhancing safety during prolonged braking, such as when descending mountains. However, this necessitates a substantial air flow, challenging the compressor's choke capability.[8]

The third requirement is a sufficient surge margin to ensure safe engine operation. During a surge event, the flow field within the compressor collapses, causing partial or complete flow reversal. This results in violent pressure fluctuations that can severely damage the compressor, turbocharger, engine, and up- and downstream components. With the trend towards down-speeding engines and increased torque demands, the engine's operating line shifts left- and upward, necessitating more surge-stable compressors.

While improved altitude performance and increased rated engine power also contribute to a wider operating range, these factors are not directly linked to thermodynamic optimization but are constrained by the mechanical strength of the compressor wheel.

Figure 1.2 clearly illustrates the challenging and, to some extent, contradictory demands placed on turbocharger compressors: they must achieve high efficiency while providing a wide operating range. It is a well-established design principle that a compressor can either be highly efficient or have a broad operating range. Furthermore, turbocharger compressors have undergone extensive optimization over the past decades, achieving in-series efficiencies greater than 80% [9]. Consequently, the development of turbocharger compressors continues to be increasingly challenging.

1.3. Compressor Prediction Limitations

Given the contradictory nature of thermodynamic compressor requirements, careful consideration of optimization constraints and data quality is essential. However, this presents a significant challenge. While a compressor's operating point and choke point can be accurately predicted by CFD, its surge point remains unpredictable, as highlighted by I.J. Day:

"Good progress can be reported, but [...], after 75 years of research, we are still unable to predict the stalling behavior of a new compressor or to contribute much to the design of a more stall resistant machine." I. J. Day, 2015 [10]

To address the unpredictability of surge, conservative engineering guidelines have been developed, such as those proposed by Aungier [11]. Their conservativeness poses issues in areas like turbocharging, where safety margins are becoming increasingly intolerable. Additionally, the strong interaction of flow phenomena with other compressor components complicates general statements, leading to contradictory yet accepted engineering guidelines [12].

More recent advancements in CFD and computational power have made surge simulations a valuable tool for understanding stall and surge, as demonstrated by various studies [13, 14, 15, 16, 17]. However, due to the simultaneous occurrence of high levels of swirl, adverse pressure gradients, boundary layer separations, and time-dependent phenomena, simulations still face significant challenges. Consequently, surge simulations remain limited to a very few compressor designs, requiring tens of thousands of CPU hours and are prone to relatively high uncertainty.

1.4. Research Aim and Objectives

It has become evident that today's turbocharger compressor design processes, and consequently overall compressor performance, are constrained by the inability to predict and understand surge. Therefore, advancements in understanding surge will pave the way for more efficient engines, which will, in turn, provide significant benefits for both the environment and economy. Thus, the main objective of the current research is as follows:

Describe and model the main influences relevant to compressor surge at both component and system levels in heavy-duty commercial vehicle applications, so that new optimization potentials for surge and efficiency can be identified and utilized using currently applied design approaches.

In order to do so, four sub-objectives are defined.

Validation of the URANS Simulation Methodology: This objective aims to evaluate the capability of industrial simulation setups in accurately capturing the flow characteristics driving surge. This is achieved by comparing experimental data obtained from test rigs with simulation results, thereby validating the simulation methodology or identifying its limitations.

Investigation of the Surge Mechanism of a High-Performance Compressor and Outline of Potential Optimization: Utilizing the validated URANS simulation setup, this objective investigates the surge mechanism in a high-performance compressor. This investigation contributes to development in several ways. Firstly, it enables precise optimization recommendations for a specific design, thereby enhancing compressor performance. Secondly, it identifies critical design parameters, facilitating the evaluation of parameters currently used in surrogate-modeled design approaches. Lastly, it aids in determining the inclusion or exclusion of new parameters in future design iterations.

Investigation of Transient Environments and their Consideration in Early Stages of Compressor Development: Diesel engines create transient environments in which turbocharger compressors must operate, contrasting with the steady-state conditions of turbocharger test rigs where compressors are thermodynamically evaluated. This discrepancy can lead to significant deviations in efficiency, pressure ratio, and surge margin. Therefore, it is crucial to determine the origins of these phenomena and evaluate their consideration in early design phases.

Investigation of Surge Feedback for Surrogate-Model Based Design Approaches Without Geometric Constraints: Based on the findings of the third objective, this objective aims to develop a reduced-order model that enables fast and accurate surge prediction. These outcomes shall then be used to provide feedback to an optimizer, preventing it from optimizing efficiency at the expense of surge margin. If successful, this will lead the way for significant compressor performance improvements by replacing overly conservative surge constraints.

1.5. Structure of the Work

The work begins with an introduction to fundamental knowledge. This includes the basics of fluid mechanics, turbomachinery, stall and surge in centrifugal compressors, and principles of design optimization.

Next, the methodologies employed in this research are introduced. The chapter is divided into two sections: the first details the various test benches, emphasizing their accuracy and application, while the second introduces the simulation methodologies.

Following the establishment of these methods, the validation of the simulations is undertaken. This involves a mesh and time step independence study. Furthermore, CFD

results are compared against transient measurements from the electric test rig and time-averaged measurements from the hot gas test rig.

The validated simulation setup is then utilized to investigate the surge trigger of a compressor at a critical engine operating point. Detailed flow analyses are conducted, and the observed phenomena are compared with existing literature. Upon understanding the surge mechanism, optimization opportunities are identified, and their effectiveness discussed based on simulation or measurement results.

In the subsequent chapter, the focus shifts from the component level to the system in which the compressor operates. Experiments are conducted on both the hot gas test rig and the engine test rig. The results are compared with literature, and the response of the compressor and turbocharger to pulsating backpressure is examined.

Finally, the validated URANS, insights from the system investigation, and an extensive dataset of compressors are utilized to develop an automated workflow for compressor optimization that incorporates surge feedback. A detailed analysis of each subsystem -the compressor model, system model, and optimization model- is provided, and the optimization results are discussed using test bench data. The thesis concludes with a summary of all findings and outline of future work.

2. Fundamental Knowledge

This chapter introduces the fundamental knowledge required in this work. First, the fundamentals of fluid mechanics and its most important equations, the Navier-Stokes-Equations, are presented. Euler's Turbomachinery Equation is then derived before a more detailed look at commercial turbochargers and their most common defining thermodynamic parameters is presented. An introduction to stall and surge is given, along with commonly applied operating range enhancement methods. The chapter ends with a description of data-driven design optimization, in the context of which the work presented here was developed.

2.1. Fundamentals of Fluid Mechanics

In fluid mechanics, the Lagrangian and Eulerian approaches are the two fundamental methods for describing fluid motion. The Lagrangian approach follows individual fluid particles as they move through space and time, tracking their trajectories and changes in properties along their paths. Conversely, the Eulerian approach focuses on specific locations in the space through which the fluid flows, observing changes in fluid properties at fixed points over time. For many common engineering problems, the Eulerian approach is preferred and hence used in this work. [18, 19]

A fluid is characterized as any material that is continuous and does not show any resistance towards shear stresses [18]. In the context of this work, a fluid is also considered isotropic, meaning its properties are uniform in all directions [19].

Fluids can be divided into several groups, the most common being based on their shear stress response[1] and reaction to pressure forces. Although technical classification often uses the terms gases and liquids, it is not always clear from a thermodynamic point of view. [18]

Many technical relevant fluids such as oils, water, technical gases, and air, show a linear relation between shear stress τ and the velocity gradient du/dy, Eqn.2.1, and are called Newtonian fluids [19]. In the equation, μ represents the material constant *dynamic viscosity*.

$$\tau = \mu \frac{du}{dy} \tag{2.1}$$

When a fluid subjected to normal forces undergoes a change in volume, it is termed *compressible*, otherwise, it is considered *incompressible*. In reality, no fluid is truly incompressible, but the changes in density can be so negligible that assuming incompressibility becomes a valid simplification [19]. The Mach number *Ma*, defined as the ratio of the fluid

[1] In reality, shear stresses on the control volume are microscopic momentum transfers. For sufficiently large control volumes, this momentum transfer can be regarded as a shear force, although this violates the definition of a fluid. [18]

velocity u to the speed of sound in the fluid a, as shown in equation 2.2 is a commonly used criterion[18, 20]. When $u << a$, indicating a low Mach number (approximately 0.25), a fluid can be treated as incompressible [19].[2]

$$Ma = \frac{u}{a} \tag{2.2}$$

2.1.1. Conservation Equations

The mechanical fundamental equations are universally valid for fluids [18], allowing the formulation of continuity equations for mass, energy, and momentum [19].
For the formulation, the intensive state variables:

- pressure p
- density ρ
- temperature T
- internal energy e

are used. The velocity U is represented by its components in each direction: $j = 1, 2, 3$.

The first continuity equation is mass conservation. Equation 2.3 shows the general formulation for compressible fluids [18].

$$\frac{\partial \rho}{\partial t} + \frac{\partial (\rho U)}{\partial x} = 0 \tag{2.3}$$

The second continuity equation is momentum conservation 2.4, a result of Newtons second law. This equation is more commonly known as the Navier-Stokes Equation. [18]

$$\rho \left(\frac{\partial U_j}{\partial t} + U_i \frac{\partial U_j}{\partial x_i} \right) = -\frac{\partial p}{\partial x_j} - \frac{\partial \tau_{ij}}{\partial x_i} + \rho g_j \tag{2.4}$$

The left hand side addresses the change in momentum due to variations of the velocity in time and space. On the right-hand side, the changes due to pressure and viscous forces are considered. The last term ρg_j is the change in momentum due to gravity and acts as a source term. Other possibilities include the inclusion of centrifugal or Coriolis forces [12]. τ represents the stress tensor. For Newtonian fluids, the following equation 2.5 applies [18]:

$$\tau_{ij} = -\mu \left(\frac{\partial U_j}{\partial x_i} + \frac{\partial U_i}{\partial x_j} \right) + \frac{2}{3} \delta_{ij} \mu \frac{\partial U_k}{\partial x_k} \tag{2.5}$$

The first term relates to the viscous stress due to deformation of the fluid particle. The second term represents the dilatational stress, which occurs when the volume of the fluid particle changes. The Kronecker Delta δ_{ij} is a mathematical operator.

For incompressible, isothermal flows of Newtonian fluids, where $\rho = const$ and $\mu = const$, equations 2.3 and 2.4 simplify to a closed system with four unknown variables

[2] For hydraulic flow machinery, fixed pressure thresholds are utilized [19, 20]

(U_j, p) and four equations [18]. Hence, they can be solved without considering energy conservation [21].

For compressible flows, another equation is required to close the system of equations. This can be achieved by considering the conservation of energy, mathematically represented by equation 2.6 [18]:

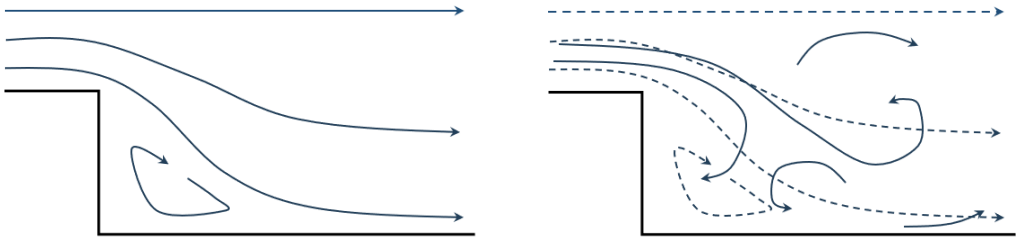
$$\left(\frac{\partial(\rho e)}{\partial t} + \frac{\partial(\rho U_i e)}{\partial x_i}\right) = \lambda \frac{\partial T}{\partial^2 x_i} - p\frac{\partial U_j}{\partial x_j} + \tau_{ij}\frac{\partial U_j}{\partial x_i} \tag{2.6}$$

Here, λ expresses the thermal conductivity of the fluid. The left-hand side of the equations represents the temporal and spatial change of the inner energy of a fluid particle. On the right-hand side, the terms represent (I) heat input, (II) volumetric work, and (III) irreversible transfer of mechanical work into heat. [18]

The resulting system of equations is highly complex and, in a wider context, also referred to as the Navier-Stokes-Equations. Numerical schemes are widely used to solve these equations [18], with Finite Volume Method (FVM) being the most common one [12, 21].

2.1.2. Laminar and Turbulent Flows

A flow field can be either well-ordered with distinctive streamlines visible, or highly disturbed and dominated by numerously, randomly occurring vortex structures [21, 18], as illustrated in Figure 2.1.



(a) laminar flow (b) turbulent flow

Figure 2.1.: laminar and turbulent flow field

Based on its macroscopic characteristics, the flow field is classified as either *laminar* or *turbulent* [21]. Flows that exhibit both laminar and turbulent behavior are termed *transitional* flows [18]. Turbulent flows have significantly higher diffusion rates than laminar flows, typically several orders of magnitude greater [18]. This is attributed to the many vortices of different scales and known as turbulent diffusion [21].

Whether a flow becomes laminar or turbulent is dependent on its ability to dampen occurring disturbances, as symbolically shown in equation 2.7, [18].

$$U = U_0 \cdot e^{(\alpha-\beta)t} \tag{2.7}$$

Here, α represents a flow disturbance and β the viscous damping. Generally, any gradient in the flow field or fluid property constitutes a flow disturbance [18]. It is evident that a flow disturbance diminishes over time if $\alpha < \beta$, and grows exponentially if $\alpha > \beta$. Consequently, the flow stays laminar or becomes turbulent.

An important dimensionless parameter to characterize this behavior is the Reynolds Number Re, as shown in equation 2.8, where l represents a characteristic length.

$$Re = \frac{\rho U l}{\mu} \tag{2.8}$$

The Reynolds number can be interpreted as the ratio of inertial forces to viscous forces [18]. For low Reynolds numbers, viscous forces dominate, resulting in laminar flow, whereas high Reynolds numbers indicate a dominance of inertial forces, signifying turbulent flow. Commonly used critical values are $Re = 520-950$ for boundary layers [18, 22] and $Re = 2300$ for pipe flows [23]. Many flows are predominantly turbulent [21, 23].

2.1.3. Boundary Layers

A sharp velocity gradient occurs in the vicinity of walls due to friction. The fluid at the wall has zero velocity, a condition known as the no-slip condition, and its velocity increases steadily normal to the wall until the freestream velocity is reached. This region is called boundary layer, and for high Reynolds numbers such as encountered in compressors, it is usually thin relative to the length of the wall. [12, 23, 22]

Initially, a boundary layer is laminar. However, as the flow progresses downstream, it may transition to turbulent. This transition is closely related to performance and stability of airfoils [12] and is subject to intense research [18]. Figure 2.2 illustrates the three transition mechanisms.

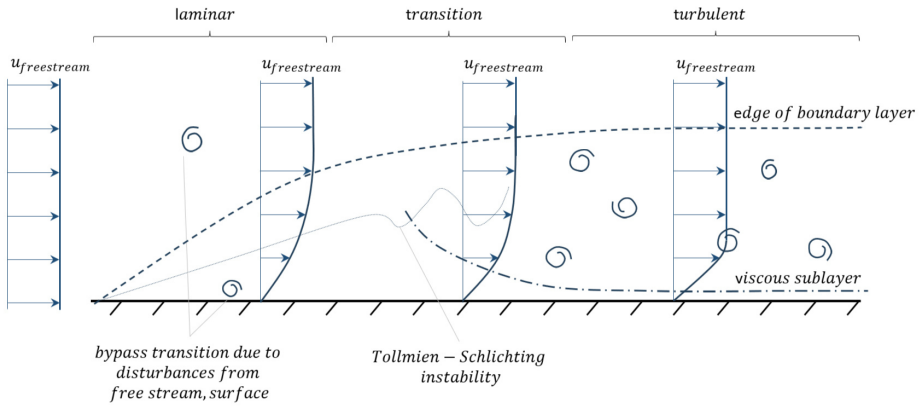


Figure 2.2.: boundary layer transition[3]

Early theories were based on inviscid stability theory and suggested that transition

[3]Reproduced with permission from Cambridge University Press, from [12], permission conveyed through PLSclear

occurs only if there was an inflection point in the velocity profile. Later, it was discovered that viscous instability waves, known as Tollmien-Schlichting waves, can destabilize the laminar boundary layer. A third trigger for transition is disturbances in the free stream or surface roughness, which can cause a rapid transition bypassing the Tollmien-Schlichting instability, known as bypass transition. Despite extensive research, boundary layer transition is not yet fully understood. [12]

Closely related to the type of boundary layer is the risk of flow separation. Near a wall, the fluid is slowed down by friction. If this coincides with an adverse pressure gradient, the momentum of the fluid might not be sufficient to overcome the pressure rise. Consequently, the flow stops or even reverses. [22, 12]

It is evident that high velocity counteracts such effects, making turbulent boundary layers less prone to detachment. However, this comes at the cost of a substantial increase in friction losses within the layer. [12]

2.2. Fundamentals of Turbomachinery

A turbomachine is defined as a rotating machine that continuously transfers energy to or from a fluid via its blades in an open system [12]. Turbomachines that transfer energy from the rotating shaft to the working fluid are called compressors (or pumps in case of incompressible fluids). Conversely, when energy is transferred from the fluid to the shaft, the machine is called a turbine. [20]

Turbomachinery is further classified based on the main flow direction. For compressors, this can be axial, radial, or mixed flow [7]. The Cordier diagram provides information about the most efficient turbomachinery type depending on operational conditions, rotational speed and rotor diameter [20]. For turbocharger applications, radial compressors are utilized [5].

2.2.1. Fundamentals of Radial Compressors

For the following considerations, the three velocities:

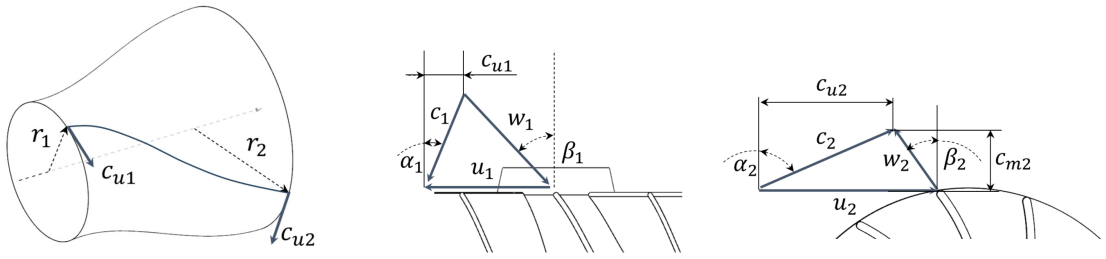
- absolute velocity c
- circumferential velocity u
- relative velocity w

are introduced [12].

These velocities are related via the fundamental kinematic equation 2.9 [7] and are illustrated in Figure 2.3.

$$\vec{c} = \vec{u} + \vec{w} \tag{2.9}$$

The vectors of velocity c and angle α pertain to the stationary reference system (absolute coordinate system), whereas the vectors of velocity w and angles β pertain to the moving reference system (relative coordinate system). [24]



(a) Euler turbomachine

(b) velocity triangles at compressor in- and outlet

Figure 2.3.: fundamental velocity considerations

The most general equation for turbomachinery was derived by Leonhard Euler [12]. Assuming a stationary, incompressible, frictionless, blade-congruent flow field in a rotor [20], torsional moment of the machine is described via:

$$M = \sum rF_u = \dot{m}(r_2 c_{u2} - r_1 c_{u1}) \tag{2.10}$$

Introducing the basic relation for specific work, $Y = \omega M/\dot{m}$, equation 2.10 becomes:

$$Y_{12} = (u_2 c_{u2} - u_1 c_{u1}) \tag{2.11}$$

Applying basic geometric considerations (see [12] for a detailed derivation), equation 2.11 can be transformed into:

$$Y_{12} = \frac{1}{2}[(u_2^2 - u_1^2) + (c_2^2 - c_1^2) + (w_1^2 - w_2^2)] \tag{2.12}$$

From this equation, the energy transformation in the rotor becomes evident. The first term describes the rise in kinetic energy through centrifugal effects, the second one the increase in kinetic energy of the absolute flow trough the rotor, and the third term the decrease in kinetic energy of the relative flow through the rotor. [20]

For a compressor, the work input into the rotor control volume is positive, meaning all three terms should be positive [12].

Considering the velocity triangles, it is apparent that the centrifugal effects $(u_2^2 - u_1^2)$ play the most significant role [12]. As centrifugal effects are independent of the mass flow rate, radial compressors achieve high pressure ratios at low mass flow rates compared to axial compressors, making them well suited for turbocharger applications [5].

Since the absolute velocity $(c_2^2 - c_1^2)$ increases across the rotor, the flow is decelerated in

a downstream diffuser to achieve the desired pressure rise [5]. However, this implies that the flow encounters an adverse pressure gradient, which might lead to separation in the diffuser and with this, substantial losses. Thus, well-designed and matched diffusers are required. [12]

The deceleration of the relative fluid velocity ($w_1^2 - w_2^2$) in the rotor is analogous to the increase in the flow passage area [5]. However, achieving this is not trivial due to the risk of flow separation in the rotor [20].

Based on these considerations, a radial compressor consists of the following elements:

- a rotor or impeller, that accelerates the fluid and, due to the radius increase, uses centrifugal effects to rise pressure
- a stator or diffuser, that decelerates the fluid leaving the impeller in such a way that minimal losses and separation occur
- a collecting container that guides the fluid leaving the diffuser into the downstream application.

The impeller is unshrouded due to the high circumferential velocities and consists of main and splitter blades. The splitter blades are downstream-shifted blades that enhance flow guidance in the region of high relative fluid velocity deceleration to avoid separation. The downstream shift leads to a larger minimal cross-sectional area of the impeller, allowing higher mass flows to pass through. [7, 12]

The diffuser can be either vaned or vaneless [6]. Although vaneless diffusers are generally considered more suitable for turbocharger application due to their superior map width and ease of manufacturing [12], vaned diffusers can lead to superior compressor characteristics in engine- relevant areas and are sometimes used in series application [9]. Often, so-called pinches, a short area between impeller and diffuser with constant through-flow area, are utilized to improve a diffuser's aerodynamic stability [25, 6].

The collecting container or volute can exhibit different cross sections such as symmetric and asymmetric ellipses, squares or rectangles, or circles [26]. For turbochargers, overhang volutes with asymmetric ellipse-like shapes are commonly used due to their low losses and compact design [7].

2.2.2. Thermodynamic Parameters

To allow a comparison between different compressors and operating conditions, characteristic thermodynamic parameters are used. The most common parameters include the referenced mass flow rate $\dot{m}_{ref}$, total-to-total pressure ratio Π_{TT}, isentropic adiabatic efficiency η_{is}, and the circumferential velocity u_2 of the turbomachine. [6, 7]

Since the actual mass flow rate varies depending on the inlet conditions, it is referenced to a specific condition. The reference condition is not standardized and can vary depending on the compressor manufacturer. In this work, a reference total pressure $p_{T,ref}$ of 1bar and a reference total temperature $T_{t,ref}$ of 298.15°K are used, following [7]. The referenced mass flow rate can be calculated using equation 2.13.

$$\dot{m}_{ref} = \dot{m}\frac{\sqrt{T_T}}{p_T}\frac{p_{T,ref}}{\sqrt{T_{T,ref}}} \tag{2.13}$$

The pressure rise of the compressor is given by the non-dimensional pressure ratio. Since both static and dynamic part of the pressure can be used in a turbocharger application, the total pressure at compressor outlet is considered [7]. The pressure ratio can be calculated as follows.

$$\Pi_{TT} = \frac{p_{2T}}{p_{1T}} \tag{2.14}$$

The aerodynamic quality of a compressor is expressed through its efficiency. It has become an accepted simplification to assume an isentropic, adiabatic process, although it is well-known that heat transfer occurs during testing and normal operation [27, 28]. The isentropic efficiency η_{is} can be calculated using equation 2.15.

$$\eta_{is} = \frac{T_{1T}}{T_{2T} - T_{1T}}\left[\left(\frac{p_{2T}}{p_{1T}}\right)^{\frac{\gamma-1}{\gamma}} - 1\right] \tag{2.15}$$

Another key parameter of the compressor is its rotational speed. For matching the compressor with the turbine, the rotational speed n is important since the turbine wheel and compressor impeller are mechanically connected via the shaft. Hence, the compressor rotational speed will be the same as the turbine. For comparison of different compressor impellers, the circumferential velocity at the impeller outlet diameter d_2 is used because of similarity law. The circumferential velocity can be calculated using equation 2.16.

$$u_2 = \pi n d_2 \tag{2.16}$$

To visualize compressor performance characteristics, compressor maps, such as the one depicted in Figure 2.4, are employed.

These maps illustrate the relationship between pressure ratio and mass flow rate at constant rotational speeds. The surge or stall line on the left marks the boundary of stable operation, beyond which the compressor becomes aerodynamically unstable. The choke line on the right represents the maximum flow rate the compressor can deliver, as the flow velocity reaches sonic conditions in the critical region.[4]

The constant speedlines are overlaid with the efficiency contours. The efficiency parabola follows the maximum value and indicates the best operating area of the compressor. A well-matched turbocharger compressor does not only allow stable and sufficient

[4]The choke line in the compressor map does not represent the true aerodynamic choke but rather a value slightly above, established by the manufacturer to avoid critical operating conditions [29]. For turbocharger compressors, efficiency thresholds are employed. Volume flow percentages, reductions in pressure ratio, or calculated Mach numbers are also utilized [30].

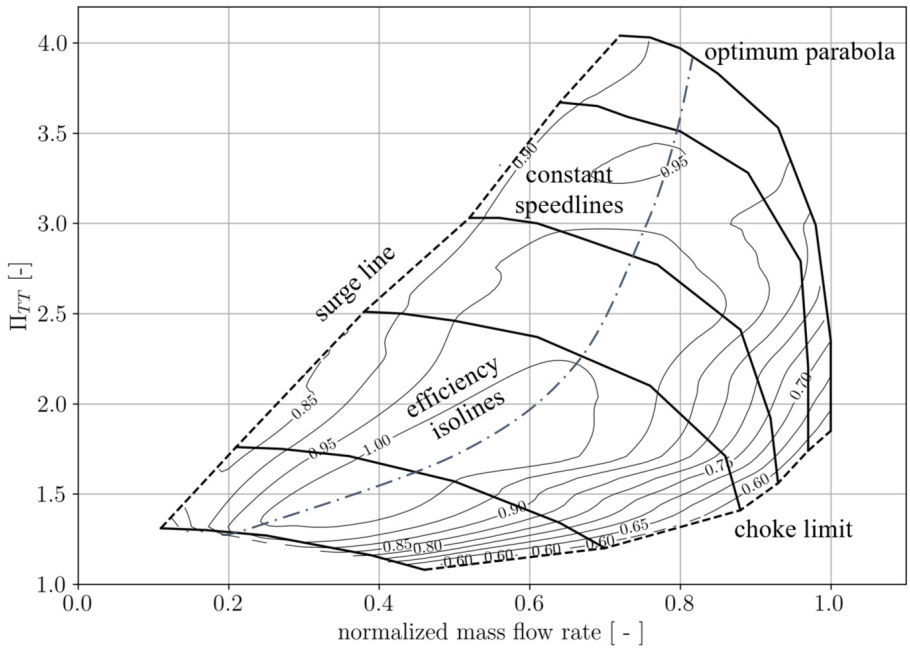


Figure 2.4.: compressor map

operation across all engine operating points, but has the efficiency parabola aligned with the engine's primary operation area for maximum fuel efficiency.

2.2.3. Fundamentals of Commercial Vehicle Exhaust Gas Turbochargers

A cross-section of a typical heavy-duty commercial vehicle turbocharger can be seen in Figure 2.5.

The core of the turbocharger is the bearing housing, which consists of a cast steel housing, a ball bearing, and the turbocharger shaft that mechanically connects the turbine and compressor wheels. Within the housing, oil-permeated cavities are placed to reduce heat transfer from the hot turbine side to the cold compressor side. The oil is also essential for lubricating the ball bearing system. The oil inlet and outlet are centrally located within the housing. An inductive speed sensor is situated in the bearing housing to measure the circumferential speed of the shaft.

The turbine housing directs the exhaust gases to the turbine wheel, where they expand, driving the shaft. Due to the gases high temperature, a steel alloy is used for the turbine housing and a nickel alloy for the turbine wheel. The volute is divided into two channels with different cross-sectional areas. The smaller cross-section creates higher backpressure, allowing part of the mass flow to be utilized for exhaust gas recirculation (EGR), whereas the larger cross-section creates minimal backpressure and is used solely for powering the turbine [8].

The compressor housing, cast from an aluminum alloy, directs the inflow to the impeller, decelerates the flow in the diffuser, and collects the gas in the volute. A ported

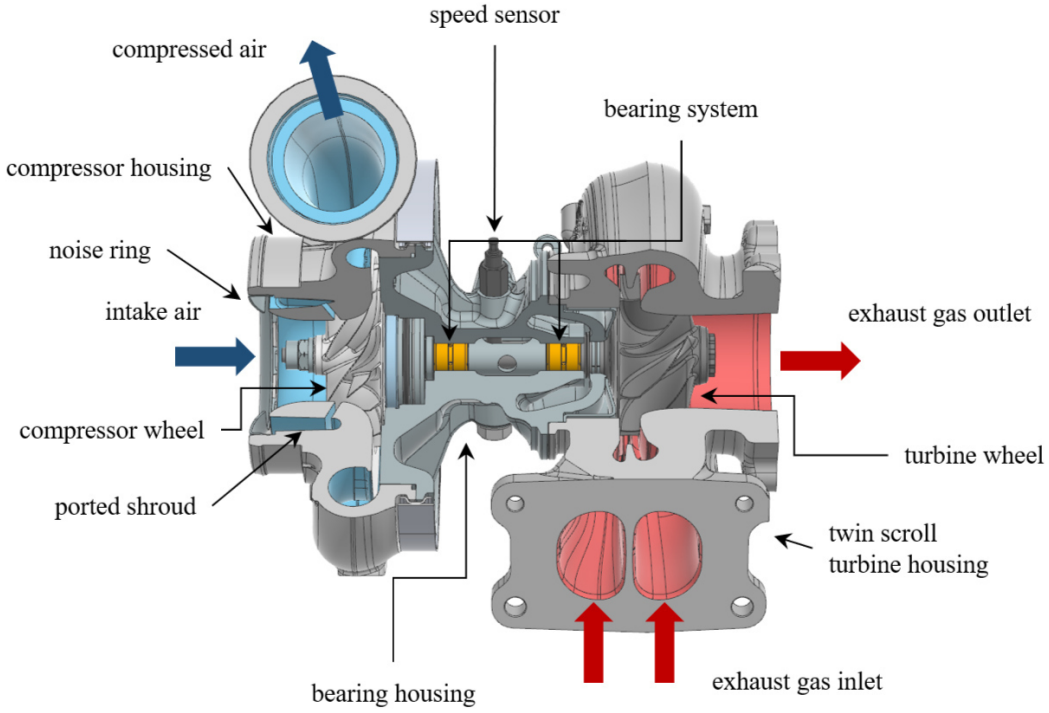
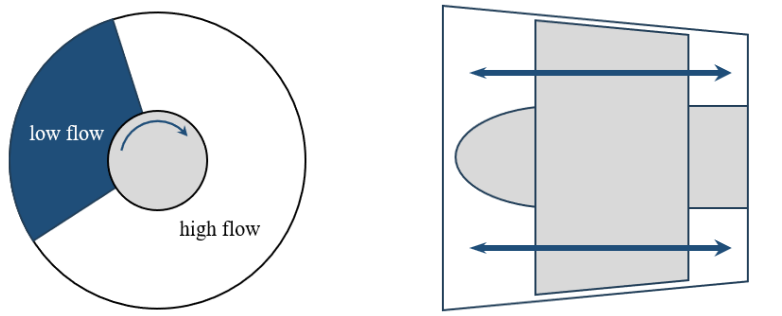


Figure 2.5.: cross-section of a commercial vehicle exhaust gas turbocharger

shroud extends the operating range of the compressor, while a noise ring is employed to reduce blade-induced noise.

2.3. Fundamentals of Stall and Surge in Centrifugal Compressors

Stall and surge are adverse and, in many cases, violent flow phenomena in axial and radial compressors happening at low mass flow rates and high pressure ratios. Research can be traced back to the 1920s when rotating stall in a centrifugal water pump was reported for the first time. Since then, stall and surge have been the focus of intense research. [10, 31]



(a) compressor stall - circumferentially nonuniform flow

(b) compressor surge - axially oscillating flow

Figure 2.6.: stall and surge in compressors[5]

[5]Used with permission from ASME, from [32], permission conveyed through Copyright Clearance Center, Inc.

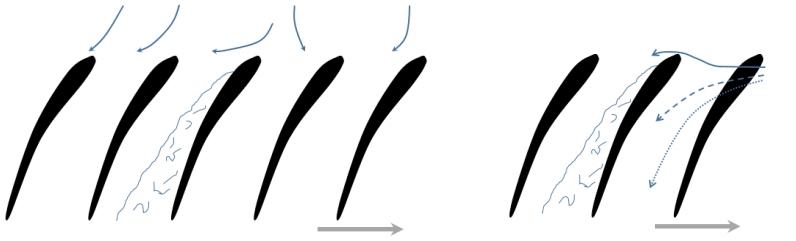
Rotating stall is a flow instability that propagates circumferentially and does not impact the annulus-averaged mass flow of a compressor [10, 32, 33], as depicted in Fig. 2.6a. Impeller stall typically rotates at 20-80% of the compressor's rotational speed, whereas vaneless diffuser stall propagates at 5-22% [34].

Surge, on the other hand, is an axial flow instability characterized by substantial pressure and mass flow oscillations [10, 33], as illustrated in Fig. 2.6b. The frequency of surge is several orders of magnitude lower than that of stall [32, 35, 36].

2.3.1. Compressor Stall

Much of the early and fundamental work on compressor stall has been conducted on axial compressors. One of the primary reasons is the distinct behaviour of these compressors, as high-loading axial compressors experience a significant pressure drop when stalled [10]. This poses a substantial risk to aero engines, driving significant commercial and public research demand [10, 31, 37]. Nevertheless, many findings from this research can be applied to centrifugal compressors [38, p. 14].

Stall is a flow instability that induces a circumferentially, nonuniform flow in the compressor, while the averaged mass flow through the compressor remains constant [32]. The studies by Emmons et al. [39], and Hoying et al. [40], performed on axial compressors, are utilized to explain some of its basic principles, as outlined by Yoon et al. [41], compare Fig. 2.7.



(a) stall propagation, based on Emmons et al. [39]

(b) stall inception, based on Hoying et al. [40]

Figure 2.7.: basic stall principles[6]

The work by Emmons et al. [39] discusses the effect of stall propagation in blade rows. The explanation is as follows: As the mass flow rate decreases at constant rotor speed, the incidence angle increases, leading to a mismatch between the blade contour and the flow field. The now limit-stable flow field experiences a transient disturbance, causing a single blade to stall as its boundary layer detaches. With the passage stalled, its throughflow area decreases, reducing its volume flow. Consequently, flow is diverted towards the following passage, further increasing the incidence angle and leading to a stall. The newly stalled blade improves the first blade's incidence angle while deteriorating the next one's incidence angle. Thus, the stall cell begins to rotate against the circumferential speed

[6] Used with permission from ASME, from [41], permission conveyed through Copyright Clearance Center, Inc.

direction of the compressor [39].

The work by Hoying et al. [40] considers a compressor's much more complex flow field. Manufacturing and material deformation effects, driven by centrifugal forces and temperature, necessitate a gap between the impeller blade and compressor housing[7]. Driven by the pressure difference between the blade's pressure side and suction side, a tip clearance flow develops, leading to a tip clearance vortex. This vortex strengthens as flow is reduced, and its trajectory shifts toward the leading edge of the subsequent blade. Once perpendicular to the axial direction, a small perturbation can cause leading-edge spillage, resulting in stall.

Centrifugal compressors exhibit more complex rotor geometries and include additional components such as volutes and different types of radial diffusers. Every component can experience stall, and stall definitions range from flow separation to significant static pressure distortions [22]. Moreover, all these components interact, making it challenging to pinpoint the true origin of stall. Notable examples are the studies by Yang et al. [42, 43]. Although the compressors stall at the impeller inlet, the stall inception points are related to the volute tongue, which generates a non-uniform static pressure distortion that affects the impeller and diffuser.

The most apparent component responsible for non-uniform flow is indeed the volute. Volutes are typically designed to conserve angular momentum, leading to linear A/R ratios [44]. As the diffuser outlet flow angle varies with increasing or decreasing mass flow, the volute will act as a nozzle or diffuser under off-design conditions [12]. This, in turn, affects the static pressure, leading to a non-circumferential flow distortion. The volute tongue introduces another significant static pressure distortion due to the abrupt geometry change, as shown, amongst others, in [14]. Using 3D CFD, Zheng et al. [45] demonstrated that these distortions can trigger impeller stall when allowed to propagate upstream.

Although many geometrical pathways to stall exist, for axial compressors, they can be categorized into two types of stall inception: modal stall and spike stall. This classification is based on the temporal development of the disturbance. Modal stall describes a long, slowly growing disturbance, whereas spike stall appears suddenly and develops into a full stall cell within less than 10 revolutions. [10, 16]

Modal stall has a comparably low stall cell speed of less than 50% of the rotor speed and occurs at the high point of the total-static compressor map. It is therefore predictable in linear stability analysis. [16, 10]

Spike stall, on the other hand, has a higher stall cell speed of greater 50% and can occur even on the negative slope of the corresponding compressor curve [10]. It has been

[7] Shrouded blades are excluded from review.

found that for axial compressors, spikes are associated with the formation of a vortex tube, driven by leading edge separation [16].

2.3.2. Compressor Surge

Surge is a global instability that necessitates consideration of the entire compression system [46, 47, 22]. It describes the axial breakdown of the flow field in the compressor, leading to either partial (mild or classic surge) or complete (deep surge) flow reversal [48]. Recognized as the most severe form of compressor aerodynamic instability, surge has the potential to inflict significant damage or even cause failure within minutes [31, 49]. It has been proven that axial compressors must experience stall prior to the onset of surge [10].

For centrifugal compressors, it remains ambiguous whether modal and spike stall are the sole triggers. Spakovszky and Roduner experimentally validated both mechanisms in a centrifugal compressor's vaned diffuser (as cited in [50]). Conversely, Godard et al.'s experimental investigation [50] failed to identify any stall precursors before surging in a centrifugal compressor with a vaned diffuser designed for fuel cell applications, thereby challenging these mechanisms to be the only two possible. This perspective is further supported by Casey and Robinson [12].

Figure 2.8 illustrates mild and deep surge in both a quasi-steady compressor map and time resolved static pressure ratio measured on the test bench. The compressor is representative of heavy-duty commercial vehicle turbocharger applications and features a vaneless diffuser and a ported shroud. The surge event is induced by gradually closing the test bench's throttle valve, thereby reducing the mass flow rate. Once deep surge occurs, the throttle valve is reopened to prevent damage to the compressor and test bench.

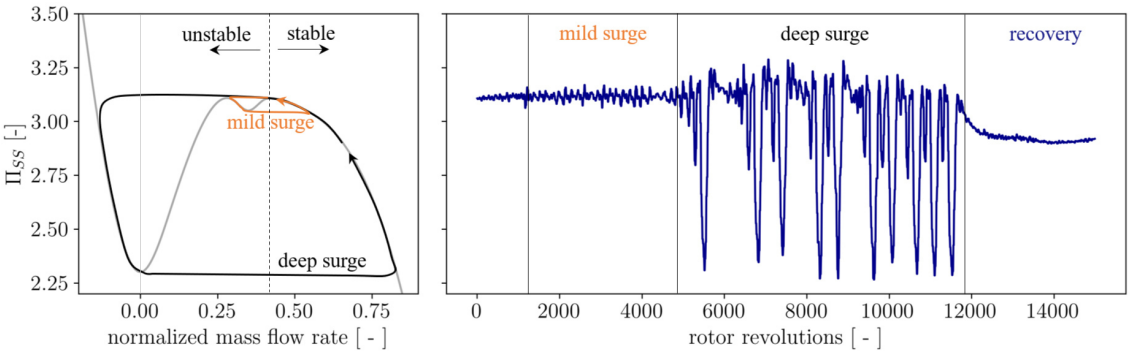


Figure 2.8.: surge event

Initially, the compressor enters a mild surge regime (1200 revolution mark / orange loop), characterized by harmonic pressure oscillations. Although the amplitude of these pressure oscillations is relatively small, the instantaneous mass flow rate varies significantly, as seen in the compressor map. A loop forms, encapsulating the smaller low point

of the compressor characteristic. This low point typically forms when recirculation in the diffuser occurs, but the compressor flow field does not completely break down [51]. If this quintic-shaped compressor characteristic is pronounced and the throttle valve step sufficiently small, as in this case, mild surge can be observed for several thousand rotor revolutions.

Eventually, the mass flow rate decreases to the second positive gradient section of the steady compressor characteristic. The instantaneous operating point enters a large loop in the compressor characteristic, reaching negative mass flow rates (discharge of the downstream plenum through the compressor) and large pressure fluctuations. This marks the beginning of deep surge, which is the most violent type of surge, acoustically detectable by a low-order buffeting noise and visually by vibration of the upstream and downstream piping. Deep surge is stopped by reopening the throttle valve, allowing mass flow to increase and re-establishing a homogeneous, stable flow.

The lumped parameter model of Greitzer, introduced in [32] and validated with experiments in [52], has significantly influenced surge modeling and the understanding of surge as a system phenomena. Initially derived for axial compressors, it was later found applicable to centrifugal compressors as well. In 1992, Fink [33] specifically adapted the model for centrifugal compressors by introducing a variable compressor rotational speed during surge, resulting in a better fit between predictions and experiments.

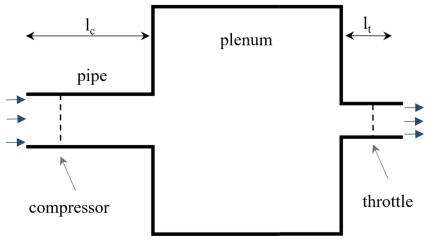


Figure 2.9.: Greitzer compression system[8]

The Greitzer model simplifies the compression system into five components: inlet ducting, compressor, plenum, outlet ducting, and throttle valve, representing a Helmholtz resonator, as shown in Figure 2.9. To maintain simplicity in the ordinary differential equations (*ODE*), incompressibility in the pipes and constant pressure in the plenum are assumed. The compressor is represented as an actuator disk. This results in four ODEs that must be solved numerically.

The ODE for flow in the compressor duct:

$$\frac{d\Phi_c}{d\tau} = B(\Psi_c - \Psi_p) \tag{2.17}$$

[8]Used with permission from ASME, from [32], permission conveyed through Copyright Clearance Center, Inc.

For the flow in the throttle duct:

$$\frac{d\Phi_t}{d\tau} = \frac{B}{G}(\Psi_p - \Psi_t) \tag{2.18}$$

For mass conservation in the plenum:

$$\frac{d\Psi_p}{d\tau} = \frac{1}{B}(\Phi_c - \Phi_p) \tag{2.19}$$

For the transient response of the compressor:

$$\frac{d\Psi_c}{d\tau} = \frac{1}{B}(\Psi_{c,ss} - \Phi_c) \tag{2.20}$$

where Ψ represents non-dimensional mass flow and Φ non-dimensional pressure rise. The parameters B and G are defined as follows:

$$B = \frac{u}{2a}\sqrt{\frac{V_p}{A_c l_c}} \tag{2.21}$$

$$G = \frac{l_t A_c}{l_c A_t} \tag{2.22}$$

where u is tip speed velocity and l_c, l_t, A_t, A_c are the corresponding lengths and areas of the compressor and throttle duct.

One of the most important findings is the introduction of the *B-stability-parameter*, equation 2.21, which can be expressed as a ratio between the pressure and inertia forces of the compression system [53, 10]. If the compression system's B-value exceeds the compressor's critical B-value, surge occurs; for lower values, the compressor moves to a new operating point and encounters rotating stall. For the original setup, the critical B-value was found to be 0.7. However, it is emphasized that the B-Parameter is not universal but unique for every compressor and has to be found experimentally.

The parameter G, a dimensionless geometry ratio, was found to be of minor importance and hence was not further investigated. [32]

The model can capture the onset, amplitude and frequency of stall and mild surge [9] [32]. However, deep surge is not well-captured as it is driven by the resistive elements, such as how quickly the flow can discharge through the compressor [50, 32].

Although the Greitzer model has greatly contributed to today's understanding of surge, it has limitations for turbocharger applications, where several resistances and volumes are located upstream and downstream of the compressor. [54, 46, 55, 56]

[9] This holds true only if the quasi-steady compressor characteristic (model input) matches the compressor behavior in the unsteady regime. As discussed in [51], cubic-like shapes, often used for centrifugal compressors, can only have stable, or limit cycle (deep surge), states. This is often overlooked when applying the Greitzer model to centrifugal compressors.

2.3.3. Surge in Transient Environments

Transient systems are common in pipeline and turbocharging applications, where displacement machines (primarily piston compressors or reciprocating engines) are combined with turbomachinery. Displacement machines generate strong pressure and volume flow pulses, which impact both compressor efficiency and operating range. This has been documented in various studies, including an automotive heavy duty turbocharger application [1], an automotive passenger car turbocharger application [57], a pipeline compressor application [58], and an unmanned aerial vehicle turbocharger application [59].

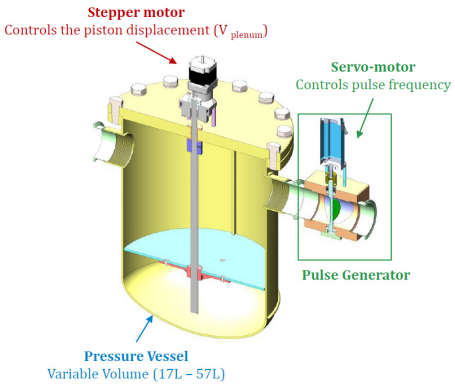


Figure 2.10.: Pulsating Flow Device (PFD) [1]

Experimental work conducted by Barrera-Medrano [1] involved adapting a compressor test rig with a variable plenum to simulate different volumes behind the compressor and incorporating a rotary valve to generate pressure pulses typical of heavy-duty diesel engine applications (see Figure 2.10). The experiments demonstrated that the operating range of the compressor is positively influenced when subjected to pulsating backpressure. Similar findings were reported by Galindo et al. [57]. Another important outcome is that pulse frequency influences hysteresis behavior. For operating points on a positive compressor slope, pressure fluctuations dominate the hysteresis curve, whereas for operating points on the negative slope of a speedline, mass flow oscillations dominate the hysteresis loop.

Shu et al. [60, 61] build upon these results and extend research on pulse frequency and amplitude using 1D simulation, as experimental approaches cannot decouple pulse frequency, amplitude and operating point. The results show that surge is postponed when the compressor operates under pulsating backpressure conditions due to the interaction between forced oscillation by the pressure boundary condition and the self-sustained surge oscillation. However, it is noted by the authors that the stability of a compressor in a pulsating environment depends on various factors and is not limited solely to amplitude and frequency.

Yang et al. [62] conducted a 3D CFD analysis to understand flow physics under

pulsating backpressure. A URANS simulation was performed and validated with thermodynamic measurements. The simulation results show that the pulsating backpressure suppresses vortices in the impeller, which arise due to the Kelvin-Helmholtz instability. This suppression reduces impeller blockage, thereby enhancing surge stability.

Although significant progress has been made in understanding surge in transient environments, accurately predicting surge onset in engine applications remains challenging. Surge margin can either improve or deteriorate on an engine [24] or engine-like test bench [54], and experimentally detecting the primary surge driver is nearly impossible due to the confined space and numerous variables involved.

Therefore, reliable surge data can currently only be obtained through testing. Engine surge tests are not standardized, and various techniques are employed in literature. One method involves feeding compressed air into the compressor outlet [24], thereby reducing the compressor mass flow rate while maintaining overall engine mass flow. Other methods include increasing EGR or conducting dynamic load testing in vehicles [6].

2.3.4. Operating Range Enhancement

In order to increase the operating range of a compressor, various methods can be employed, typically categorized into active and passive surge control. Active surge control methods involve the use of actively controlled devices, such as adjustable inlet guide vanes [63], adjustable diffuser vanes [6], bypasses [64], aerodynamic pre-swirl [65], or loudspeakers [66]. Although these methods can significantly improve the operating range, their complexity precludes their use in automotive series applications. However, bypass valves are commonly used in gasoline and hydrogen combustion engines.

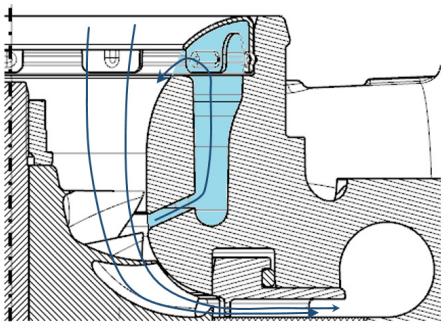


Figure 2.11.: ported shroud

In Diesel engine applications, passive surge control is employed [67]. The most prevalent device is the ported shroud or recirculation slot, see Figure 2.11. Other passive surge control methods are casing treatments, which involve slots, holes or grooves in the shroud contour. Yoon et al. [41] provide an overview of their function, advantages and disadvantages. Due to higher manufacturing costs compared to ported shrouds, casing treatments are not used in series applications and are therefore excluded from review. Unfortunately,

the term "casing treatment" has become somewhat synonymous with "ported shroud", leading to unnecessary confusion.

Qiu et al [68] utilize steady RANS simulation to derive a meanline model of the ported shroud. It is found that two different effects are responsible for the improved stability. Firstly, the recirculating flow at low mass flow rates blocks part of the inducer, thereby improving the inlet incidence angle. Secondly, the removal of low-momentum flow accumulating in the clearance gap enhances the downstream flow, resulting in lower end-wall losses. This, in turn, leads to improved pressure rise capability of the impeller, and a generally cleaner flow field. Consequently, the stall margin is improved.

Large Eddy Simulation (LES) is employed in [69] to capture the detailed flow field of the impeller interacting with a ported shroud. The findings show that the improved pressure rise is attributable to higher blade loading near the impeller leading edge. In the absence of the ported shroud, backflow at the impeller tip adversely affects the incidence angle, thus reducing blade loading and propagating flow disturbances through the compressor.

Studies utilizing particle image velocimetry (PIV) demonstrate that significant flow recirculation occurs near surge conditions, validating simulation-based work. Furthermore, both sets of measurements reveal that the recirculation flow is non-uniform and influenced by the ported shroud's supportive structure. [70, 67]

A numerical optimization of the supportive structure is conducted in [71] and validated by experiments. The optimized support structure fosters a more favorable flow field and induces pre-swirl, leading to significant improvements in surge margin and noise reduction, with a slight increase in choke mass flow.

Additional work is conducted in [72, 73], where the mitigation of the non-axisymmetric pressure distortion induced by the volute using the ported shroud is investigated. By precisely matching the bleed slot height with the distortion, a 10% improvement in surge margin over standard ported shroud designs is achieved.

Despite these findings, significantly aero-optimized ported shroud designs are not widely adopted in series applications, primarily due to their impact on compressor lifespan. The positioning and thickness of the supportive structure are constrained by blade excitation, thermal stresses during load cycles, and containment requirements in the event of impeller failure. Consequently, aerodynamic optimization in this area is severely limited.

2.4. Fundamentals of Design Optimization

Optimizing a compressor, or more generally, any type of machine, typically follows one of two major design methodologies: knowledge-based optimization or data-driven optimization. In a knowledge-based optimization, a machine is optimized based on explicit information, such as in-depth analysis of test or simulation data. For complex relationships, data-driven optimization is typically employed, as explicit information is difficult or even impossible to obtain. In this approach, large data sets are utilized to enable surrogate modelling, and mathematical optimizers are applied to find the optimal solution. In commercial turbocharger compressor development, data-driven optimization has become a well-established design methodology [74, 75, 76].

According to Pietrenko-Dabrowska and Koziel [77], four steps are required to obtain a sound surrogate model, which forms the basis of successful data-driven optimization:

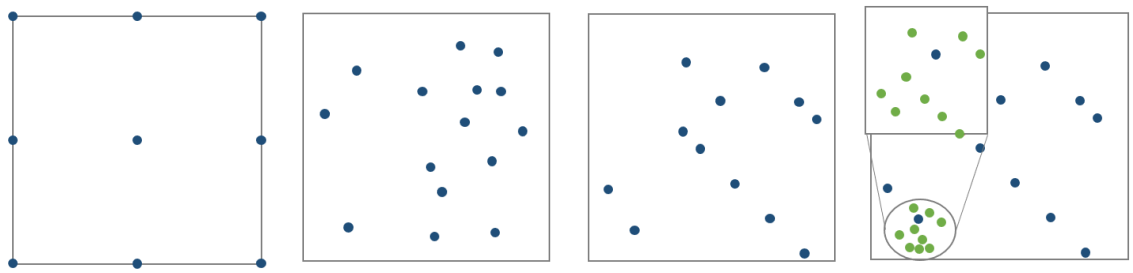
1. Design of Experiments (DoE): This step involves defining the design space and ensuring its comprehensive coverage, resulting in an initial set of experimental designs.
2. Training Data Acquisition: Following the generation of designs, their system outputs (responses) must be evaluated. This step is typically the most resource-intensive.
3. Model identification: In this phase, the most appropriate model algorithm is selected, and the surrogate model is constructed.
4. Model validation: The predictive accuracy of the surrogate model is assessed. If the results are unsatisfactory, additional design points may be incorporated to enhance the model.

In commercially available software, model identification and model validation are often integrated into a single automated process, commonly referred to as *metamodelling*. This integration is due to the necessity of in-depth knowledge of the underlying, sometimes even proprietary, surrogate model algorithm for proper validation, which directly impacts user-friendliness [78].

Upon the construction and validation of the surrogate model, optimization processes are implemented. These processes are selected based on several criteria, including their objective (single-objective or multi-objective), convergence properties, stability, and their capability to identify global or local optima.

2.4.1. Design of Experiments

The DoE refers to the strategic allocation of training data points within the design space [77]. This process significantly impacts both the computational cost and the quality of the resulting surrogate model. Generally, four DoE methods are utilized, as illustrated in Fig. 2.12.



(a) Full Factorial Sampling (b) Monte Carlo Sampling (c) Latin Hypercube Sampling (d) Sequential Sampling

Figure 2.12.: DoE methods

The most straightforward DoEs are *Factorial Design Plans*, which position samples at the corners or edges of the design space (Fig.2.12a). These plans allow for the estimation of main effects and interactions but become impractical for a large number of input variables or detailed analyses due to the excessive number of required samples [77, 79].

To mitigate the excessive sample requirement, *Random Sampling*, such as Monte Carlo Simulation, can be employed (Fig.2.12b). This method assumes that design variables follow a uniform distribution within a specified range, placing designs randomly in the design space. While this approach enhances the detection of interactions, insufficient sampling can lead to clusters and gaps, making some areas less observable. Additionally, false correlations between input variables may occur, rendering the surrogate models unusable. [79]

Latin Hypercube Sampling (Fig.2.12c) ensures more uniform spacing compared to Monte Carlo methods and minimizes potential false correlations between input variables. This method is more efficient and reliable and recommended for up to 50 input variables. [79, 77]

In many applications, even a Latin Hypercube Sampling results in an excessive number of designs. To address this, *Sequential Sampling* is widely used (Fig.2.12d). This method involves creating a coarse initial mesh, identifying the optimization path, and iteratively refining the relevant area. Thus, non-favourable or irrelevant areas are excluded, significantly reducing the required number of designs. [77, 80, 81]

2.4.2. Training Data Acquisition

With the samples generated by the DoE, their response values are obtained through either experimental tests or simulation techniques, with the latter being more widely adopted due to their relatively lower costs. To ensure a suitable dataset, it is crucial to minimize external disturbances, as the surrogate model only accounts for the specified input variables. This requirement, coupled with the large number of experiments or simulations, typically necessitates fully automated setups.

For compressor performance prediction, 3D CFD simulations are commonly utilized [6, 74, 7, 76, 75]. However, alternative methods such as 1D or meanline calculations, as well as test-based data, are also utilized, depending on the design phase and the specific objectives of the surrogate model.

2.4.3. Model Identification and Validation (Metamodelling)

With the initial designs created and their responses obtained, all necessary data is available for generating and evaluating the surrogate model. The selection of an appropriate model algorithm depends on various factors such as the amount of available designs, number of input and output parameters, level of noise and gradient of the approximated function. Commonly used model algorithms include, but are not limited to, the following methodologies or their derivatives:

- Polynomial Regression
- Moving Least Squares
- Kriging
- Artificial Neural Networks

The *Polynomial Regression* is a widely used surrogate model when all basic relationships between input and output parameters are known. The regression coefficients are typically calculated using the least squares of error method. As the number of variables or the polynomial degree increases, the required amount of training points rises significantly. Therefore, polynomial regression is normally limited to second order polynomials and linear coupling terms. [81, 82]

An adaption of the polynomial regression is the *Moving Least Squares* approximation. Similar to polynomial regression, the basic function includes linear and quadratic terms, but it incorporates position-dependent weighting functions. This addition allows for efficient smoothing of noisy data. [79]

In many engineering applications, the *Kriging* approach is favored for its robust interpolation capabilities. The core principle of the algorithm is that data between training points can be interpolated by applying weighting factors based on the distance to the surrounding training points. The weighting factor increases as a training point gets closer to the approximation area. Consequently, the training points become an integral part of the model, and the prediction error becomes zero at each training point. [81, 82, 77]

Artificial Neural Networks differ from other surrogate models as they are inspired by the biological nerve system. Various network types exist, with the *simple Feed Forward Network* being one of the most common. This network consists of an input layer with as many neurons as variables, an output layer with one neuron corresponding to the

output parameter, and several hidden layers, but typically not exceeding two. Each neuron at position $k + 1$ is activated based on a weighted sum of the preceeding neurons at position k. The individual weighting factors of each neuron are determined through the training process, which minimizes the error between predictions and training data. This training usually requires large datasets and significantly more computational power compared to other approaches. Artificial neural networks are insensitive to single errors and disturbance variables in the training data, making them suitable for complex tasks. Additionally, they outperform other surrogate models when dealing with steep gradients. [82]

With many different surrogate models available, it is crucial to evaluate not only the predictive capability of a single model but also to compare its performance with other types. The most straightforward method for this comparison is to use the *Coefficient of Determination, CoD*, as shown in equation 2.23.

$$CoD = 1 - \frac{SS_E}{SS_T}, 0 \leq CoD \leq 1 \tag{2.23}$$

Here, SS_E represents the sum of squares due to error, and SS_T corresponds to the total sum of squares. The closer the CoD is to one, the better the approximation is expected to be. However, this is not always the case, and the value can be misleading. Firstly, if overfitting occurs in polynomial regression, the *CoD* will approach one. Secondly, Kriging-based models inherently include the original design samples, also resulting in a *CoD* value of one. Thus, the CoD should not be used to evaluate the approximation quality of surrogate models. [78]

For a more general and reliable evaluation of surrogate models, the *Coefficient of Prognosis, CoP*, eqn 2.24 is recommended.

$$CoP = 1 - \frac{SS_E^{Prediction}}{SS_T}, 0 \leq CoP \leq 1 \tag{2.24}$$

Rather than using the direct fitting error, the prediction error $SS_E^{Prediction}$ is utilized. To calculate this value, a cross-validation scheme is applied, where the design points are divided into groups that construct the surrogate model and groups that are solely used to assess the prediction performance of the derived model. As a result of this scheme, the CoP becomes independent of the model type and is much less sensitive to overfitting. Therefore, it is used as the key indicator in automated surrogate modelling systems. [79, 78, 83]

2.4.4. Optimization Methodologies

With the surrogate model constructucted and its predictive accuracy in the design space confirmed, optimization procedures can be applied to identify the optimal solution to a given set of objectives and constraints. The objectives are usually formulated as mini-

mization tasks. Figure 2.13 shows typical minimization algorithms and their respective application area.

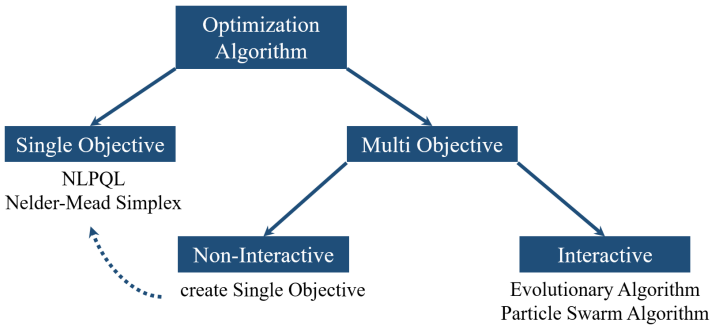


Figure 2.13.: optimization algorithms

For single objective optimization, a gradient-based method such as *Nonlinear Programming by Quadratic Lagrangian, NLPQL*, can be employed. This method approximates the derivative of the objective function and searches for the next local optimum. NLPQL is highly efficient for optimization tasks with fewer than 20 input variables and low noise levels. For higher noise levels, the differentiation interval becomes crucial as too small intervals can lead to solver divergence.[79]

A commonly used gradient-free method is the *Nelder-Mead Simplex* algorithm [77]. This algorithm uses a simplex to evaluate the objective function and converge towards its local optimum. Its independence from gradients makes it much more robust to solver noise and inconsistencies in the objective function due to failed designs. [80]

In many practical engineering cases, optimization tasks involve multiple objectives and constraints, necessitating the use of specific multi-objective solvers. These solvers are classified in non-interactive and interactive methods.[79]

Non-interactive methods transform multi-objective tasks into single-objective tasks. The two most common approaches are to designate one optimization target and reformulate the other objectives to constraints, or to introduce an optimization function with individual weightings for each objective. Subsequently, single objective methods are applied to find the optimal solution. However, both approaches require extensive knowledge about the optimization potential and a clear understanding of the importance of each objective, which is often not available at the beginning of the optimization process. Therefore, interactive methods such as Pareto optimization are applied. [79]

In a Pareto optimization, a design a is considered dominant against another design b if it is feasible, equal or better in all objectives, and better in at least one objective. As a result of the optimization, a Pareto front forms, with each design representing an optimal solution. This front allows for the investigation of conflicting objectives and the design space, facilitating the understanding of their relationships. Based on these findings, non-

interactive methods can be set up if required. [79]

For Pareto optimization, nature-inspired optimization processes are often employed. [79]

Evolutionary Algorithms are inspired by the process of natural selection and genetics. After initializing a random first population, all individuals are evaluated, and the best individuals are selected for reproduction. This process continues until stagnation is achieved. Random mutations prevent the solver from converging to a local optimum. This method allows the solver to handle a large number of failed designs and is considered one of the most efficient approaches for optimization tasks with many design variables and constraints. [79, 80]

The *Particle Swarm Algorithm* is inspired by the behavior of schools of birds and fish [77]. A swarm of particles moves through the design space, with each particle's position updated based on the best global position (leader) and its own best position from previous steps. Its performance is comparable to evolutionary algorithms but deteriorates when dealing with discrete variables or numerous constraints. [79, 80]

Since many technical parameters, such as dimensions, are discrete rather than continuous values, evolutionary algorithms are the preferred optimization tool.

3. Methods

This chapter introduces the methodologies employed to acquire the data for this work. The first section details the experimental facilities utilized, namely the Hot Gas Test Rig (HGTR), Electric Test Rig, and Engine Test Rig (ETR). The second section introduces the simulative approaches, specifically Reynolds-Averaged Navier-Stokes (RANS) and Unsteady Reynolds-Averaged Navier-Stokes (URANS) simulations.

3.1. Testing

The highly complex aerodynamic and thermodynamic effects in applied turbomachinery make the derivation of physical and mathematical models challenging and prone to modeling errors [84]. Consequently, much of the research and development on compressors relies on experimental results, particularly when investigating transient effects such as stall or surge. Depending on the specific effect under investigation or the development target, various test rigs are employed. These test rigs are discussed in the following subsections.

3.1.1. Hot Gas Test Rig

Compressor testing is usually done on a HGTR. As the name implies, hot gas, generated by combustion of natural gas or diesel fuel, is used to drive the turbocharger. The test rig used in this work is a fully automated industrial test bench and optimized for thermodynamic turbine and compressor measurements.

The standard test bench setup is shown in Figure 3.1, where the compressor operates in an open-circuit system. Air is drawn from the conditioned test cell (1) into the inlet ducting (2) and enters the compressor (3). It then passes through the measurement ducting (4) and is expanded in a pneumatically operated throttle valve (5). It is then released into the atmosphere through a chimney (6).

The turbine (7) is driven by a natural gas burner (8) which provides a hot gas comparable to the exhaust gases of an engine. Typically, turbine inlet temperature is set to 873°K.

Inlet static pressure (a) is pneumatically averaged and measured $2d_1$ upstream of the compressor inlet. The inlet temperature is measured with PT-100 sensors (b) in the same measurement plane.

T_2 (c) and p_2 (d) are measured $5d_2$ downstream of the compressor outlet cone. p_2 is similarly measured as p_1. T_2 is measured with six PT100 sensors, which are positioned in a specific form to take the swirling flow of the compressor into account.

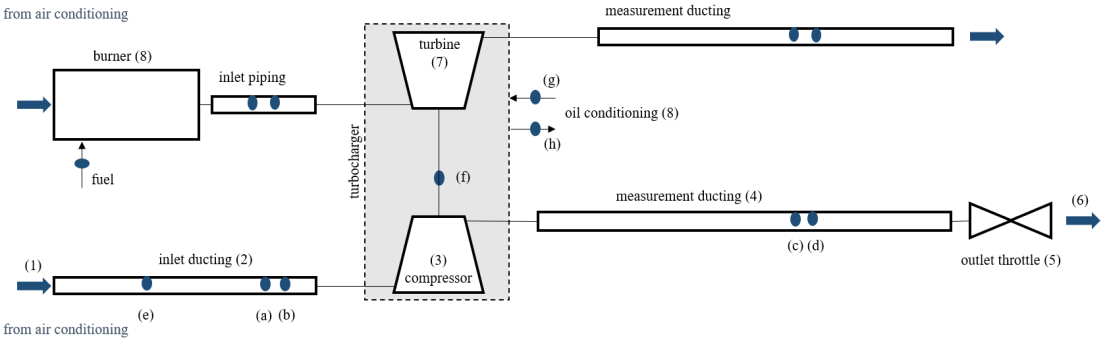


Figure 3.1.: hot gas test rig

Since neither total temperature nor total pressure can be precisely measured, a fully developed flow is assumed and total values are iteratively calculated, following common industrial best-practice guidelines [85].

The mass flow rate is measured by a SensiFlow flow meter (e) located at the beginning of the inlet ducting.

As every turbocharger is manufactured with an internal speed sensor (f), the test rig does not actively measure the circumferential speed but acquires it from the turbocharger.

The lubricant for the turbocharger bearing system is provided by the test bench (8). Oil mass flow, inlet- and outlet pressure and temperatures (g, h) are monitored and logged during a test run.

Surge is detected when the pressure fluctuations are greater than five percent of the sliding average at pressure outlet, or if the outlet temperature exceeds 483°K. The temperature limit is dictated by the mechanical robustness of the compressor wheel and usually leads to a "kinked" surge line for the highest circumferential speed. It is emphasized that this "kink" is not the aerodynamic stability limit, which is the common surge definition.

Internal measurement standards and procedures [86] surpass the current industry standard for turbocharger testing [87], for which the HGTR is fully compliant to.

3.1.2. Electric Test Rig

Although a HGTR powers a turbocharger in the correct thermodynamic way, it introduces errors when the compressor as a component itself is evaluated. The two main drivers are heat transfer from turbine to compressor [28, 88, 89, 27, 90, 91], and varying turbocharger speeds due to control lag [86]. Both sources of error can be minimized when an electric test rig is used, see Figure 3.2.

On the electric test rig, an electric motor with a gearbox (1) drives the compressor (2).

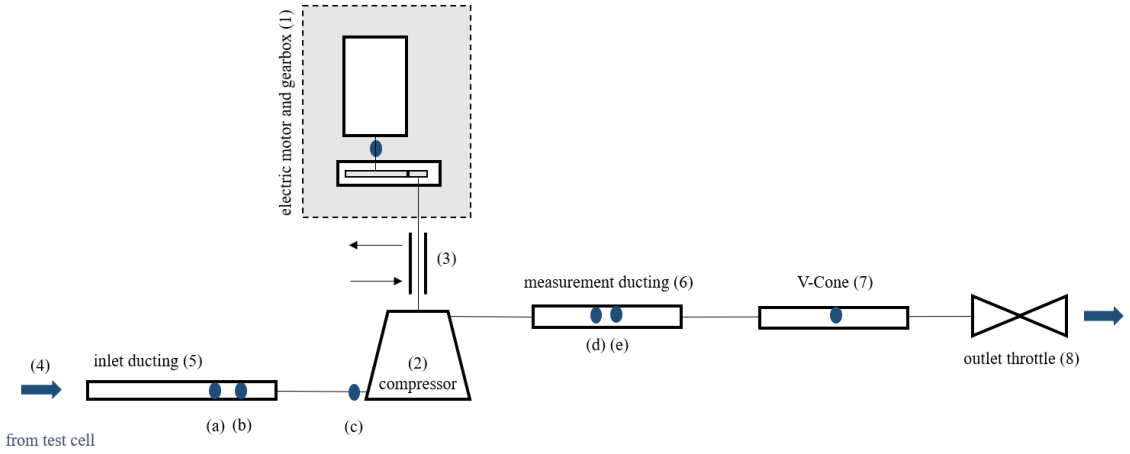


Figure 3.2.: electric test rig

The electric control and known transmission ratio make a speed sensor redundant. A special shaft (3) connects gearbox and compressor, while using the same turbocharger bearing system.

Air is sucked in from the conditioned test cell through a bell mouth (4) and enters the $6d_1$ long inlet ducting (5) equipped with sensors for p_1 (a) and T_1 (b). An additional type-K thermocouple (c) is located right at the compressor inlet to detect begin of backflow.

At the compressor outlet, the air enters the measurement ducting (6), where p_2 (d) and T_2 (e) are measured $5d_2$ downstream. Mass flow rate is measured with a V-Cone (7). The air is released to the test cell via a butterfly valve (8).

The electric test rig generally meets the test measurement and accuracy requirements as stated in Section 4 of SAE J1826 [87].

3.1.3. Engine Test Rig

The ETR, Fig. 3.3 is used to get closer to the real turbocharger working environment and gain information about the compressor operation in a transient environment. The test rig contains of a complete engine (1), where the intercooler (2) is swapped to a watercooled type to allow operation in a test cell. The engine is coupled to an electric brake (3) to control the engine operation point. Extensive intake conditioning (4) and aftertreatment systems (5) allow combustion-related research.

Although compressor inlet and outlet temperature (a, b), pressure (c, d), and turbocharger rotational speed (e) are measured, they cannot be compared to HGTR results. Due to the very limited space and different ducting, measurements only allow a qualitative comparison between different compressors on the engine.

The ETR employed in this study is a state-of-the-art test bench, utilized for heavy-duty engine certification in compliance with UNECE R49 [92]. Furthermore, it conforms to the

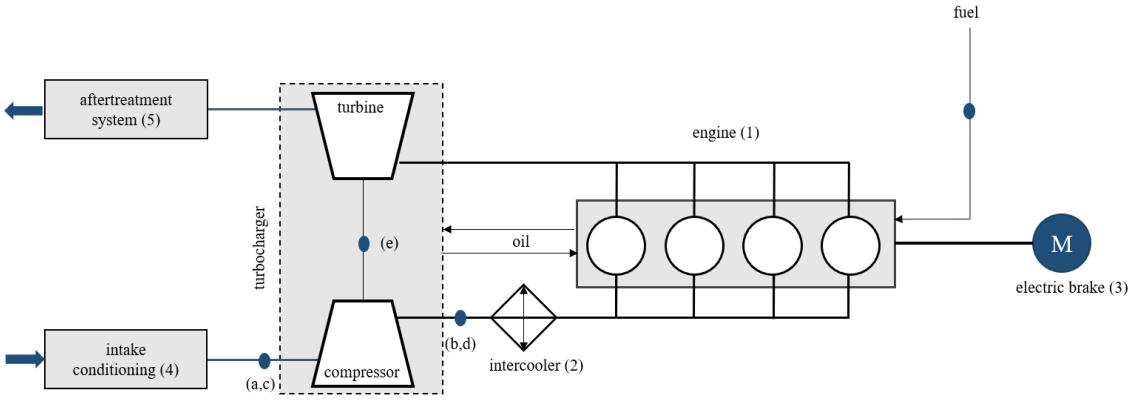


Figure 3.3.: engine test rig

specifications outlined in ISO 15550 [93].

3.2. Computational Fluid Dynamics

While experimental results are widely acknowledged as the most reliable, they come with significant downsides. The need for prototypes and test benches incurs substantial costs and time. Additionally, acquiring test data is not always feasible, for example when investigating effects within the rotor.

On the other hand, simulation capabilities have substantially improved alongside advancements in computational power [26]. Consequently, validated simulations now play a crucial role in understanding flow behaviors and enhancing compressor designs [84].

3.2.1. Reynolds Averaging

CFD faces the challenge of balancing computational cost with the accurate representation of physical phenomena. While a Direct Numerical Simulation (DNS) solves the Navier-Stokes-Equations without introducing turbulence modeling assumptions, it is currently not feasible for technical applications due to the complexity of turbulence and the resulting computational effort. [21]

In many practical turbomachinery applications, the primary interest lies in the steady mean flow characteristics. Hence, RANS equations are utilized to balance accuracy and computational cost. [94, 18]

Reynolds Decomposition separates the flow field into a temporal mean value and a fluctuating component, as shown in equation 3.1 [21, 18]. ϕ represents a flow variable, and $\overline{\phi}$ and ϕ' are its time-averaged and fluctuating components. The time-average of the fluctuating component must be zero [18].

$$\phi = \overline{\phi} + \phi' \tag{3.1}$$

When applied to the Navier-Stokes equations, Reynolds Decomposition introduces an additional term in the momentum equation known as Reynolds stress [18]. This is demonstrated in equation 3.2 for incompressible flows without a source term for sake of clarity.

$$\bar{\rho}\left(\frac{\partial \bar{U}_j}{\partial t} + \bar{U}_i \frac{\partial \bar{U}_j}{\partial x_i}\right) = -\frac{\partial \bar{p}}{\partial x_j} + \frac{\partial}{\partial x_i}\left[\overline{\tau_{ij}} - \bar{\rho}\overline{u_i' u_j'}\right] \tag{3.2}$$

This term ($\bar{\rho}\overline{u_i' u_j'}$) renders the system of equations underdetermined, necessitating additional equations for closure [95]. Thus, turbulence models are employed, establishing correlations between the unknown Reynolds stresses and the known mean flow components [18]. This approach allows for the consideration of turbulent flow fluctuations without direct modeling. As a result, the required spatial and temporal grid sizes can be significantly reduced, leading to the desired reduction in computational cost [21, 96].

3.2.2. Turbulence Models

Many turbulence models apply the Boussinesq hypothesis, which assumes that the transport mechanism of turbulent velocity fluctuations is analoguous to the molecular transport in an isotropic, Newtonian fluid. This is mathematically represented by equation 3.3. [18]

$$\bar{\rho}\overline{u_i' u_j'} = -\overline{\rho} \cdot \nu_T \left(\frac{\partial \overline{U}_j}{\partial x_i} + \frac{\partial \overline{U}_i}{\partial x_j}\right) \tag{3.3}$$

In this equation, ν_T represents the eddy viscosity, which is a property of the flow rather than the fluid itself, and thus must be calculated.

While numerous methods have been proposed in the literature, only a few have gained widespread use. The most common are the $k-\epsilon$, $k-\omega$, and SST-$k-\omega$ models, along with their derivatives. These models calculate ν_T using turbulent kinetic energy k and either turbulent dissipation ϵ or turbulent characteristic frequency ω.[21]

Compared to other approaches, such as analytical or one-equation models, these two-equation models achieve better accuracy and can be applied in complex environments. They are also less computationally demanding than more sophisticated multi-equation models such as the Reynolds Stress Model (RSM). [18, 12]

As pointed out in [12], there is no perfect turbulence model, and selection is based on individual calibration material and experience. $k-\epsilon$ models have been employed in previous compressor flow field investigations relevant to this work [7, 6, 97, 44] and

are commonly used in many industrial applications [96, 21]. Thus, in this work, the Navier-Stokes equations are solved using the *realizable* $k-\epsilon$ RANS model in the commercial solver Siemens Simcenter StarCCM+. Compared to the *standard* $k-\epsilon$ model, some model constants are replaced by functions, which help in obtaining physically realistic turbulence values under certain flow conditions [21]. This also improves the stability of the solver [98].

3.2.3. Discretization and Computational Grid

To solve the resulting set of Partial Differential Equations (PDE), numerical schemes are applied that find the solution through iteration. Therefore, continuous description of the equations is brought into a discrete form. The resulting equations are then applied to a computational grid, which represents the flow field with a finite number of points in time and space. FVM is the most utilized method, as it is, by design, suitable for conservative discretization [21, 18, 96].

The computational grid divides the flow region into a set of control volumes that do not overlap or exhibits gaps [21]. The two main grid types are structured and unstructured grids [21, 18].

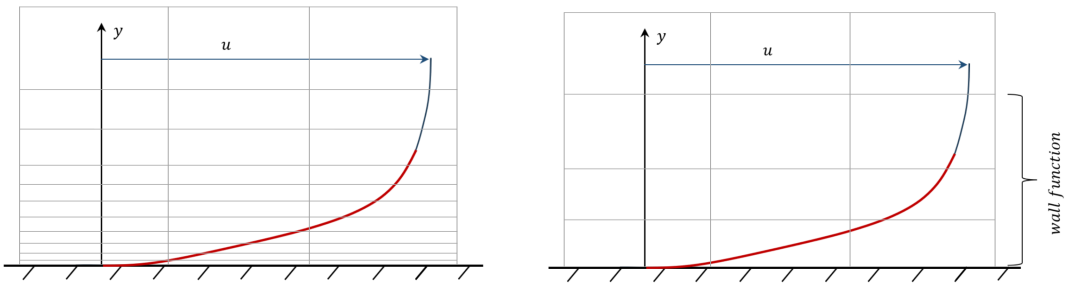
- *structured grids* exhibit a uniform topology, and control volumes are placed in a regular manner. They typically use hexahedrons or square volume types. [21]
- *unstructured grids* do not exhibit uniform topologies and can use different volume types such as tetrahedrons and hexahedrons. These grids are flexible and easy to automate and hence widely utilized, however, they are typically more computationally expensive than structured grids. [21]
- *hybrid grids* are a special case of unstructured ones [12] and combine either structured with unstructured grids, or stack different structured grids. This can be advantageous if, for example, large fluid volumes have to be discretized.

The grid density heavily influences the outcome and result of a simulation [12]. If the grid is too coarse, key flow characteristics might not be well captured, if at all. A very fine mesh, on the other hand, can lead to extensive computational requirements or numerical divergence.

Also, the quality of the control volumes play an important role. The more the shape of the cell differs from the generic baseline, the worse the numerical result becomes. [12]

As discussed in Chapter 2, the flow field exhibits large gradients near walls, encompassing the viscous sublayer, transition area, and turbulent main flow. This presents significant challenges for turbulence models, which are usually only valid in fully turbulent flows [21]. To address this, two approaches are employed: high Re meshes and low

Re meshes. Figure 3.4 illustrates these two approaches.



(a) low Re mesh (b) high Re mesh

Figure 3.4.: near wall modeling

The non-dimensional distance to the wall, y+, defined in equation 3.4, is the key to understand and distinguish between the two approaches:

$$y+ = \frac{yu_t}{\nu} \tag{3.4}$$

In this equation, the friction velocity u_t is calculated from the wall shear stress, and ν is the kinematic viscosity, a fluid property ($\nu = \mu/\rho$).

Low Re meshes discretize the spatial domain up to the viscous sublayer and employ specialized low-Re turbulence models to directly resolve the wall flows. The y+ value is approximately 1. [21]

High Re meshes, on the other hand, use the *law of the wall* to model the boundary layer. Analytical functions approximate the boundary flows up to the point where a fully turbulent flow is developed, allowing classical turbulence models such as the $k-\epsilon$ model to be valid. Typical y+ values range from 30 to 300, depending on the specific wall and blend functions used, which is often solver-related. [21]

Thus, the y+ significantly influences the simulation accuracy and the mesh has to be carefully aligned with the numerical approach and the effects under investigation. A low Re mesh is considered more accurate than high Re meshes, but might be unreasonable to deploy because of excessive computational costs [7].

In the work herein, the grid generation is fully automated as outlined in [99] to allow comparability of simulation results across different compressor designs. The proprietary CAD tool *CTRL-X* provides the whole fluid domain and consists of the full-annulus compressor fluid volume together with information on required grid structure and size.

The grid is auto-generated in StarCCM+ and discretizes the fluid volume to approximately 8 million cells, with the critical regions around the impeller blades refined. Polyhedral volume mesh is used with a prism layer mesh for the boundaries. The wall $y+$

across the domain ranges between 30 to 80. The walls are treated as hydraulically smooth and adiabatic, and a no-slip condition is applied. An all-$y+$ wall treatment is used for numerical stability while providing reasonable results [98]. Figure 3.5 shows a representative mesh with some of the inlet and outlet piping included.

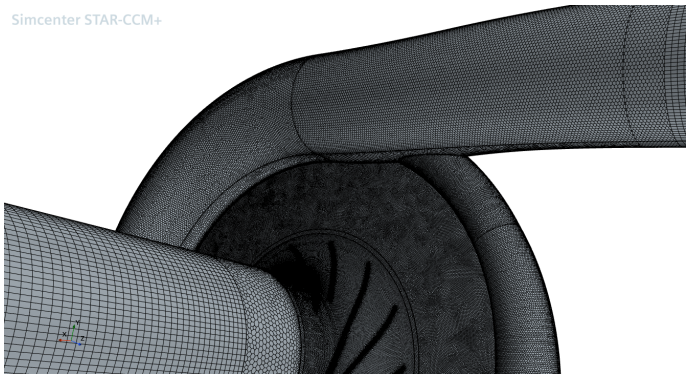


Figure 3.5.: Representative CFD mesh. Where possible, structured mesh sections are applied to improve accuracy and numerical efficiency.

3.2.4. Rotor Interaction and Interfaces

To model rotor movement in steady-state simulations, two methods can be utilized: the frozen rotor approach and the mixing plane approach. In both cases, a rotating reference frame is applied to the rotor to simulate its movement. [98]

In the frozen rotor approach, a direct interface between the rotor and stator exists, allowing flow information to pass directly from the rotor cells to the adjacent stator cells. Since the rotor mesh does not move, the solution depends on the initial positioning of the rotor blades relative to the stator. [98]

Conversely, the mixing plane approach uses an interface that circumferentially averages the flow profile, mitigating the influence of the relative positioning between the rotor and stator. However, this method cannot capture wake effects, as they are averaged out in the mixing plane. [98]

The mixing plane approach is typically employed in RANS simulations (see setups in [7, 6, 100]) and generally seen as good practice [12]. Consequently, in this work, the mixing plane approach is utilized. Its settings and an extensive validation are published in [7].

3.2.5. Boundary Conditions

Boundary Conditions (BC) are used to define the operating point of the compressor in the simulation. For the inlet, a non-reflective total pressure $p_T = 1bar$ and total temperature $T_T = 25°C$ BC are taken, similar to the inlet conditions at the HGTR and ETR. The outlet

BC is set for mass flow rate.

3.2.6. Transient Simulation

RANS simulations loose their applicability at specific compressor operating points, particular in the stall regime. This limitation arises due to unsteady flow phenomena and high levels of swirl [101, 102]. Consequently, while RANS simulations can be reasonably accurate, their reliability diminishes as the compressors operating point approaches surge.

Thus, simulation types that account for transient effects are utilized. The most common ones are Unsteady RANS (URANS), LES or Detached Eddy Simulation (DES), each having its own strengths and weaknesses. While URANS is numerically robust, it is unable to capture large separations behind obstacles in the flow field [103]. For such cases, LES can be utilized, but lacks numerical stability and introduces significantly higher computational demands [103, 104]. DES combines URANS and LES by applying URANS near walls and LES in the main flow field, hence focusing on each models strength. However, this approach rises issues regarding meshing and theoretical order of accuracy [103]. As a result, URANS is often preferred over LES and DES [62, p. 3] and has become current industry standard for transient CFD. Nevertheless, it is still seen as a last design phase method and not utilized in design iterations [12]. In literature, URANS has been extensively used to simulate centrifugal compressors in transient operation, stall or surge [1, 13, 105, 106, 35].

It is important to note that URANS, unlike steady RANS, does not rely on time-averaging but uses ensemble averaging. Here, the instantaneous flow variables are decomposed into a mean and a fluctuating component based on statistically equivalent realizations of the unsteady flow. This preserves the large-scale, coherent unsteady motions that would be suppressed by time-averaging in a steady formulation.

In the work presented herein, The Navier-Stokes equation is solved using the *transient realizable $k-\epsilon$ RANS model* [98]. The spatial grid is created upon the same criterions as in the steady simulation case.[10] However, the mesh may also include the relevant parts of inlet and outlet ducting of the test bench.

The transient character of the model is defined by the temporal discretisation and the motion of the impeller. An implicit unsteady, second order temporal discretization scheme with 40 inner iterations is used. The movement of the rotor is modelled with Rigid Body Motion (RBM) using a fixed mesh. The time step size is subject to the effect under investigation and grid independence study presented in chapter 4.

[10] As one aspect of this research is industrial applicability, a low Re mesh is not suitable as it significantly increases required computational ressources: computational effort is proportional to the square of the number of grid points and inversely proportional to the time step size. The amount of grid points increases massively with the low Re mesh and the time step must be reduced in order to keep the CFL-number small.

At the inlet, a non-reflective total pressure and temperature BC is set. At the outlet, a mass flow boundary condition is set, following the discussion and procedure in [17].

Each URANS simulation comprises two distinct phases. The initial phase involves a mass flow ramp-up, during which the outlet mass flow boundary condition linearly increases from zero to the target mass flow rate. This gradual increase prevents numerical instability. Subsequently, the mass flow rate is maintained at a constant level, marking the commencement of the physics evaluation phase. During this phase, the compressor, having reached its choke limit, follows its speed line towards surge as the backpressure rises due to mass accumulation at the outlet. Consequently, the compressor will either stabilize at a steady operating point or transition towards surge.

4. Analysis of the Surge Trigger of a High-Performance Compressor

Understanding the mechanisms that trigger surge in a representative compressor of the investigated compressor family is essential for both knowledge-based and data-driven optimization strategies. In knowledge-based approaches, identifying the dominant physical phenomena enables the development of effective countermeasures and further performance improvements. In contrast, data-driven methods require the information to ensure that relevant geometric parameters are appropriately varied within the DoE.

To enable a detailed flow field analysis, a URANS simulation is conducted. Consequently, this chapter follows three main objectives:

1. Validation of the URANS Setup
2. Analysis of the Surge Trigger Mechanism
3. Improvement Recommendations

The *Validation of the URANS Setup* involves a grid independence study, comparison with transient and steady-state data from the electric test rig and HGTR. This ensures that the simulation setup is sufficiently accurate to capture the dominant physical mechanisms driving surge.

The *Analysis of the Surge Trigger Mechanism* is connected to the validation as it compares the effects seen in the URANS with findings from literature using LES or PIV. From this, the chain of events leading to surge is derived.

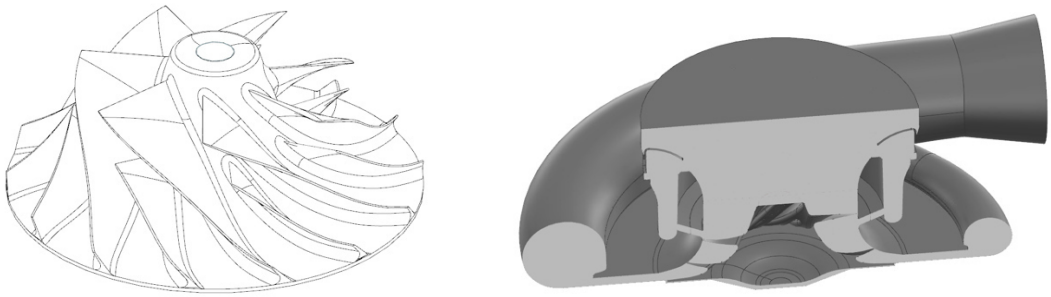
The *Improvement Recommendations* are based on the surge mechanism analysis and identify optimization potential for surge, efficiency, and choke. Each compressor component -ported shroud, impeller, diffuser and volute- is evaluated, with new solutions proposed or linked to existing literature where applicable.

Additionally, an *Addendum: Investigation of Automated Surge Trigger Detection* examines methods proposed in grey literature for automated surge detection in simulations. Given the extensive data generated by URANS, rule-based detection approaches are appealing. With the actual surge trigger mechanism derived and validated, three detection methods are applied to the URANS and their results compared.

4.1. Compressor Design

For the URANS analysis, a state-of-the-art turbocharger compressor designed for a 6 cylinder, 15l on-highway heavy-duty Diesel engine is used. It has a 7+7 impeller, a vaneless diffuser, a linear A/R ratio volute, and a class-typical ported shroud with noise

ring. Inlet diameter is ~64mm, and the design speed range ~40.000 – ~120.000rpm. Figure 4.1 shows the compressor fluid volume (inlet and outlet ducting not visualized) and impeller. This baseline compressor is referenced to as *compressor B*. It was developed by the industrial sponsor using an automated optimization approach and manually improved to achieve wider map width.

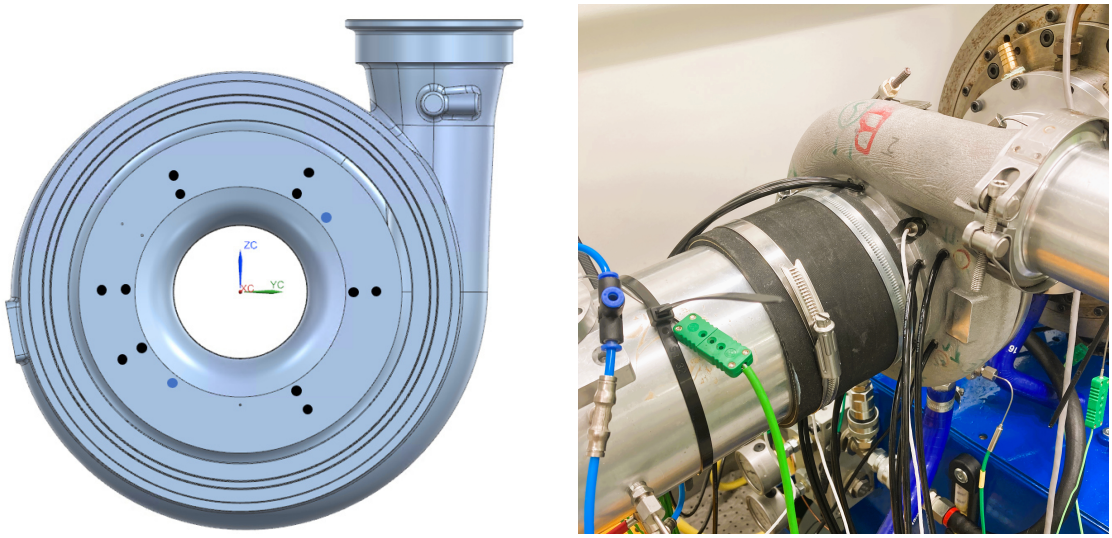


(a) impeller (b) fluid volume

Figure 4.1.: fluid volume compressor B

4.1.1. Hardware Setup

The compressor used for testing is equipped with static pressure transducers. Fig. 4.2 shows the positioning of the sensors, and the manufactured and equipped compressor housing.



(a) sensor positions; black: steady-state, blue: transient (b) compressor w. sensors mounted on electric test rig

Figure 4.2.: hardware compressor B

In order to minimize eigenfrequency effects and misleading measurements of the transient pressure sensors, the maximum permitted length of the holes is calculated based on

the reshaped standing sound wave equation 4.1.

$$l = \frac{c}{4 f_{sampling}} \tag{4.1}$$

Using the most critical values for the speed of sound and sampling frequency, the holes must be shorter than 1.95mm to avoid the first harmonic. Hence, the maximum depth of the hole is set to 1.5mm which ensures a correct static pressure measurement, while providing enough safety margin against standing wave interference.

4.2. Validation of the URANS Setup

4.2.1. Grid Independence Study

The simulation was proven mesh independent in [107]. It falls within typical range for full-annulus meshes of compressors with comparable geometrical dimensions [35].

A time step independence study is conducted to ensure confidence in the temporal discretization. Therefore, the same baseline mesh is used, but with different time steps of 10°deg, 5°deg, and 1°deg. Similar to the mesh independence study, global data does not vary significantly with different time steps, as shown in Figure 4.3.

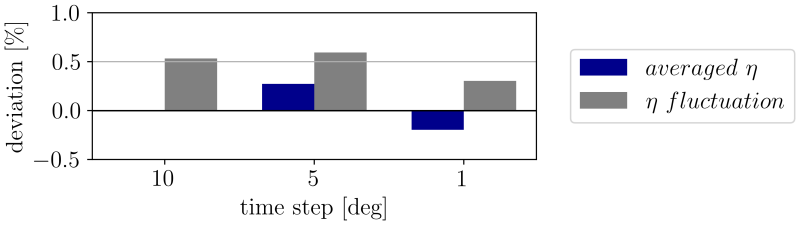


Figure 4.3.: Time step independence study. Averaged isentropic, adiabatic efficiency and converged fluctuation.

While this could suggest the use of a 10°deg time step size, it must be emphasized that only global data is compared. Thus, the internal flow features can vary, as highlighted in [108], concluding independence is achieved upon 15 time steps per passage. Key stall characteristics are evident at three steps per passage. Considering the 7+7 impeller geometry used in the study herein, two grid sizes are defined depending on the effect under investigation:

- For global performance data comparison, a 10°deg time step is applied to balance numerical cost and accuracy.
- For stall phenomena, a 1°deg time step is applied.

4.2.2. Comparison with Electric Test Rig Data

The electric test rig closely resembles the URANS setup, providing an environment that approximates adiabatic and speed-constant conditions. Therefore, detailed flow field val-

idation is conducted using the electric test rig with the compressor speed being set to 60%.

The initial validation step involves measuring and comparing the steady-static pressure field within the diffuser. Therefore, twelve static pressure transducers at diffuser inlet and outlet are utilized to determine the deviation between test and simulation.

Figure 4.4 illustrates that the simulated static pressure aligns very well with the measurements, with deviations at the diffuser outlet remaining below 0.5%. At the inlet, deviations increase up to 2.5%. This is due to the proximity of the sensors to the impeller outlet, where steep pressure gradients are present, as depicted in the static pressure field generated by CFD. Thus, even minor discrepancies in geometric positioning result in notable variations. Therefore, it can be concluded that the URANS accurately captures the steady-state pressure distortion induced by the volute at the test bench's last stable operating point.

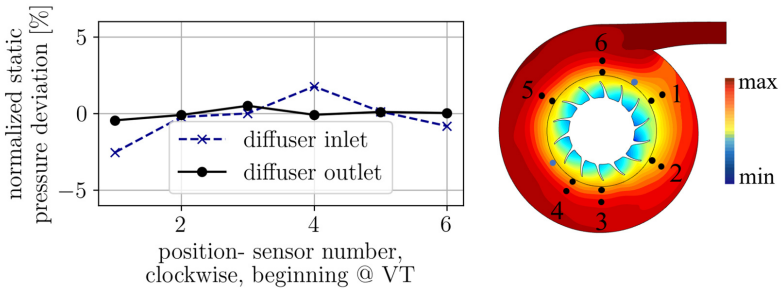


Figure 4.4.: Comparison of test and simulation steady static pressure in the diffuser, last stable operating point.

The second validation step involves the detailed comparison of the flow breakdown. In the simulation, the compressor is forced into stall by setting the mass flow BC slightly below its last known stable test bench point. Conversely, in the experiment, the throttle valve is incrementally closed. Two transient pressure sensors, shown in Fig. 4.4 as blue dots, record the static pressure signal at a sampling frequency of 50,000Hz.

To synchronize data, the first clearly detectable, high-order pressure fluctuation exhibiting a 180°deg phase shift is chosen as the reference point, as illustrated in Figure 4.5. The time window begins with the pressure spike resulting from the URANS BC alteration and ends after five fully developed stall oscillations. 0.2s later, the test encountered the first deep surge event.

From Figure 4.5 it is imminent that key characteristics are well captured:

- Before the emergence of the first clearly distinguishable waves, the pressure difference between the sensors gradually increases.
- a good match in the oscillation frequency and amplitude is observed once stall has developed. Notably, even the intersections between the sensor signals are captured

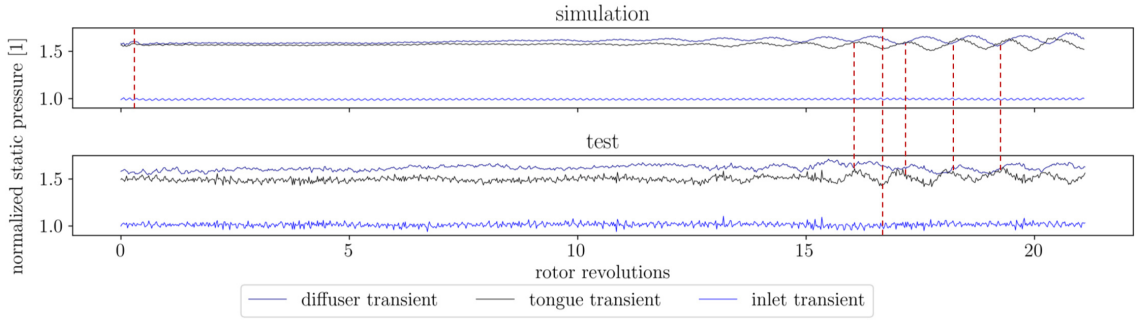


Figure 4.5.: Transient static pressure data. Data normalized with ambient static pressure.

in the URANS simulation, as shown by the last three red-dashed lines.

With the basic validity of the URANS stall inception mechanism confirmed, a detailed examination of the diffusor sensor data is conducted. A high-pass filter with a cutoff frequency of 300Hz is applied to all datasets, as in the experiment, an inlet pipe oscillation occurs at ca. 250Hz. The filtered results are shown in Figure 4.6.

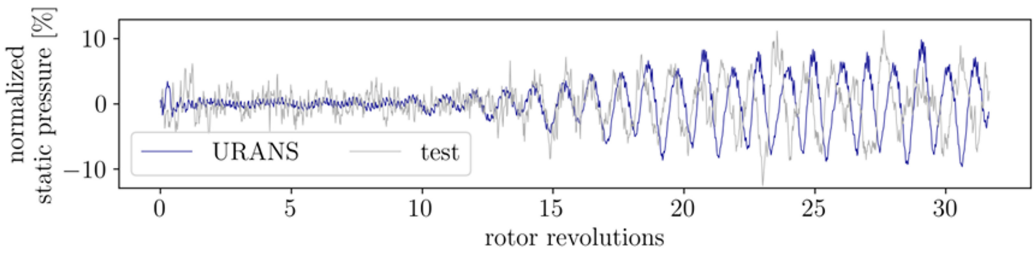


Figure 4.6.: Comparison of URANS and test data for the diffuser sensor. Data normalized with measured relative static pressure at last stable point, compressor outlet.

For the time-resolved data, it is important that the interval between the initial disturbance and the onset of oscillation in the simulation corresponds with the test data, where a pressure disturbance precedes the oscillation. In both scenarios, this does not indicate spike stall inception. In the simulation, the pressure spike arises directly from a change in the BC, whereas in the experiment, the pressure disturbance occurs several rotor revolutions before the plotted data. This disturbance then abruptly dissipates, akin to the spike in the simulation, and a long-wavelength disturbance emerges during the same period, reaching comparable amplitudes. Given the ideal conditions in the simulation and the unsteady nature of the test bench, it is concluded that the URANS model effectively captures the onset of stall.

Simulation and measurement data reveal a sudden phase shift at the 21 rotor revolution mark, followed by the observation of long - wavelength frequencies in the test signal. This discrepancy between simulation and test data is typical when classic surge occurs. With the initial stall fully developed, the test bench's increasing vibrations induce secondary flow breakdowns, which inherently cannot be captured by the simulation. Consequently, the pressure signals exhibit a drift. It is important to emphasize that this is not critical,

as the flow field at this stage has already entered the unstable regime, and any (random, uncontrollable) disturbance will amplify.

4.2.3. Comparison with HGTR Data

In engine applications, critical surge areas are usually located at compressor speeds exceeding 70% of the maximum speed, necessitating measurements with HGTRs. However, the nature of these rigs restricts detailed measurements, often allowing only global data comparisons. Thus, a global data simulation for one deep surge cycle at 86% speed, employing the 10°deg time step, is conducted to validate the modified setup.

The URANS setup includes the HGTR's downstream volume up to the throttle valve. The inlet is modelled as a 1.5m long pipe, providing sufficient volume to allow a surge oscillation [11].

From this, the deep surge frequency is determined to be 6.5Hz, closely aligning with the one measured at the HGTR (5.9Hz). Additionally, the choke point is well matched with the test data (+1.3%). Therefore, based on the available data, it can be concluded that the URANS setup is capable of capturing all relevant flow phenomena, even at high pressure ratios in HGTR environments.

4.3. Analysis of the Surge Trigger Mechanism

4.3.1. Physical Evaluation and Comparison with Literature

With the setup validated as grid-independent and accurately aligned with test data, the surge trigger at 86% compressor speed is examined. The analysis employs the same setup as used in the HGTR comparison, but the time step is decreased to 1deg. Figures 4.7 and 4.8 present detailed information regarding the velocity and pressure fields in the mid-diffuser plane across six relevant time steps. Table 4.1 provides the instantaneous mass flow rate of each time step.

time step	normalized instantaneous mass flow rate
a	64.1%
b	55.5%
c	51.8%
d	47%
e	41.4%
f	32%

Table 4.1.: Simulation time steps and instantaneous mass flow rate. a-c are globally stable, d-f unstable. b-e are timewise equally spaced. a is close to the design operating point, f is during impeller flow reversal. Data normalized with maximum choke mass flow.

As the mass flow is reduced by the outlet BC, the volute becomes mismatched and begins to operate as a diffuser (Fig. 4.8, timestep a-b). This leads to the development of

[11] The HGTR's extensive inlet piping is so dominant, that during a deep surge cycle, no relevant amount of fluid exits the system. This effect is logarithmic to volume and thus, beyond a certain point, any further increase in inlet volume does not alter surge frequency. In the CFD, this characteristic is used to reduce computational costs.

a strongly non-axisymmetric pressure field, which is consistent with experimental observations and extensively documented in literature [13, 109, 110, 14, 101, 12].

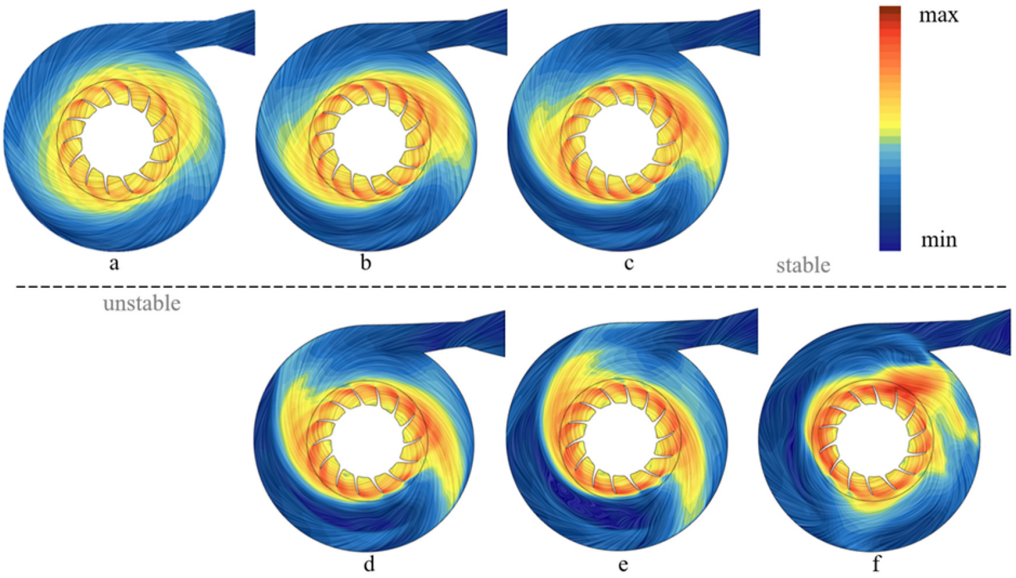


Figure 4.7.: Instantaneous velocity field at different time steps in the mid diffuser plane.

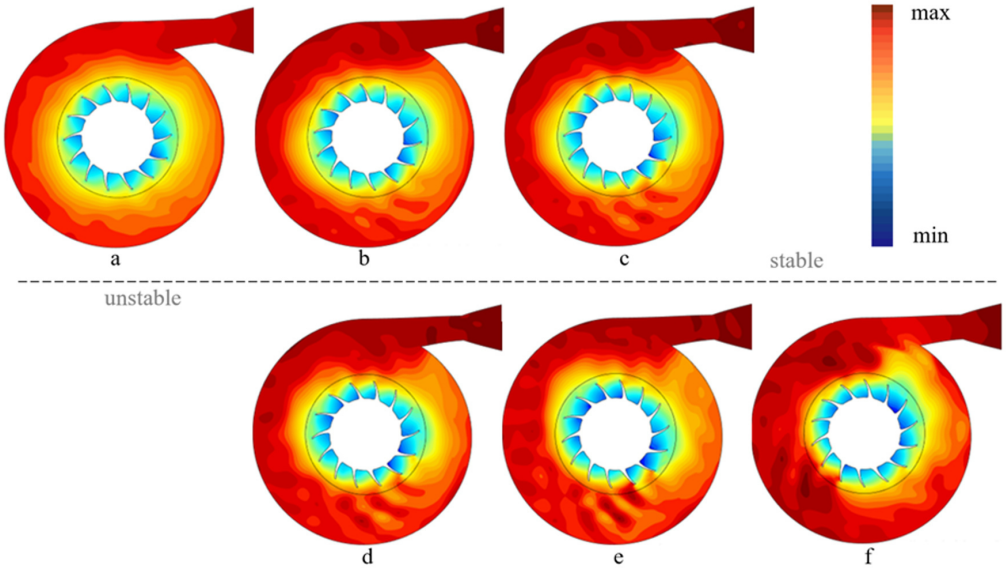


Figure 4.8.: Instantaneous static pressure field at different time steps in the mid diffuser plane.

As a result of this, a significant pressure gradient develops at the volute tongue (Fig. 4.8, timesteps b-e). This gradient induces a leakage flow from the volute outlet back into the tongue region, resulting in partial recirculation within the volute (Fig. 4.7, timestep b). This leakage flow is also captured in LES simulations [14, 110].

The low static backpressure behind the volute tongue (Fig. 4.8, timestep b) also results in an increased mass flow rate through the diffuser and exducer in this region (Fig. 4.7, timestep b). This effect is further intensified by the partial blockage of the diffuser outlet

caused by the volute recirculation.

As the mass flow rate in the diffuser decreases due to the discharge of accumulated flow and the subsequent increase in static pressure, the flow detaches and forms a stall cell at the four o'clock position (Fig. 4.7 and 4.8, timesteps b-c).

This separation causes the accumulation of flow exiting the impeller, which discharges approximately 90°deg phase-shifted as sufficient mass flow rate unblocks the diffuser (Fig. 4.7, timestep b-c). The partial closure of the diffuser is reported, amongst others, in [12] and is observable, albeit less pronounced, in the LES simulation in [14].

At some point, the non-axisymmetric pressure field in the diffuser begins to interact with the exducer. An initial impeller stall event occurs at the twelve o'clock position, where the static pressure seen by the passage is highest. However, this stall cannot develop due to the sudden pressure drop downstream the volute tongue, which enables full flow recovery (Fig. 4.8, timestep c).

The global flow breakdown initiates with the occurence of a second exducer stall originating from the main blade suction surface at the six 'o clock position at time step d. Figure 4.9 provides a detailed visualization of the separation, while Figure 4.10 illustrates the time-resolved progression of stall growth. It is evident that the instantaneous mass flow is initially dominated by the main passage (rotor revolutions 0-2), transitions through an intermediate phase (rotor revolutions 2-4), and subsequently becomes dominated by the splitter blade passage (rotor revolutions 4-6) as the main passage becomes obstructed by the stall (see Fig. 4.9). The mass flow rate plot also highlights the rapidly growing mass flow fluctuation from rotor revolution 3 on, providing strong evidence that this separation is in fact the trigger of the surge event.

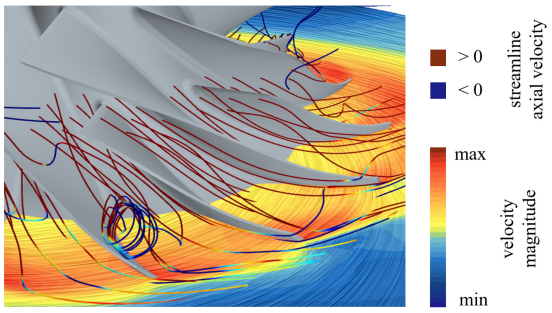


Figure 4.9.: Exducer stall begin, time step (d). Rotating frame streamlines and reference frame velocity convolution plot.

Figures 4.8 and 4.9 show that the exducer stall coincides spatially with the fully developed diffuser stall in the same region. However, it remains uncertain whether the diffuser stall alone is responsible for triggering the exducer stall. Due to the limitation of the URANS approach, small-scale vortical structures upstream the stall cell are not resolved. To address this, entropy plots are used as an indicator to visualize regions of

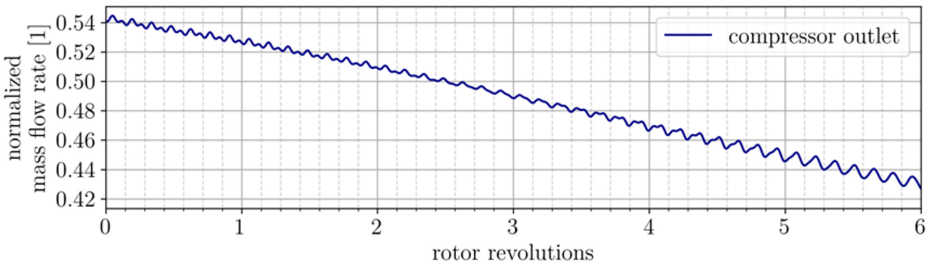
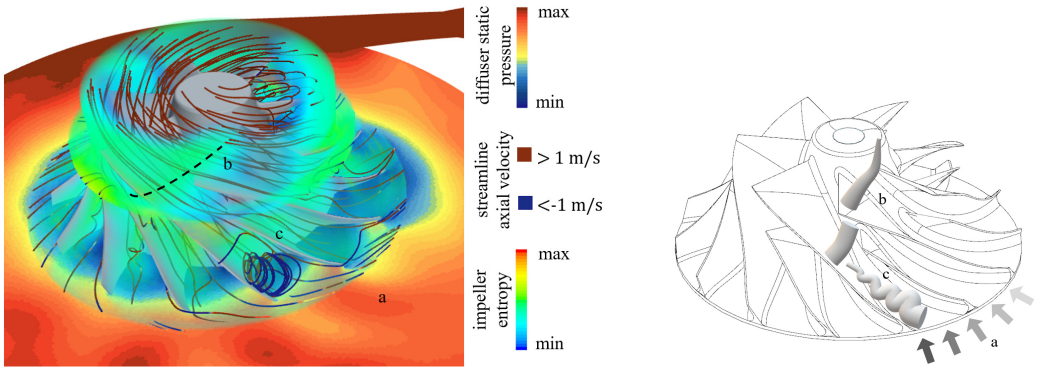


Figure 4.10.: Instantaneous mass flow rate at compressor outlet before, during, and after stall inception.

disturbed flow. The corresponding results are shown in Figure 4.11.



(a) CFD flow field during exducer stall inception

(b) sketch of dominant flow features

Figure 4.11.: exducer stall inception, time step d

To the left, the raw CFD results are presented, while the right side provides a schematic highlighting the dominant flow features. At position "a", a sharp increase in pressure resulting from the diffuser stall can be seen. Feature "b" denotes a region of significantly increased entropy reaching out of the impeller, but also connecting with the main blade's suction side just upstream of the exducer stall "c", as illustrated by the streamlines in the rotating frame.

To further investigate flow feature "b", axial velocity and entropy distributions at the compressor inlet, as well as entropy at 90% span, are extracted at time steps a, c, d and are shown in Figure 4.12.

The axial velocity plots (Fig.4.12, row one) clearly show that, even during the unstable time step "d", no impeller backflow occurs. Thus, it can be concluded that the flow structure originates from upstream the impeller.

The entropy contours at the impeller inlet (Fig.4.12, row two) show that under stable operating conditions, at first an approximately axisymmetric high-entropy ring forms near the shroud (time step a). As the mass flow decreases, this ring evolves into three distinct high-entropy regions (time step c) which subsequently move radially toward the impeller hub (time steps c-d). Notably, the circumferential position of these features remains nearly stationary, exhibiting a rotational speed of only 1.4% of the impeller speed.

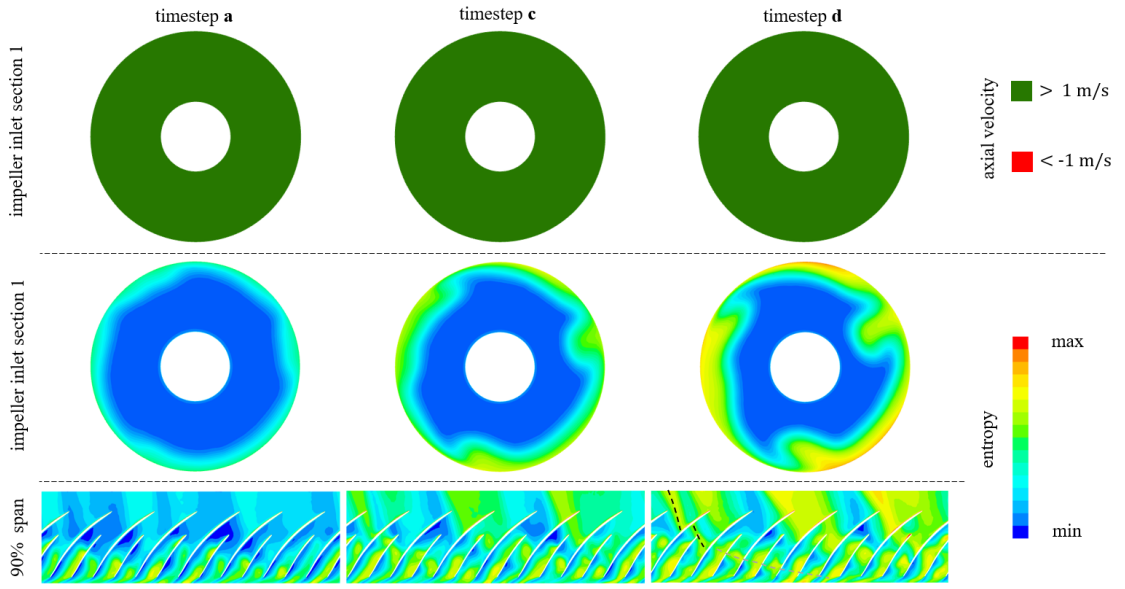


Figure 4.12.: Relevant flow fields for investigation of flow structure "b" at time steps a, c, and d.

This slow movement is attributed entirely to the decreasing mass flow rate, indicating that the features originate from fixed locations in the absolute (stationary) frame of reference.

The entropy distribution at 90% span (Fig.4.12, row three) reveals that these three flow features penetrate into the rotor domain but are interrupted and broken down by the main blades. This is best observed at time step d, where an incoming blade divides one of the features, and its remnants can be tracked as they are convected downstream through the rotor. This behavior is highlighted by the black and grey dashed lines for improved visualization.

Combining these findings with the fact that the ported shroud cavity has three support ribs, it is concluded that the high entropy regions correspond to a coherent flow structure characterized by the following:

1. It originates from the ported shroud, as it must form upstream of the impeller. Given that the compressor inlet is modeled with ideal inflow conditions in the CFD setup, the ported shroud is the only plausible source.

2. It results from the interaction between the recirculating flow and the support ribs, as the structure remains fixed in the absolute frame and appears at circumferentially equidistant positions, consistent with the rib spacing.

3. It is driven by the strength of the recirculation flow and therefore increases in both magnitude and radial penetration as the amount of recirculated flow grows.

Figure 4.13 presents a schematic of the origin and formation of flow feature "b", which are declared as vortex structures. As the flow enters the ported shroud, it exhibits a high circumferential velocity. While a part of this flow spirals upward towards the exit, a significant portion impinges on the support rib, redirecting it axially. The resulting jet

then interacts with the spiraling flow and is subsequently deflected nearly 180°deg by the noise ring, redirecting it toward the impeller inlet. As a result, the vortex structure forms in the inlet. Notably, similar vortex and jet structures have been experimentally confirmed using PIV in compressors with ported shrouds lacking a noise ring [67]. Furthermore, it is reported in [14] that the induced swirl lowers the impellers capability to rise pressure, a key factor in the onset of surge.

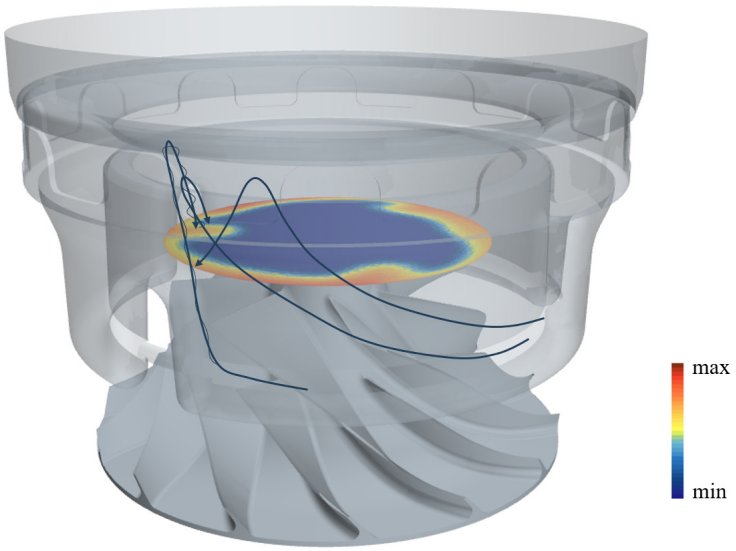


Figure 4.13.: Origin and formation of flow feature "b", symbolically shown for one rib. Entropy section above impeller overlaid with relevant streamlines.

With flow structure "b" identified as a vortex structure originating from the ported shroud, disturbing the inlet flow conditions, it is concluded that the exducer stall inception results from a combination of two mechanisms: the increasing backpressure caused by the downstream diffuser stall, and the growing inflow disturbance induced by the increasing recirculation through the ported shroud.

Once initiated, the exducer stall, diffuser stall, and ported shroud recirculation enter a self-reinforcing feedback loop. The stalled exducer exacerbates the diffuser stall, which in turn intensifies the stall in the following passages. Simultaneously, the stalled exducer increases the volume of recirculated flow through the ported shroud, further disturbing the impeller inflow and amplifying the severity of the exducer stall.

With the resulting drop in mass flow rate, the pressure difference at the volute tongue increases (Fig. 4.8 timesteps d-e), raising the backpressure experienced by the impeller passage at this location and promoting a stronger impeller stall in this area as well. Consequently, the spillage flow at the volute tongue intensifies, intitiating a clockwise rotation of the diffuser flow field (Fig. 4.7 time steps d-e).

It is interesting to see that the two jets in the diffuser (Fig. 4.8 timesteps d-e) rotate at different speeds. The jet at the three o‘clock position, driven primarily by the volute tongue spillage and lower static backpressure, rotates more slowly. In contrast, the jet

at the nine o'clock position, driven by the growing diffuser and exducer stall, rotates significantly faster.

The flow field collapses entirely as the faster-rotating jet reaches the volute tongue area (Fig. 4.8 timestep f), at which point backflow becomes observable at the compressor inlet.

During the flow reversal phase, the inlet flow field structure is consistent with the PIV measurements in [67, 70]. It is dominated by a single, large and fast-rotating backflow area near the shroud, while flow near the hub continues to enter the impeller. A substantial portion of the backflow exits through the ported shroud cavity, which is believed to significantly reduce the induced stress on the inducer during surge.

4.3.2. Conclusion

The surge trigger of the compressor is an exducer stall at the impeller's five o'clock position, initiated by a coupled mechanism of diffuser stall and inlet flow disturbance induced by the ported shroud. With the exducer stall formed, multiple self-reinforcing feedback loops arise, leading to a global breakdown of the flow field. Many of the reported effects have been documented in other works utilizing different approaches such as PIV or LES, thus supporting the findings presented here.

A comparison with the quasi-steady HGTR results confirms this chain of effects experimentally, as illustrated in Figure 4.14. The low point in the HGTR quasi-steady pressure curve is characteristic of diffuser stall, as also observed in the URANS. Furthermore, the occurrence of the exducer stall in the simulation aligns very closely with the HGTR's stability limit ($\triangle \dot{m}_{normalized} = 0.005$).

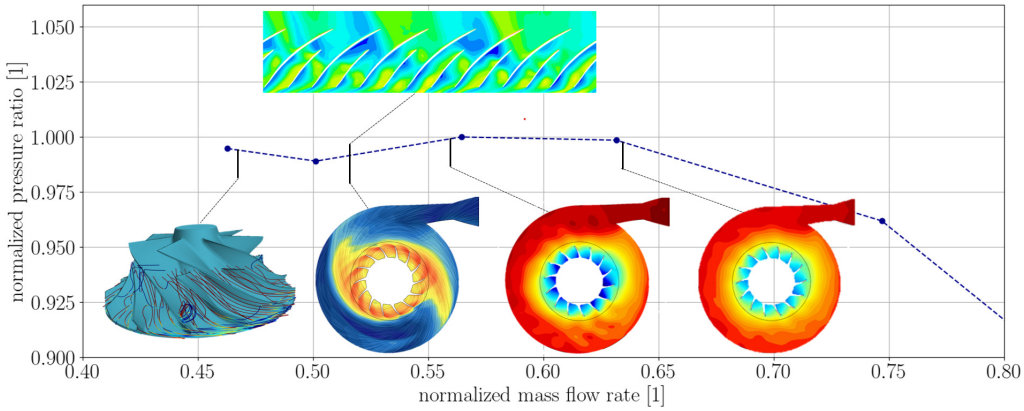


Figure 4.14.: Key events of the compressor entering surge. HGTR quasi-steady measurements and URANS flow fields.

Hence, it is confirmed that URANS simulations, with an emphasis on numerical stability and efficiency, can capture surge and its driving phenomena. However, the URANS reaches its limits for in-depth analysis of single effects, e.g. the understanding of the tip leakage flows role in exducer separation.

4.4. Compressor Improvement Recommendations

With the surge trigger mechanism understood, possibilities for optimization can be investigated. Given that compressor B was originally developed using an automated optimization framework, it would be counterproductive to alter the parameters that were explicitly varied during the design process, as these have been tuned to achieve a local optimum on the Pareto front generated by the optimizer.

Instead, the current findings are used to identify design parameters or features that were not included in the original optimization scope but exhibit potential for improving either efficiency or map width.

4.4.1. Ported Shroud

The ported shroud of the compressor has been found that while extending the stable operating range of the compressor, at some point, the recirculating flow becomes one of the two disturbances reliable for initiating surge. Thus, reducing this disturbance directly addresses a fundamental trigger of surge onset.

In the current configuration, optimization strategies targeting the ported shroud inlet, such as recommended in [73], are not considered viable as the ported shroud can effectively remove the low momentum flow from the shroud contour. Therefore, modifications to the ported shroud inlet positioning, width, and angle, will not contribute much to delay surge, but are likely to deteriorate efficiency.

However, it was found that the ported shroud support ribs generate a surge-relevant inlet flow disturbance, which has been widely acknowledged in literature, compare Chapter 2. Importantly, studies did not only report this disturbance, but also propose mitigation strategies. For instance, [71], introduces the concept of utilizing the ribs as flow-directing vanes, with experimental validation supporting its effectiveness. While such geometric modifications entail considerable implications for manufacturing, vibrations, mechanical and thermal stress, and containment requirements, they offer the potential for substantial surge mitigation without adversely affecting efficiency. Given that a proof of concept exists in literature, no further investigation is pursued. Additional contributions would require a comprehensive optimization that accounts for all aforementioned constraints, which is beyond the scope of the present work.

4.4.2. Impeller Optimization

One potential mitigation strategy for exducer stall is to increase the impeller's resistance by employing more backward-swept exducer blades. However, the *outlet blade angle* was already an optimization parameter in the original design. Altering it would directly influence the impeller exit flow and compromise aerodynamic matching with downstream

components. Consequently, improvements targeting surge behavior via impeller modifications are likely to incur substantial efficiency losses and are thus not considered a feasible strategy.

Instead, recognizing that the stall-triggering disturbances originate both upstream and downstream of the impeller, other surge-delaying features such as the splitter blades can be optimized. The splitter blades were initially positioned at this location as it was thought that the impeller might stall due to its expanding section, that is, due to high relative fluid velocity deceleration. However, the splitter blade cannot mitigate the incoming disturbance nor the sudden increase in backpressure. Thus, moderate axial repositioning of the splitter blades is not expected to influence surge behaviour but offers potential for optimization.

For this impeller, the critical cross-section is defined by the leading edge position of the splitter blades. Shifting the leading edge downstream increases choke mass flow, whereas shifting it upstream reduces it. At the design condition, these changes are expected to be efficiency-neutral. However, a slight efficiency benefit is anticipated near surge for upstream-shifted blades due to improved flow guidance and reduced losses. Conversely, downstream-shifted blades should perform better at high mass flows due to decreased fluid velocity and hence, reduced friction losses.

To validate this hypothesis, two RANS speedline simulations were conducted at 86% rotational speed and the maximum choke point, with splitter blades shifted 10% upstream and downstream. Figure 4.15 illustrates the geometries, and Table 4.2 summarizes the results. The pressure ratio remains unchanged compared to the baseline, and the choke mass flow rate varies as predicted. Also, the efficiency trend aligns well with the theory.

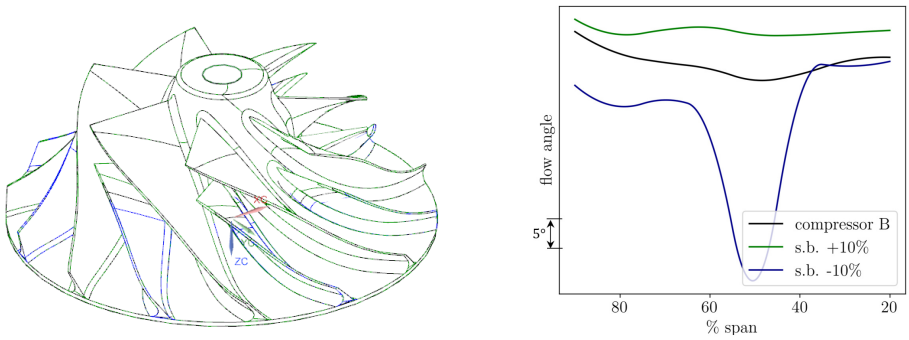
	0.58		0.61		0.65		0.7		max choke
	Π_{TT}	η_{is}	Π_{TT}	η_{is}	Π_{TT}	η_{is}	Π_{TT}	η_{is}	$\dot{m}$
downstream shifted s.b.	-0.001	-0.26	-0.001	-0.16	0	-0.06	0.002	-0.02	+1
upstream shifted s.b.	0.001	0.13	0	0.02	-0.002	-0.11	-0.003	-0.19	-1.9

Table 4.2.: RANS results of impeller splitter blade optimization at given mass flow rates. Normalized difference to compressor B (%).

To assess potential splitter blade stall due to missmatch between the flow field and leading edge angle, the flow angle β was extracted from the simulations. Figure 4.15b presents the incidence angle at a normalized mass flow rate of 0.65, where the flow field can be considered quasi-steady (compare Fig. 4.14). The same trend is observed at lower mass flow rates.

The plot reveals a pronounced disturbance at 50% span for the downstream-shifted splitter blade, likely caused by a vortex generated by tip leakage flow from the main blade, as described in [13]. The downstream shift positions the splitter blade's leading edge within this vortex region, likely forcing an immediate separation at the splitter blade

suction side.



(a) impeller geometries

(b) flow incidence angle at s.b. leading edge

Figure 4.15.: Impeller geometries and flow incidence angle β at splitter blade leading edge at normalized mass flow rate 0.58. All angles are positive, compare Fig. 2.3

This finding is particularly interesting as it raises the question of whether the geometric modifications can still be considered moderate, and as a resulting question, if the surge trigger mechanism itself is rather limit-stable and other effects might rapidly overpower the effect chain, or if the surge trigger mechanism is dominant against other possible separations.

To investigate this, experiments were conducted to obtain reliable results. Three impellers were manufactured and consecutively tested using the same compressor housing: one with splitter blades shifted 10% upstream, one with blades shifted 10% downstream, and a baseline configuration. The measurements confirm the following:

- The surge line remains unchanged across the compressor map for all configurations, within measurement accuracy of the HGTR.
- Choke mass flow increases with downstream shifted splitter blades and decreases with upstream shifted splitter blades.
- For the downstream-shifted configuration, efficiency improves significantly (up to 3%) at high mass flows but slightly deteriorates near surge, consistent with RANS predictions.
- For the upstream-shifted configuration, efficiency slightly improves near surge but deteriorates at high mass flows, also in agreement with RANS.

From these results, two key conclusions can be drawn.

First, the experiments reveal a notable insensitivity of the surge line to geometric changes of an impeller feature previously considered critical for surge delay. This provides experimental evidence that surge initiation is not governed by splitter blade stall or impeller-induced relative velocity deceleration. Furthermore, it shows that the surge trigger mechanism dominates over other forms of flow separation and remains robust

under moderate geometric or environmental disturbances.

Second, the axial positioning of the splitter blade is identified as a viable optimization parameter, with potential to enhance choke mass flow rate or increase efficiency in engine-relevant areas. Given that RANS successfully replicate the experimental trends, a more detailed numerical optimization study is both feasible and warranted.

4.4.3. Diffuser Optimization

Both *diffuser width* and *diffuser outlet radius* were included in the automatic optimization process and thus should not be varied. Although various techniques exist to enhance diffuser stability -such as the implementation of grooves [111] or active fluid injection [12]- these methods are generally not employed in series production due to either significant efficiency penalties or increased system complexity. Thus, no further diffuser optimization is pursued.

4.4.4. Volute Optimization

One of the compressors surge-driving effects is the non-axissymmetric pressure distortion of the volute. Thus, mitigating or delaying this effect will adress one of the root causes of surge. Additionally, the (resulting) delay of diffuser stall will generally lead to better performance of the compressor at low mass flow rates.

The volute is designed using the traditional linear A/R approach, which is based on conserving angular momentum at design flow rate [44]. At the design point, the volute functions as a flow collector. However, at low mass flow rates, the volute cross sectional area increases faster than flow enters the volute, leading to flow deceleration and increased losses as the volute becomes a diffuser. Conversely, for mass flows above the design point, more flow enters the volute than the cross sectional area increases, leading to an acceleration and increase in losses as the volute acts as a nozzle. Hence, the volute exhibits a parabolic loss profile, with high losses at low and high mass flow rates and a minimum at design point.

The A/R was included in the original optimization approach and hence, the volute is well matched for the considered compressor design. Thus, a change in the A/R leads to a drop in design point efficiency, which would result in the typical improvement of surge on cost of efficiency.

However, the increasing static pressure difference at the volute tongue, combined with the overhang volute design, can be exploited to create a self-regulating recirculation channel that counteracts the increasing pressure distortion and diffusion losses.

Considering the static pressure field in Figure 4.8, the most significant pressure gradient is found at the volute tongue, which drives a portion of the flow to re-enter the volute rather than exiting through the outlet. This recirculation is undesirable, as it increases mixing losses and the volute tongue is generally recognized as a critical factor influencing surge.

However, due to manufacturing constraints, an overhang volute inherently includes a channel-like opening beneath the diffuser exit, opposite the volute tongue (that is, the shroud side). Flow trough this passage can be recirculated, effectively simulating a higher mass flow rate. Although some mixing losses likely increase locally, they should be outweighed by the reduction in uncontrolled expansion and mixing losses within the volute, leading to improved global efficiency and pressure ratio. Additionally, the reduced pressure distortion should lead to a delayed diffuser stall, enhancing surge margin.

To investigate this concept, a modified volute design incorporating a curvature-constant overhang recirculation channel was developed and evaluated using RANS simulations at 86% rotational speed. Figure 4.16 illustrates the changes in pressure ratio and efficiency relative to the baseline configuration.

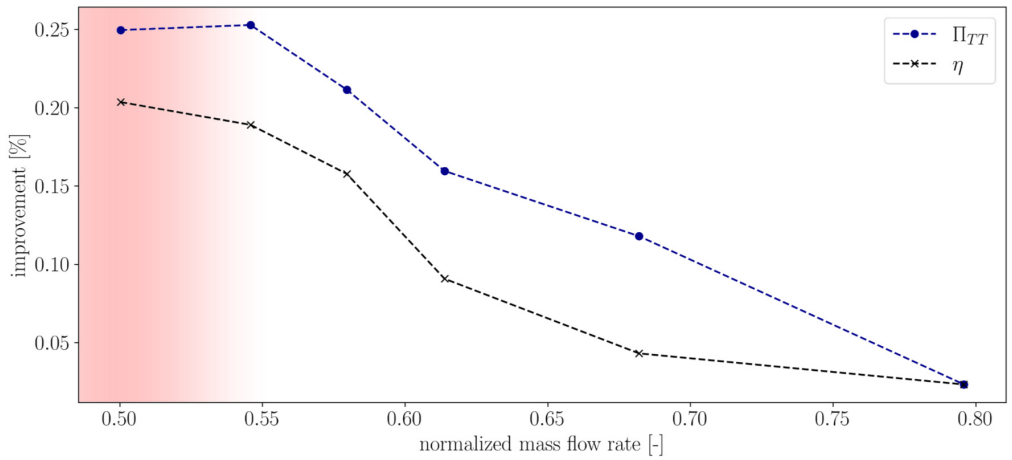
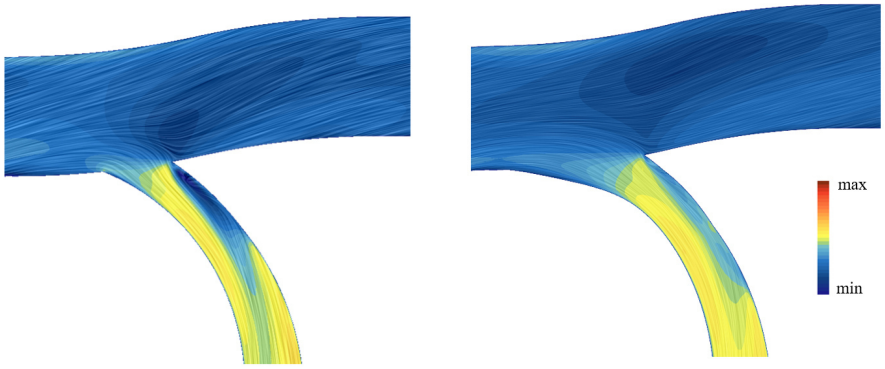


Figure 4.16.: Percentual improvement of the overhang volute compared to the baseline configuration. At the lowest mass flow rate, minor flow oscillations were observed (1.8gps), indicating the onset of numerical instability in the RANS.

As hypothesized, pressure ratio and efficiency do not change at high mass flow rates. However, towards surge, both pressure ratio and efficiency improve compared to the baseline. At the lowest mass flow rate, minor mass flow oscillations were observed, indicating the onset of numerical instability. This region is marked in the figure as red to highlight the area of increased uncertainty.

Figure 4.17 shows the velocity line integral convolution plot at 55% normalized mass flow rate at the volute tongue, where the optimization was conducted.

In the standard overhang volute design, a stall cell forms behind the volute tongue due



(a) standard overhang volute design

(b) curvature constant overhang volute recirculation channel

Figure 4.17.: Volute recirculation channel and standard volute design. Velocity magnitude, line integral convolution plot.

to a sudden increase in cross-sectional area, creating a large separation zone. This stall cell extends far downstream, significantly disrupting the volute flow field and increasing losses. The blockage at the volute tongue also intensifies the circumferential pressure gradient by restricting mass flow into the volute.

In contrast, the curvature-constant overhang volute recirculation channel design effectively suppresses the stall cell. Flow enters the channel smoothly, resulting in a more uniform flow field and higher mass flow rate throughout the volute. The better functioning of the volute is evident even at the outlet, where the flow is more homogeneous due to enhanced inflow conditions into the reciculation channel. Consequently, losses are reduced, and the volute operates closer to its design condition, yielding increased pressure ratio and efficiency compared to the baseline.

With this, optimization potential for improving efficiency and pressure ratio at low mass flow rates is identified. Importantly, this enhancement does not compromise performance at choke conditions, as the recirculation channel is self-regulating. RANS simulations confirm no adverse impact on choke. Moreover, the results suggest that surge can be optimized as well as one of the two key disturbances is directly addressed. However, the RANS simulation results only provide indicative results; definitive validation requires URANS simulations, or HGTR measurements.

4.5. Addendum: Investigation of Automated Surge Trigger Detection

Although the surge trigger was successfully identified through manual analysis, the process proved to be time-consuming and heavily dependent on expert judgment. This reliance makes manual analysis impractical for industrial applications, where automation and scalability are critical. With the full chain of events leading to surge understood and validated, three automated surge trigger methods are investigated for possible suitability. The backflow and entropy-based methods are selected due to their frequent recommen-

dation in grey literature, while a transient stability parameter (SP) method is investigated owing to the demonstrated effectiveness of SP-based approaches in quasi-steady analyses.

4.5.1. Backflow Method

The backflow method is based on the assumption that a key characteristic of a flow separation is the occurrence of backflow (which is actually correct [34]).

However, this method is inherently ineffective when a ported shroud is used, which is designed to remove and recirculate backflow. Hence, the surge trigger is identified near the ported shroud opening at the onset of its intended operation. Furthermore, even in non-ported-shroud compressors, the initiation of reversed flow does not necessarily indicate the onset of surge [34].

4.5.2. Entropy-based Methods

Entropy-based methods aim to detect flow instabilities by analyzing entropy distributions across control surfaces or volumes. They typically rely on identifying high points or crossovers as indicators of flow separation. However, high entropy levels are not a unique feature of separation, but also found in stall-unrelated phenomena such as mixing or friction losses. Additionally, the dependency on the velocity field further compromises the results.

To illustrate these limitations, a series of entropy-monitoring control surfaces are introduced throughout the compressor. The mean entropy values at these locations are tracked and are presented in Figure 4.18. The control surfaces include the geometric compressor inlet "s _ inlet", six sections through the impeller, the impeller outlet, six diffuser sections, and the geometric compressor outlet.

The first entropy-based surge trigger occurs at a mass flow rate of 0.71, corresponding to a crossover between impeller sections three and four. However, this lies well within the stable operating regime and is attributed to an increase in losses caused by the tip of the splitter blade rotating between these sections.

The second trigger is observed at a mass flow rate of 0.66, based on a crossover between the diffuser outlet and diffuser section five. Although this marks the onset of minor flow separation in the diffuser, it remains within the stable regime.

A third trigger is identified at a mass flow rate of 0.505, involving a crossover between the compressor outlet and diffuser outlet. While this is close to the actual instability onset, the compressor is still stable. Moreover, the crossover occurs in a geometrically irrelevant region, as the critical flow breakdown is located in the exducer rather than the volute.

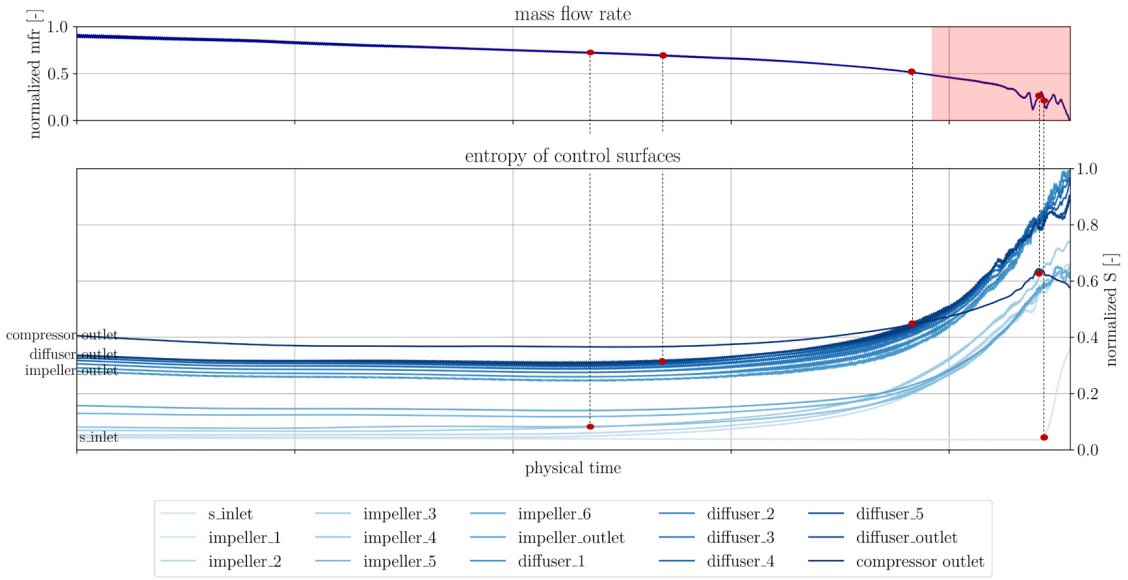


Figure 4.18.: Entropy based surge detection. Typical "surge triggers" based on crossovers and high points are marked in red. The red zone in the mass flow rate plot marks the actual instability zone.

The fourth and fifth surge triggers occur deep within the unstable regime and are based on a local entropy maximum at the compressor outlet, and increasing entropy levels at compressor inlet. These are interpreted as indicators of flow reversal. However, the reversal observed is a consequence of the flow breakdown in the impeller, which happened at a significantly higher mass flow.

It can therefore be concluded that entropy-based methods are not suitable for detecting the onset or location of surge. The methods are prone to false positives due to their sensitivity to non-critical entropy generating mechanisms. Definite indicators such as local or global high points are effectively equivalent to backflow detection methods and thus only capture the effects of surge after the flow has already broken down. As a result, they provide a significantly delayed indication of instability. Thus, entropy methods either generate too conservative, or optimistic, results and hence offer no predictive value.

4.5.3. Stability Parameter Method

The stability parameter (SP) [22], defined in eqn. 4.2, is a well-established criterion for detecting surge onset in compressors. It has recently been employed in [109] to investigate surge onset in a URANS simulation. The SP is derived from the quasi-steady compressor characteristic and indicates the onset of instability when its sign becomes positive.

In the study in [109], the URANS BC was incrementally adjusted after sufficiently long time intervals, allowing the extraction of time-averaged operating points for SP evaluation. This raises the question whether the SP can be applied to the presented setup that can only provide transient data.

$$SP = \frac{1}{\Pi_{SS}} \cdot \frac{d(\Pi_{SS})}{d\dot{m}} \tag{4.2}$$

Figure 4.19, shows such application, where the SP is evaluated across different control volumes (inducer, exducer, diffuser, volute) in the URANS simulation. At first glance, and in comparison with Figure 4.14, the results appear promising: all spikes occur at mass flow rates corresponding to diffuser and exducer stall, and the final spike even matches deep surge at the HGTR within less than 1% deviation in mass flow rate. Moreover, the location of the spikes suggest a similar origin of the stall as the manual flow field analysis.

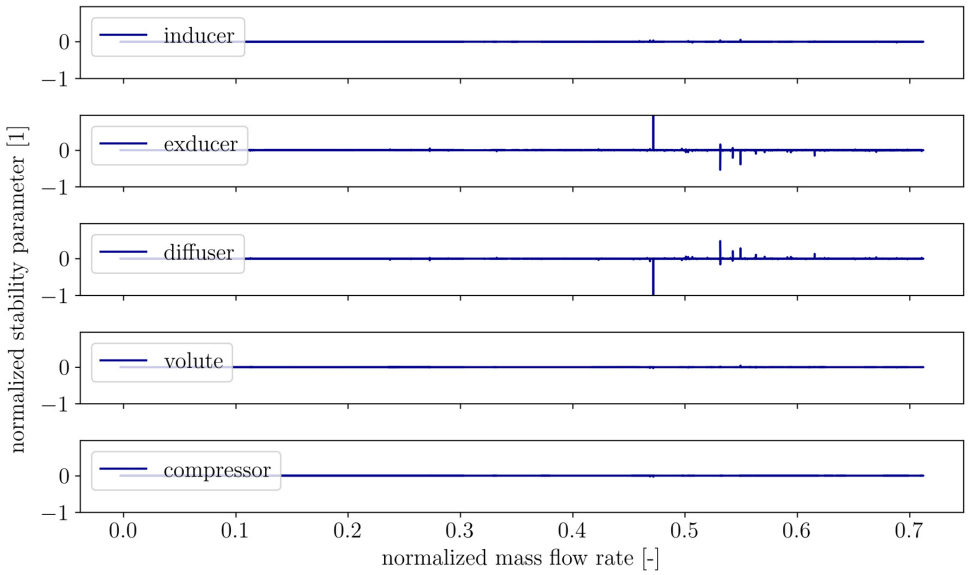


Figure 4.19.: Stability parameter applied on URANS data. Data normalized with stability parameter maximum. The y-axis scale is constant for all subplots.

However, this interpretation is misleading for several reasons:

1. Although a sufficiently small time step results in a quasi-steady geometric configuration (i.e., minimal impeller movement between steps), the flow field remains inherently transient. This violates a key assumption underlying the SP, which presumes quasi-steady flow behavior.

2. The observed spikes are not necessarily indicators of flow instability but rather artifacts of the numerical scheme. In a quasi-steady compressor map, the instantaneous operating point traces a loop around its time-averaged value [1]. This behavior persists even in transient compressor operation, with the loop shape adapting accordingly. Numerically, this loop results in divergence at both ends. A stall event can now increase the divergence-critical areas (as pressure is instantaneous but not

mass flow rate, hence, the steep part of the loop will increase), making it more likely that the discrete numerical scheme captures this vertical tangent.

Thus, the SP method is not a viable tool to detect surge onset in transient setups.

4.5.4. Conclusion

Three different approaches for automated surge detection in URANS simulations were investigated and it was found that none of them are suitable for reliable application.

Although frequently proposed in grey literature, backflow- and entropy-based methods oversimplify the mechanisms responsible for surge initiation. As a result, they produce inaccurate or misleading results.

The SP method, while a well-established tool for evaluating surge onset under quasi-steady conditions, was shown to be unsuitable for transient data as its core assumption is violated. Despite an apparent match between SP spikes and surge or stall onset, this correlation is coincidental. It arises from the increased likelihood of the numerical scheme detecting divergence in the slope of the instantaneous compressor loop, which occurs even under stable conditions.

In all three cases, the methods were motivated by some physical reasoning and, in some instances, yielded results that appeared to match surge behaviour. However, these matches are either not generalizable across different compressors, or, as in the case of the SP method, are coincidental and mask fundamental flaws in the underlaying assumptions.

4.6. Summary

A robust URANS setup was presented that focuses on numerical cost and stability. Extensive validation against test rig data demonstrated good agreement, confirming the setup's capability to capture surge-relevant flow phenomena. Through detailed flow field analysis, the surge trigger mechanism was identified as a combination of diffuser stall and inlet flow distortion caused by recirculation through the ported shroud, ultimately leading to flow separation in the exducer. Although transient measurements were not feasible at the HGTR, steady-state data confirmed diffuser stall and the onset of global instability, further validating the simulation and analysis.

Based on the understanding of the surge inception mechanism, optimization potential was identified. The ported shroud ribs were found to significantly disturb the inlet flow field. As design improvements for this component are already available in literature [71], no further investigation was conducted.

For the impeller, the splitter blade position was found to be a new optimization parameter. The splitter blades can be moved up- or downstream to shift efficiency areas and choke mass flow. Furthermore, it was experimentally proven that the splitter blade positioning does not change the surge point. Hence, numerical optimization can be conducted that allows for better efficiency and choke mass flow rate without compromising surge.

While no optimization potential was found for the diffuser, the volute showed room for improvement. A self-adjusting overhang volute recirculation channel was designed, which increased efficiency and pressure ratio at low mass flow rates while remaining neutral under high mass flow and choke conditions.

Finally, various automated surge trigger detection methods were applied to the URANS results and compared with manual analysis. None of the methods successfully detected the surge trigger or its onset, underscoring the complexity of surge phenomena. Although there is a strong demand to automate the analysis of the large datasets generated by URANS, the application of such methods -at least in their current form- proved counterproductive and leads to misleading results.

In conclusion, industrial simulation setups that focus on numerical cost and stability are capable of capturing surge-relevant flow phenomena and can be effectively used to investigate surge mechanisms. This represents a significant step toward the broader adoption of URANS in compressor development, enabling better compressor designs. The improvement recommendations derived from the URANS identified optimization opportunities that would have been overlooked using RANS or conventional engineering experience alone.

5. Compressor Operation in Transient Environments

So far, it has been assumed that the compressor operates in a steady environment. This assumption is valid for the electric rig and HGTR under normal operating conditions, but does not represent the actual environment the compressor will operate in. Instead, the operation of a piston engine (or more general, any displacement machinery) downstream of the compressor introduces pulses that interact with the compressor, affecting pressure ratio, efficiency and surge limit [1, 53, 59, 60, 61, 58, 54, 57, 62, 112, 24].

For surge, contradictory trends have been reported. Experimental work conducted by Barrera-Medrano [1, 53], Shu et al. [59], Marelli et al. [112], and Galindo et al. [57] show an improvement in surge margin. Brun et al. [58] and Buehler [54] reports otherwise, and it seems to be a general trend in industry to assume surge deterioration. On the other hand, Werner [24] notes that both improvement or deterioration can be observed on an ETR.

It becomes clear that so far, no generally applicable theory has been found. This chapter is thus intended to help in the understanding of compressors operating in transient environments and provide insights into engine-like environments, a topic often hidden to public research.

In the first section, the hardware used in the experiments is introduced. Then, measurements with a pulsating flow device on a HGTR are performed and the results analyzed. Next, engine measurements are conducted and the effects of EGR and surge testing procedures are explained. Last, the findings are summarized and further research outlined.

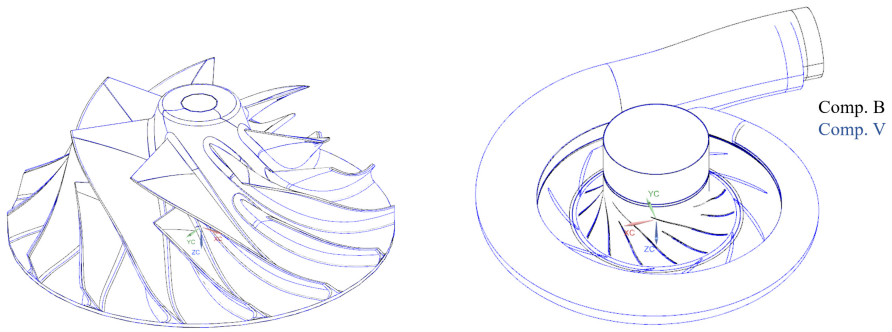
5.1. Compressor Geometries

The experimental work presented in this chapter is conducted with compressor B for vaneless diffuser designs, and compressor V for vaned diffuser designs. Compressor V is, similarly to compressor B, designed for 12.8-15.6l six cylinder engines, but optimized towards other engine operating points. Figure 5.1 shows the fluid volumes and impellers of the compressors.

Large data set testing is conducted with a proprietary compressor set, with the compressors belonging to the compressor B and V family.

5.2. Measurements with the Pulsating Flow Device

A PFD similarly to the one used in the work by Barrera-Medrano [1] is installed at the HGTR. The pulser is located between measurement ducting and variable plenum. The plenum itself is connected to the throttle valve. At each inlet and outlet of the compressor, three Kistler 407A V200S pressure transducers are installed to allow transient pressure



(a) impellers B and V (b) fluid volume compressor B and V

Figure 5.1.: comparison of compressors B and V

measurements. Figure 5.2 shows the overall test bench setup.

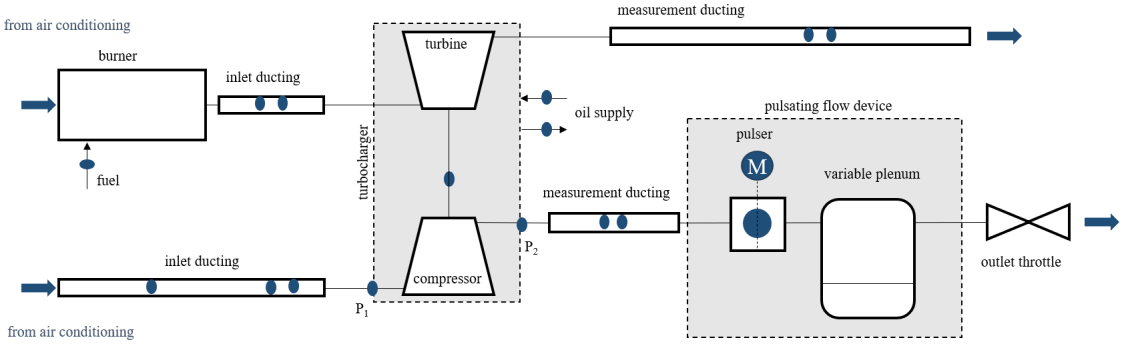


Figure 5.2.: HGTR with PFD

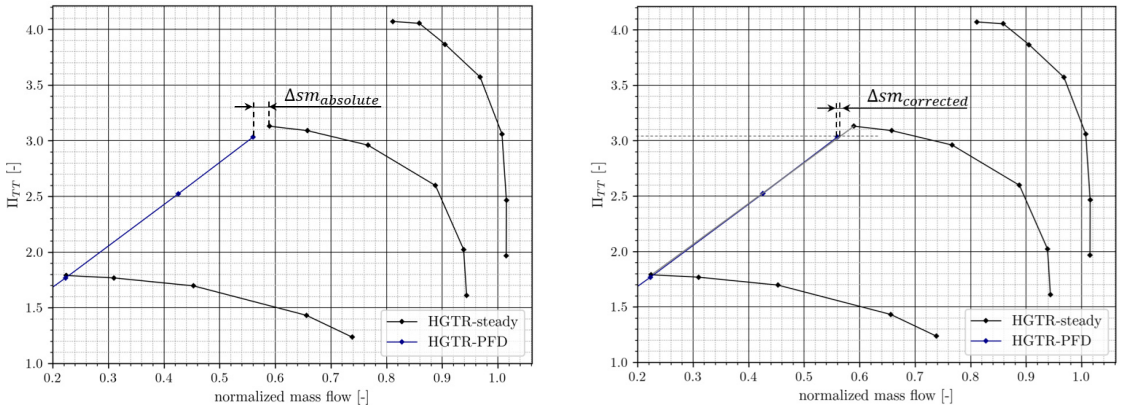
The PFD generates pressure pulses, analogous to those observed in Diesel engines, with characteristic frequencies on the order of 10^1 Hz, whereas the compressor impeller rotates at frequencies on the order of 10^3 Hz. The blade-passing frequency is even higher, reaching the order of 10^4 Hz. Hence, the pulsation frequency introduced by the PFD is significantly lower than the dominant aerodynamic frequencies of the compressor.

When a compressor operates under pulsating conditions, it does not converge towards a quasi-steady single point in a compressor map, but forms a hysteresis loop. The loop's shape is dependent on pulsation amplitude, frequency and plenum volume. Moreover, the hysteresis loop does not have a constant angular velocity, but changes speed depending on its position. Therefore, the instantaneous operating point can be significantly different from its quasi-steady counterpart. [1]

Measuring the instantaneous operating point is limited by the mass flow meters positioning and accuracy under changing fluid properties. It is therefore not possible to determine the hysteresis loop in industrial HGTR environments. Even if so, it would be difficult to compare a hysteresis loop with a time-averaged data point in a steady environment. Therefore, all pulsating condition measurements are time-averaged using the same averaging technique applied to quasi-steady measurements, leading to an artificial operating point that can be compared to its quasi-steady counterpart.

5.2.1. Surge Margin Shift Definitions

As already shown by different research [53, 60], a compressors time-averaged capability to increase pressure deteriorates under pulsating backpressure. This finding is generally valid and not bounded to a specific compressor design or test bench, as long as the circumferential speed is not altered.[12] The strength of this effect, is, however, dependent on the compressor and can lead to false conclusions, as depicted in Figure 5.3.



(a) absolute sm shift

(b) corrected sm shift

Figure 5.3.: definition of absolute and corrected surge margin shift

In the figure, a compressor is tested under pulsating (blue) and non-pulsating (black) conditions. The pulsations force the compressor to operate at lower pressure ratios at the same rotational speed. A direct comparison of the surge mass flow rates leads to the conclusion that the compressor improves its surge margin under pulsating conditions, as depicted in case a: absolute surge margin shift.

It is obvious that at least some of the improvement is due to the compressor operating at lower pressure ratios. A correction scheme based on a linear interpolation of the quasi-steady compressor characteristic, eqn. 5.1 takes this shift into account and is visually depicted in Figure 5.3 b. In this case, the surge margin shift is solely due to the decrease in pressure ratio.

$$\triangle sm = \frac{(\Pi_{PFD} - \Pi_{qs1})(\dot{m}_{qs1} - \dot{m}_{qs2})}{\Pi_{qs1} - \Pi_{qs2}} + \dot{m}_{qs1} - \dot{m}_{PFD} \tag{5.1}$$

With the new surge margin shift definition, the true influence of pulses on the surge margin can be determined. It is therefore an important parameter to evaluate the actual performance and suitability of a compressor to operate in an unsteady environment.
As previous papers do not apply the scheme, both values (absolute and corrected surge margin shift) are given to allow comparison.

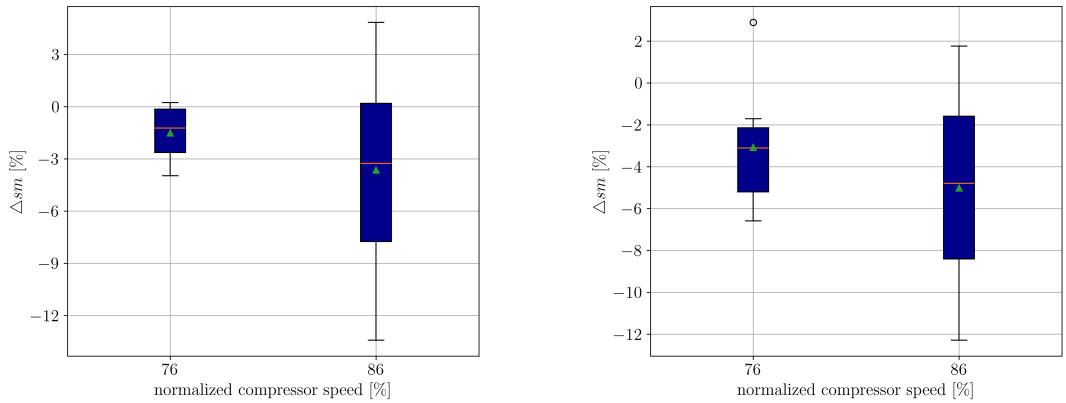
[12] ETRs do not fulfill this condition and are treated in a separate section.

5.2.2. Influence of a Ported Shroud

In traditional compressor design approaches, a ported shroud is considered an option to enhance surge or choke margin. However, it is not typically included in the initial design phase but is often added in later stages. This raises the question of whether a compressor behaves differently under pulsating conditions when a ported shroud is used. The outcome determines the earliest design stage at which pulsating environments can be considered, thereby significantly influencing the overall development strategy.

To address this question, a specific pulsating condition was selected, and a set of proprietary compressor designs, both with and without ported shrouds, were tested. The results for the 77% and 86% speedlines for compressors with ported shrouds are presented in Figure 5.4. In these graphs, the difference between the pulsating condition and its steady counterpart $\triangle sm$ has been normalized with the maximum choke mass flow. Positive values indicate an improvement in surge margin under pulsating conditions, while negative values indicate a deterioration.

From Figure 5.4, it is evident that for the applied pulsating condition, the surge margin predominantly deteriorates. The median and mean values are closely aligned, suggesting a normal distribution. On average, the corrected surge margin deteriorates by -3% for the 76% compressor speed and by -4.8% for the 86% compressor speed. An outlier exists for the 76% speedline, which can be attributed to a heavily kinked surge line that the correction scheme cannot accurately follow.



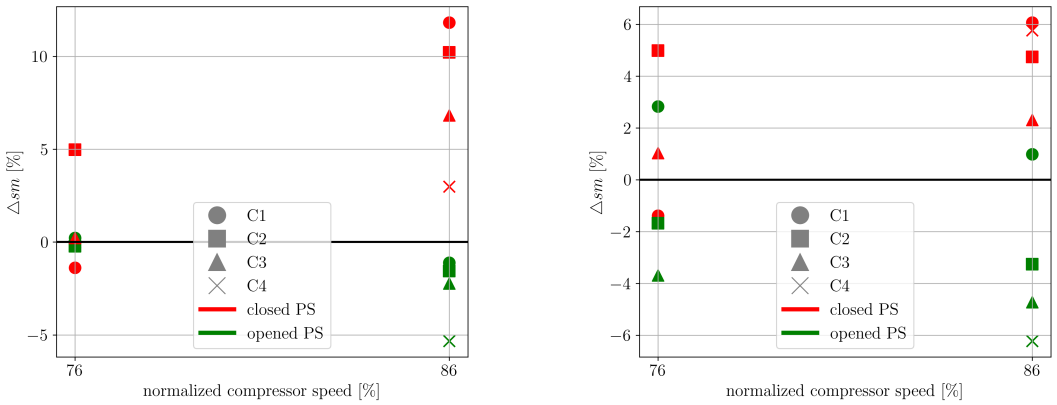
(a) absolute sm shift

(b) corrected sm shift

Figure 5.4.: absolute and corrected surge margin shift of compressors with ported shroud

With a statistically significant data set obtained for open ported shroud compressors, the hypothesis that "ported shroud compressors behave similarly to non-ported shroud compressors" can be falsified if even one compressor in the sample set does not follow this trend. Consequently, testing can be significantly reduced. Figure 5.5 shows four different compressors that meet this falsification criterion, highlighting that the surge

margin impact either reverses or changes drastically.



(a) absolute sm shift

(b) corrected sm shift

Figure 5.5.: absolute and corrected surge margin shift of compressors with and without ported shroud

It is therefore concluded that pulsating conditions must be considered at very late design phases, as results cannot be transferred between ported and non-ported shroud designs.

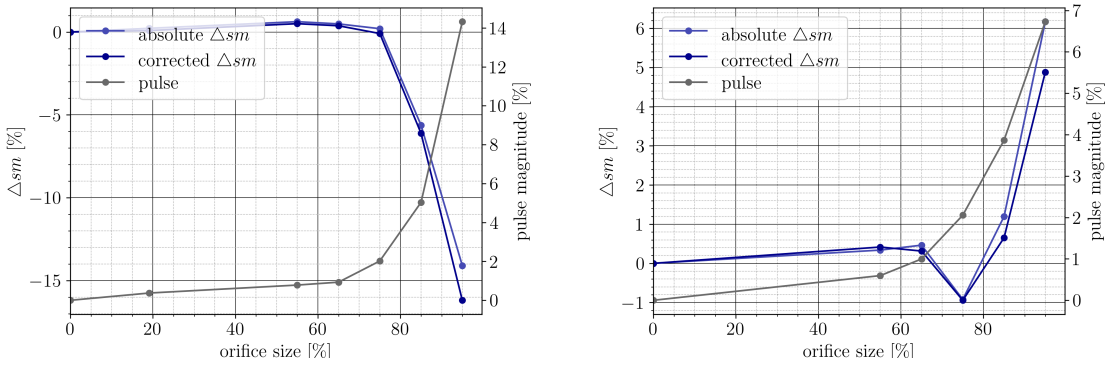
Moreover, the experimental results are particularly significant because much of the research reporting an improvement in surge margin has been conducted using turbocharger compressors without ported shrouds [53, 1, 59, 61, 62, 113, 109]. No information is available for [57, 112], where a surge margin improvement is also reported. This suggests that the opposing trends observed in industry might be related to the inclusion of a ported shroud. Ported shrouds have become a standard feature, and thus, industrial transient surge testing is generally not performed without ported shroud compressors.

A potential explanation for the observed behavioral differences may be attributed to the surge trigger mechanism. Non-ported shroud geometries typically experience stall within the impeller, whereas ported shroud geometries tend to initiate stall within the diffuser. Pulses have been shown to delay impeller stall, as demonstrated in [62, 113], yet it is hypothesized that they trigger diffuser stall by facilitating bypass transition. This hypothesis is supported by the correlation between diffuser stall lines and pulsation surge lines, although this relationship has not been thoroughly investigated. Future research is recommended to further understand this phenomenon.

5.2.3. Influence of Orifice Size on Vaned and Vaneless Diffuser Type Compressors

So far, only one specific design point has been tested. Hence, a variation in orifice size was conducted for compressors B and V.[13] The results are depicted in Figure 5.6.

[13]Pulser frequency differs from previous tests but remains constant. Compressors equipped with ported shroud.



(a) vaned diffuser design, compressor V

(b) vaneless diffuser design, compressor B (interpolated)

Figure 5.6.: influence of pulsation amplitude on surge margin shift

In the plots, the pulse magnitude is normalized with its time average. It is evident that although the orifice size influences the pulse amplitude, the amplitude results from various factors, including mass flow rate and compressor response. Thus, statistical independence of parameters is only given for the orifice size, mass flow rate, and pulse frequency.

Up to orifice sizes of 75%, the observed trends are similar for vaned and vaneless diffuser designs. A slight surge margin improvement is noted, peaking at the 55% orifice size. The 75% orifice marks a pronounced drop, and the compressors' surge margin begin to deteriorate. From this point, however, very different trends emerge. For the vaned diffuser design, the surge margin deteriorates significantly, reaching up to -16% for the largest orifice size (corrected $\triangle sm$). Conversely, the vaneless design improves its surge margin after the initial drop, achieving an improvement of 4.9% corrected $\triangle sm$.

The deterioration of compressor V under stronger pulsation can be explained by the stall mechanism of vaned-type compressors. Once one component -rotor or stator- stalls, it triggers the stall in the other component. As a result, vaned diffuser type compressors enter deep surge relatively quickly and do not exhibit pronounced stalled regimes. Hence, once a critical pulsation level is reached, deep surge is almost immediately triggered. Once deep surge is triggered, it cannot be delayed by any pulser-induced phenomena due to the different magnitudes of energy of the occurring waves.

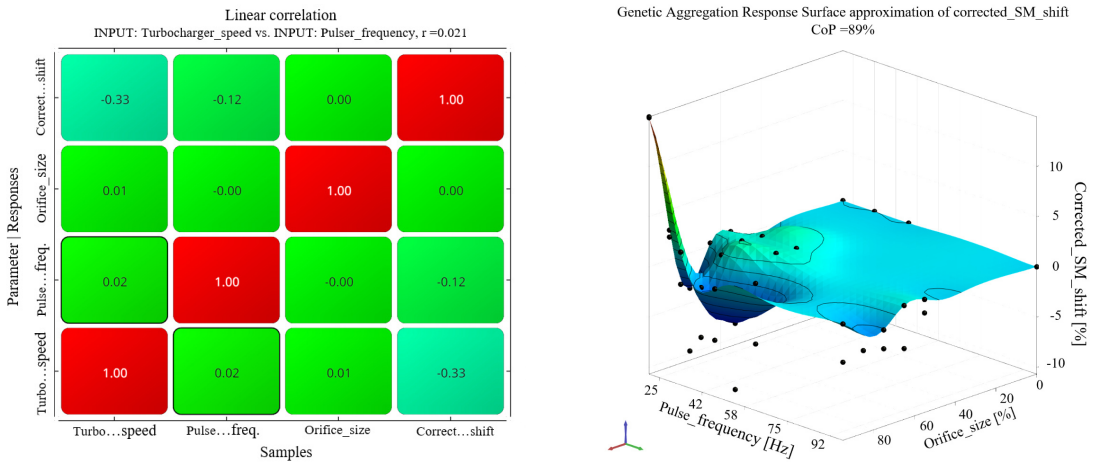
In contrast, vaneless diffuser designs can exhibit "stable" rotating stall areas, and their transition to deep surge is generally slower. This allows the imprinted pulse to interact and counteract surge development or to force the compressor into a mild surge. With the definition of the surge margin as the occurrence of deep surge cycles, this leads to an improvement in surge margin.

As a result of this investigation, it can be stated that vaned and vaneless diffuser type compressors can behave very differently when subjected to pulsating conditions. These

findings are significant when compared to the literature. To the author's knowledge, there is currently no literature available investigating the effect of pressure pulses on vaned-type diffusers. It is likely that they have been investigated in more stationary setups, such as pipeline systems [58], but this has not been explicitly stated. Thus, it is likely that, similar to the ported shroud, seemingly contradictory results are due to significantly different design features of compressors that cannot be directly compared.

5.2.4. Pulsation Influence

In the preceding subsections, the influence of compressor geometry-related factors was investigated. An intriguing effect was observed for vaneless diffuser designs with ported shroud, suggesting a surge margin improvement under strong pulsation. Such designs are generally favored in heavy-duty commercial vehicle compressor development due to their robustness and ease of manufacture. Consequently, a more extensive study on pulsation influence is conducted, varying pulser frequency, orifice size, and two compressor speeds. All parameters are statistically independent, and the DoE is fully factorial in the relevant areas. Figure 5.7 presents the resulting correlation matrix and response surface plot for 76% compressor speed. For 6-Cylinder Diesel engines, surge-relevant pulse frequencies typically lie between 20-40Hz, depending on multiple factors such as critical engine speed and EGR strategy.



(a) correlation matrix

(b) response surface plot

Figure 5.7.: influence of pulsation on surge margin

The correlation matrix indicates weak linear correlations for turbocharger and pulser speed, and no correlation for orifice size. This suggests a high non-linearity of the phenomena, particularly since orifice size has been shown to significantly influence surge margin in the previous subsection. The response surface plot corroborates this assumption. A strong surge margin improvement is observed for low pulser speeds and large orifices, followed by a "wave-like" pattern of the response surface along the orifice size and pulser speed axes.

Figure 5.8 provides a top view of the response surface plot, resulting in a heat map that indicates the surge margin shift. Dark blue colors denote a deterioration in surge margin, while red indicates an improvement.

Areas of high uncertainty are also highlighted. The rectangular region between 10-45% orifice size exhibits pure regression uncertainty. Preliminary measurements indicated negligible pulse generation for these sizes, resulting in no significant shift, as shown in Figure 5.6a. Thus, physical testing in these areas is unnecessary. However, numerical artifacts such as overshoots may occur in regression calculations.

The region between 60-87Hz is marked by uncertainty due to a lack of measurements. Tests were not conducted in this range as the corresponding engine speeds are 2400 rpm and above. Instead, tests were performed at the limits of the PFD's capability to detect the main trends.

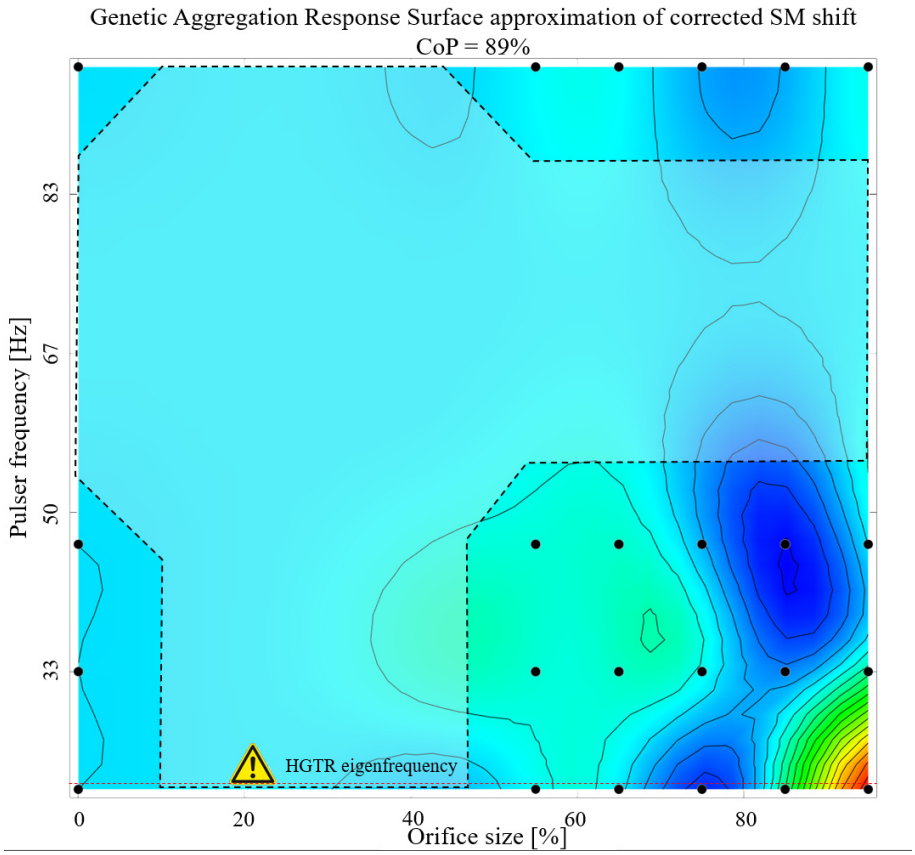


Figure 5.8.: influence of pulsation on surge margin - heatmap; areas with high uncertainty highlighted

The most prominent feature, the spike at low pulser frequency with a large orifice, is not a measurement error but the result of excitation at a test rig eigenfrequency. This was initially noted by strong vibrations of the test bench at the beginning of testing, when the compressor operated in a stable area of the compressor map close to choke. Further analysis revealed that the resulting acoustic wavelength of the pulser was 0.1m,

with many parts of the test bench being multiples of this wavelength. Consequently, the HGTR is artificially turned into a Helmholtz resonator, bringing it to mild surge frequency. Thus, at some point, the strong forced mild surge counteracts the onset of deep surge, leading to a significant delay in surge and highlighting the difficulty in determining surge.

The deterioration at smaller orifice sizes with the same frequency does not contradict this theory. At some point, the pulse interaction becomes strong enough to trigger a stall event at higher mass flows but is too weak to maintain the forced oscillation against the developing deep surge, hence resulting in a worse surge margin.

This effect is actually observed in all four tested pulser speed variations and, with the exception of the Helmholtz frequency data, occurs at the 75% orifice. From there, the surge margin first decreases before the largest orifice leads to surge neutrality due to the strong forced reaction.

The effect becomes weaker with increasing pulser speed. This is due to the change in the hysteresis curve, as experimentally shown, amongst others, in [1]. Low pulser speeds result in low pressure, high mass flow variations, whereas higher pulser speeds create high pressure, low mass flow variations. Hence, its influence on surge diminishes.

5.2.5. Summary

In the foregone measurement campaign, different compressors exposed to varying pulsating outlet conditions have been investigated.

Firstly, it was found that the inclusion of a ported shroud can detrimentally change the behaviour of a compressor geometry. In the presented case, the compressors surge margin deteriorated with the inclusion of a ported shroud, whereas it improved without a ported shroud. This finding is important as it links much of the literature to experience in industry. Literature mainly uses non ported shroud compressors, leading to surge margin improvements. Not only could this be confirmed by measurements, it also shows that the different results are not contradictory but due to the inclusion of ported shrouds.

Secondly, it was experimentally determined that vaned and vaneless diffuser design compressors respond differently to pulsating conditions. While a vaned diffuser compressor may stall and experience a deteriorating surge margin with increasing pulsation levels, a vaneless diffuser design can recover and even improve the surge margin. This difference is attributed to the distinct surge triggers in the compressors, allowing the pulse to interact with the slower path to surge in vaneless diffuser designs. This finding can help link literature focused on stationary equipment, where vaned diffusers are more commonly used.

Furthermore, it was found that even a comparatively simple setup, such as a PFD

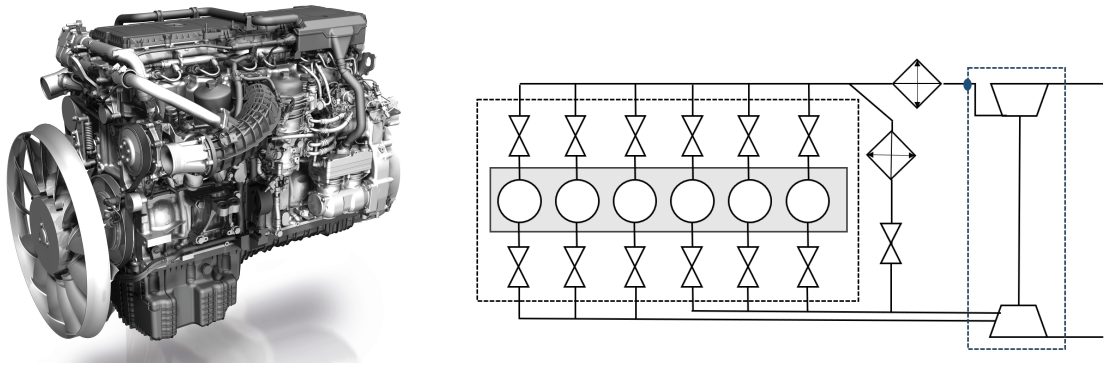
with only three variables (pulser and compressor speed, orifice size), exhibits high non-linearity, with improvements or deteriorations occurring with very small changes. This aligns with publications that have noted both improvements and deteriorations.

These findings show that testing under pulsating conditions must be approached with great care. The high sensitivity and non-linearity of the parameters can lead to significant discrepancies and even opposing trends. Therefore, preliminary testing should only be conducted if the exact engine environment is understood and can be accurately replicated with the PFD. Thus, a thorough investigation of the ETR is essential.

5.3. Characterization of the Engine Test Rig Environment

5.3.1. Engine Hardware

An OM471 prototype engine is used for surge measurements at the ETR. Compared to its series configuration, the engine is equipped with a Miller-type camshaft. Miller valve timing is used primarily to lower peak combustion temperatures, which helps reduce raw NOx emissions [5]. Although emissions reduction is not relevant to the present surge analysis, the Miller camshaft is retained in this work because it also shifts the engine operating line by requiring higher boost pressure at lower mass flow rates, and thus becomes more critical for the surge behaviour investigated here. Figure 5.9 shows the engine and its overall layout.



(a) engine (b) engine layout

Figure 5.9.: OM471 test engine

Unlike other engines, the OM47x engine platform uses non-axisymmetric EGR. The first three cylinders power the turbine, while a smaller turbine-volute cross-section increases the backpressure for cylinders 4-6. This allows a positive pressure gradient between engine intake and outlet section and thus a recirculation of exhaust gases. [114]

Additional to standard prototype engine measurement probes, a Kistler 4075A V200S pressure transducer is installed at the compressor outlet - charge air pipe interface to allow capture of the transient outlet conditions of the compressor. The sensor is equipped

with a waterjacket to avoid temperature-induced drift due to its close proximity to the engine outlet pipe. All tests are performed with compressor B.

5.3.2. Surge Testing Procedure

As the engine includes multiple components that interact with each other, automatic surge detection algorithms are not favourable. Instead, surge is acoustically detected by the test bench operator through the typical buffeting noise and sudden pressure rise in the inlet pipe. Hence, only deep surge can be reliably detected.

The procedure for surge testing is as follows. First, a critical engine speed is selected and the engine is brought to the corresponding full load operating point. Then, the EGR valve is gradually opened until the buffeting noise is heard. This often coincides with violent movement of the whole inlet ducting and vibration of the surrounding components. The EGR valve is immediately closed to reduce the bypass flow, thus allowing the compressor to recover. This process is repeated multiple times to take the manual aspects and corresponding deviations into account. Finally, pressure ratio and mass flow rate are averaged over the measurements.

5.3.3. Effects of the Surge Testing Procedure on the Compressor Operating Point

During engine surge testing, multiple variables are changed at the same time. This is due to the close coupling of the components and denies a quantification of single influences. Figure 5.10 illustrates the changes in a compressor map.

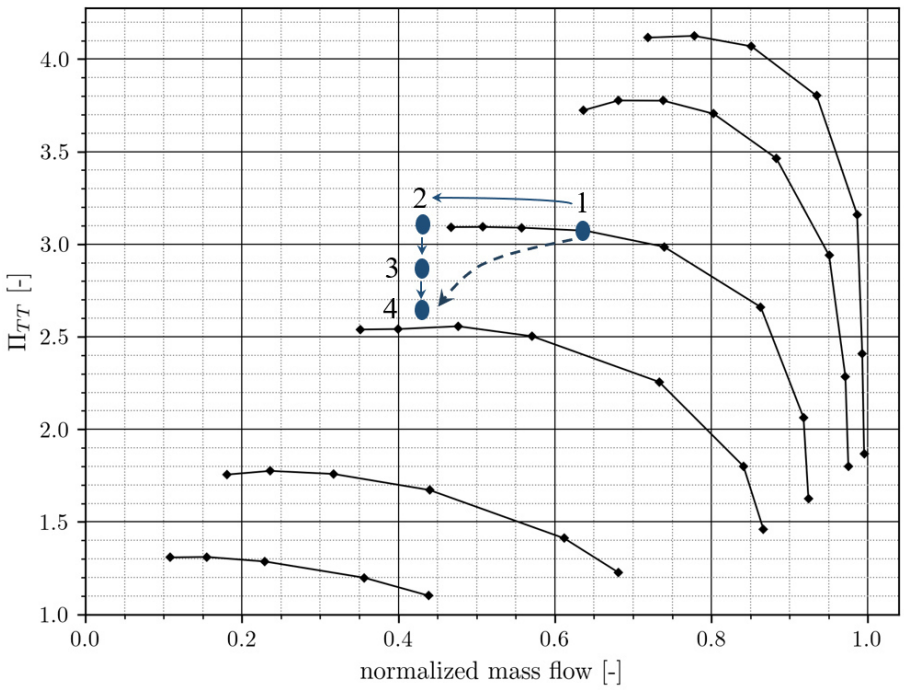


Figure 5.10.: change of operating conditions during engine surge testing

Surge testing begins with the compressor operating at the stable engine full-load condition (1).
The EGR valve is opened and high pressure exhaust gases are pushed into the engine intake manifold. Hence, the compressor mass flow is reduced (2).
With a part of the exhaust gas recirculating, the available energy for the turbine is reduced. As a result, the turbine decelerates until energy balance is re-established. Thus, the turbocharger speed is reduced. This leads to a drop in the compressor pressure ratio (3).
The exhaust gases are of highly pulsating nature and the pressure waves travel upstream through the intercooler to the compressor outlet, overlaying with the engine intake valve pulses. The compressor operates in a more transient pulsating condition and its pressure ratio is reduced (4).
As all effects happen simultaneously, the actual operation point shift roughly follows the dashed arrow.

Significant changes can also be seen in the transient static pressure signals at compressor outlet, see Fig. 5.11. The graph shows the full load and last stable EGR rate static pressure signal of the transducer, plotted and averaged over the crankshaft angle.

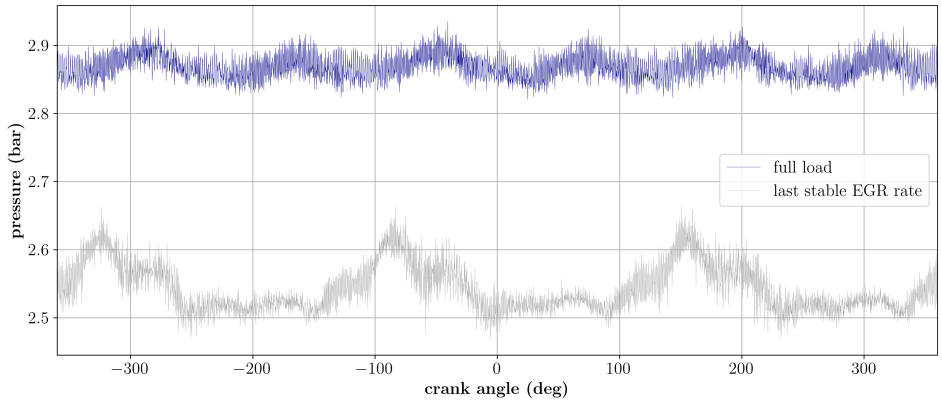


Figure 5.11.: crankshaft resolved p_2 at ETR

At engine design point, a sinusoidal pressure wave occurs. As expected, its position in the crank angle diagram matches well with the opening and closing of the inlet valves. A somewhat similar signal shape was used in the investigation by Barrera-Medrano [53].

However, at the last stable point, the outlet pressure fluctuation is characterized by a triangular peak occurring at every second outlet valve opening. This phenomenon is clearly associated with the engine's non-axisymmetric EGR system. It becomes obvious that the engine exhaust pulses are not limited to the turbine, but also heavily influence the charge air components and become the dominating effect. With EGR, the opening and closing of the inlet valves are barely discernible not only because of their comparably weak amplitude, but also due to EGR wave reflections.

The measurements also confirm and highlight the theoretically derived pressure drop. Compared to the full load counterpart, the charge air pressure drops by 0.3bar, which the engine has to counteract by injecting more fuel, hence reducing engine efficiency.

In summary, the relevant surge operating condition is not caused by intake valve interactions alone. Instead, it results from a complex interplay between the engine, turbocharger, and EGR system. This contrasts sharply with some literature, such as Barrera Medrano [1] and Shu [59], who investigated non-EGR systems. Consequently, the knowledge from these studies cannot be directly applied, as the systems are fundamentally different.

5.4. Conclusions

In the preceding sections, extensive testing at both HGTR and ETR was conducted to allow analysis of compressors operating in transient environments.

On the HGTR, it was found that ported shrouds can significantly alter the compressor's response. Additionally, experiments showed that vaneless and vaned diffuser designs react very differently under pulsating conditions. It was also discovered that even in relatively simple setups, shifts in surge margin are highly non-linear and sensitive.

On the ETR, it was observed that compressor operating conditions change significantly during surge testing. The final operating condition results from the energy balance in the turbocharger, which dictates the rotational speed, reduced mass flow due to the EGR, triangular pressure waves from non-axisymmetric EGR, and resulting wave reflections.

These findings lead to the following conclusions:

- A compressors response to pulsating conditions cannot be evaluated at early design stages. This is especially the case when ported shrouds are considered, as the observed trends are likely to oppose each other.

- The highly non-linear correlations between surge margin and pulsation magnitude prevent a single-point evaluation. It is not beneficial if a compressor is more surge stable at very high pulsations but deteriorates at mild pulsation magnitudes, as engine pulses gradually increase. Therefore, different pulse magnitudes must be investigated to avoid misleading conclusions during development.

- The complex interaction of multiple effects on an engine cannot be properly replicated at an HGTR. A PFD cannot recreate the triangular shape of the pressure signal, leading to uncertainty about its validity. Since the pressure signal results from the

entire system rather than an independent intake valve, a true predictive manner of the PFD cannot be achieved either. Instead, a very similar turbocharger must be tested on an engine, with pulses measured and then replicated with the PFD.

- Eigenfrequencies of different test benches play a major role in surge margin shifts.

- Surge definitions are crucial in determining improvements or deteriorations. Some definitions are so sensitive that even a normal stable pulsating condition is detected as surge, while others cannot detect partial flow reversal. Therefore, a robust and consistent surge definition must be used across all measurements and test rigs.

In conclusion, considering transient environments in early design phases is not feasible. The complexity of the effects requires consideration in later phases, where the design, surrounding environment, and interaction with other components are well understood.

Importantly, the experiments showed that the opposing results reported in literature and experienced in industry are not contradictory. Instead, they are due to different design features, test bench setups, and surge definitions, highlighting the high complexity of surge.

6. Reduced Order Modeling and Optimization

As highlighted in Chapter 1, the development of compressors has become increasingly challenging, with manufacturers striving to achieve higher efficiencies while maintaining or even expanding the compressor map width. To address these challenges, automated surrogate-model based optimization methods, such as the ones proposed by Woehr et al. and Abel et al. [74, 99], are employed. However, a significant limitation of these methods is their exclusive focus on mathematical optimization. While this approach enhances efficiency, it often results in a reduced map width due to the lack of engineering insight and surge feedback.

Consequently, constraints based on conservative engineering guidelines such as the ones proposed in [11, 22] must be implemented, which can severely restrict the optimizer's ability to identify improved designs. Therefore, incorporating a fast, accurate, and robust surge feedback mechanism will significantly enhance the optimization capabilities of these methods.

Fast surge feedback can be achieved by utilizing 1D-, or lumped parameter models, which consist of a *compressor model* that provides a compressor map and a *system model* that determines the surge point of the compressor within the system. Then, this information can be fed back to the optimization algorithm.

The Chapter follows these steps, see Figure 6.1. First, a compressor model based on experimental data is introduced (1). Subsequently, a system model is selected, and its determining characteristics are acquired (2). Next, the compressor and system models are integrated into a new, fully automated compressor optimization (3) that combines the process proposed by Abel et al. [99] (4) with the surge feedback loop. An optimization run is performed, and two resulting designs are manufactured and tested on the HGTR. The chapter concludes with a thorough comparison and discussion of the optimization results.

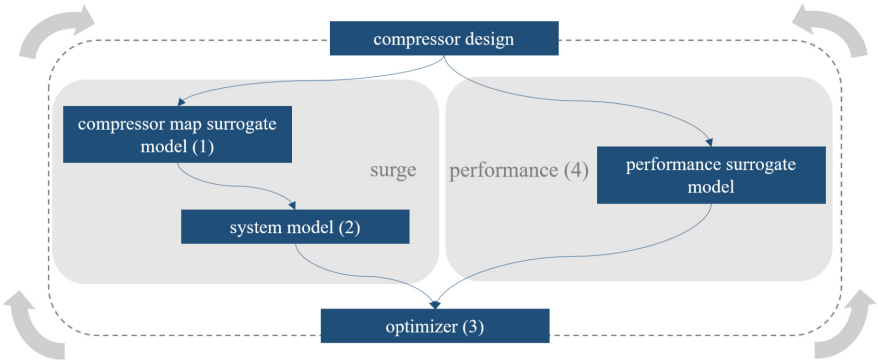


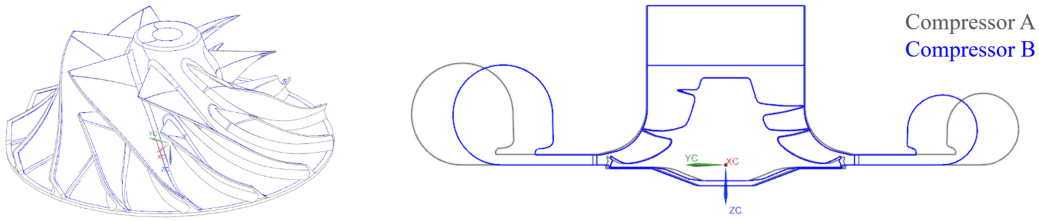
Figure 6.1.: reduced order modeling and optimization approach

6.1. Compressor Performance Prediction Model

The compressor performance prediction model was published as a peer-reviewed conference paper and presented at the *THIESEL 2024 Conference on Thermo- and Fluid Dynamics Processes for Clean Propulsion Powerplants* in Valencia, Spain [115]. Parts of it are presented here again for sake of completeness.
Subsection 6.1.6 was presented at the *Weimar Optimization and Stochastic Day 2024* in Weimar, Germany [107].

In the following subsections, different surrogate models are derived. All surrogate models use the same test bench data as training data. The models are multi-dimensional and connect geometric parameters, tip speed and the mass flow rate with the corresponding output variable: $y = f(geometry, u_2, \dot{m})$. Geometric input parameters were excluded from the model when no statistically relevant influence was found. All compressor performance data was measured at the HGTR. The compressor set contains designs that have a 7+7 impeller, vaneless diffusers, linear A/R-ratio volutes, and do not have a ported shroud or casing treatment.

For validation purposes, compressor A is introduced. It is a typical high-performance compressor resulting from an automated optimization methodology and exhibits a higher efficiency, but lower map width compared to compressor B. Figure 6.2 shows the geometrical comparison between both compressors.



(a) impellers A, B

(b) cross-section fluid volume compressor A, B

Figure 6.2.: comparison of compressors A, B

6.1.1. Pressure Ratio Surrogate Model Stabilization

A surrogate model, solely based on test bench data, is shown in Fig. 6.3 as grey speedlines. Its CoP was found to be superior to other surrogate models, although it was carefully checked that this was not due to overfitting.

The surrogate model generally follows its training data ("test" in the figure), but there are deviations in the choke mass flow. This is due to the steep slope of the compressor curve, which is a common problem in surrogate modelling. Choke is a crucial parameter in compressor design but can be accurately predicted using RANS. Hence, choke range

is not of interest for the methodology presented here, and this effect is not investigated further.

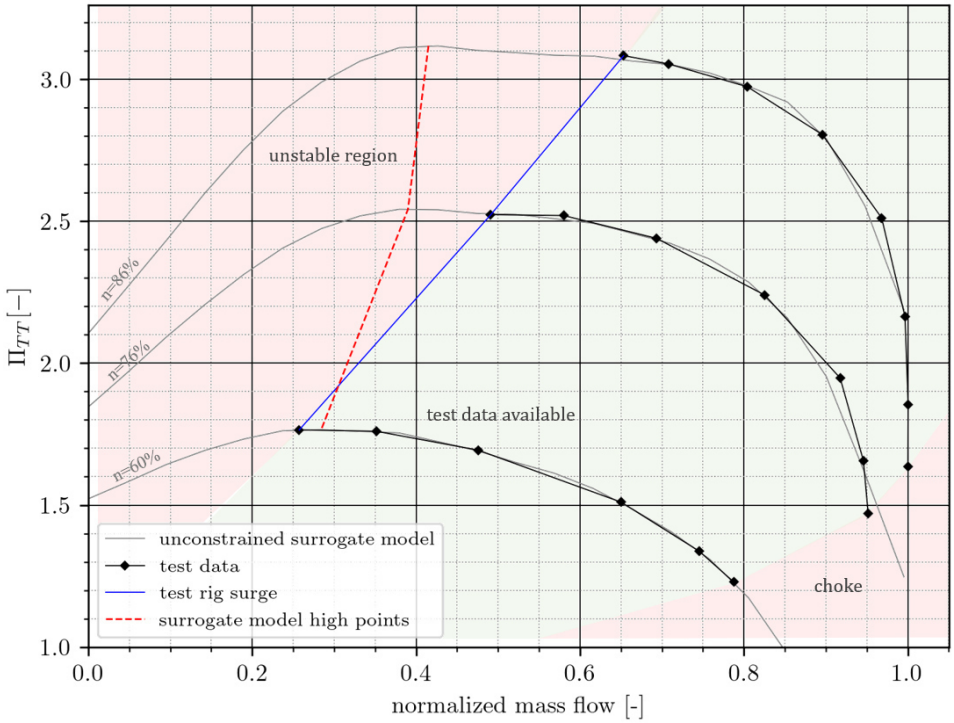


Figure 6.3.: test data and surrogate model- compressor A

On the left-hand side of the training data, or what can also be described as the unstable region of the compressor on the test bench, the surrogate model estimates an increase in the pressure ratio before the typical positive slope develops. Any surge calculation based on this surrogate model is therefore very inaccurate and not useful in any kind of development.

To suppress the unphysical behaviour, additional support points must be added. This could be done by measurements in the unstable region. In the past, some authors [116, 49] have succeeded in achieving this for small automotive compressors. However, the compressors considered in this study are three times larger and Gharaibeh [117] concludes that measurements for such sizes are not feasible.

In the absence of experimental data, it is necessary to use data obtained by calculation. This is generally considered a poor approach, as the discrepancies between calculations and experiments degrade the accuracy of the surrogate model. Consequently, the calculated support points should be situated at a considerable distance from the region of interest, in order to stabilise the surrogate model without affecting its prediction accuracy in the region of interest.

The *Radial Equilibrium Theory*, (RET) is employed by several authors [22, 118, 116, 119]

to calculate the pressure ratio of the compressor at zero mass flow, as illustrated in eqn. 6.1. Thus, it can be regarded a suitable boundary condition for the surrogate model. Dehner et al. [119] propose the use of a constant multiplier K to enhance the alignment between calculations and measurements. The derivation of the equation can be found in annex A.

$$PR_0 = K\left[1 + \frac{\gamma - 1}{2\gamma RT_1}\omega^2(r_2^2 - r_1^2)\right]^{\frac{\gamma}{\gamma-1}} \tag{6.1}$$

In case of the surrogate model, K can additionally be used to improve its prediction accuracy. Therefore, an optimization, eqn. 6.3 is introduced, with $f(\dot{m}_{ref}, K)$ being the surrogate model and $g(\dot{m}_{ref})$ being the measured Π_{TT} curve. Figure 6.4 shows the optimization procedure.

$$\min_{K=0.9...1.1}(|\Delta\dot{m}_{ref}|) \tag{6.2}$$

$$\Delta\dot{m}_{ref} = [f'(\dot{m}_{ref}, K) = 0] - [g'(\dot{m}_{ref}) = 0] \tag{6.3}$$

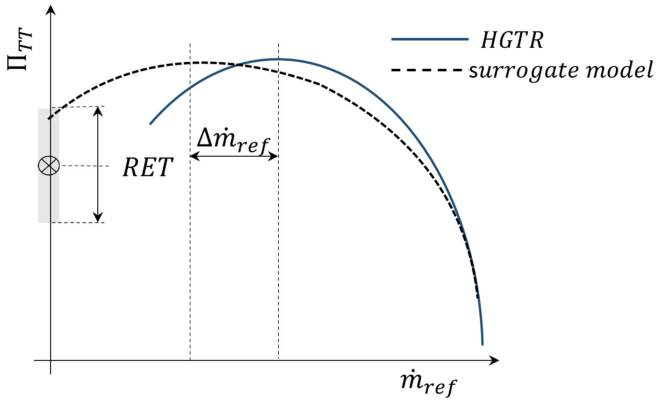


Figure 6.4.: surrogate model optimization procedure

The procedure is implemented in Ansys OptiSlang and a variant of the Nelder-Mead SIMPLEX algorithm [120] is used to find the optimum solution. The program flow chart is shown in Fig. B.1 in the annex.

The optimization took 109 iterations to converge, and $\triangle\dot{m}_{ref}$ reduced to 35% of its initial value. K is 1.089, which is within the range of the work of Dehner et al. [119]. This indicates that the optimization is not a tuning overfit, but rather based on physical effects that cannot be modeled with the RET. The optimized surrogate model is depicted in green in Fig. 6.5. The graph illustrates how the applied boundary condition effectively suppresses the numerical overshoot in the unstable region. Instead of maintaining the negative slope, the surrogate model develops a positive slope and drops almost linearly in the direction of the introduced boundary condition at a mass flow of zero.

The optimisation of K also demonstrates the predicted enhancements in the precision of the surrogate model within the stable operational range of the compressor. This is most apparent for the second speed line, where the prediction of the surrogate model is well within the measurement accuracy of the test rig. Additionally, the general response surface has become more uniform.

At the highest speed line, an overshoot can be identified, which is attributable to the fact that K is dependent on the compressor speed [119]. Nevertheless, the overshoot remains within 1.5% of the measured value, which is within the same range as the deviation of the unconstrained surrogate model due to its coarser response surface.

6.1.2. Analytical Extrapolation

Although the surrogate model has improved significantly, the response surface does not necessarily represent the true quasi-steady behavior. The few successful measurements of the unstable region indicate a third-order polynomial shape, with a low point at zero mass flow [116][14]. This observation contradicts the stabilized surrogate model, which has an almost constant gradient. In certain applications, linear extrapolation is employed as it has minimal impact on the modelling of surge cycles [121], but here the pressure ratio is later used to calculate the efficiency. Thus, the third-order polynomial equation 6.4 of Moore and Greitzer [122] is coupled with the tuned surrogate model.

$$\Pi_{TT} = \Pi_{TT0} + \beta \left[1 + 1.5 \left(\frac{\dot{m}_{ref}}{\phi} - 1 \right) - 0.5 \left(\frac{\dot{m}_{ref}}{\phi} - 1 \right)^3 \right] \tag{6.4}$$

Its determining parameters are calculated on the basis of the constrained surrogate model and are individual for each compressor design. The final result can be seen as the dark blue line in Fig. 6.5.

[14] Measurements conducted in [49] show a change in this characteristic at high compressor speeds, where a vertical asymptote develops at very small negative mass flows. The authors observed that this behaviour appears to depend on the test starting conditions. Due to catastrophic failure of the turbocharger, this could not be investigated further, leaving it unclear whether the effect is related to the compressor or system.

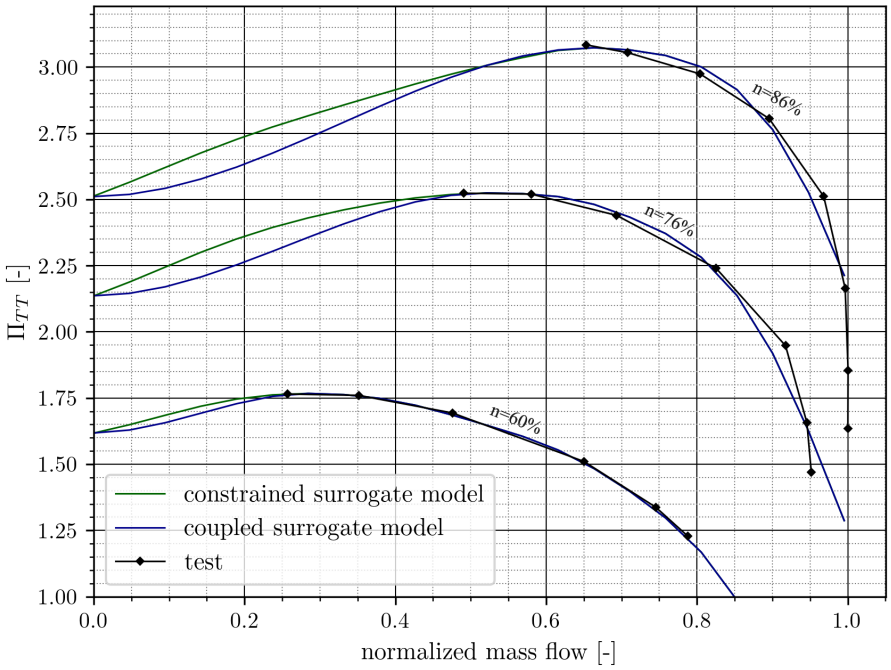


Figure 6.5.: constrained and coupled surrogate models- compressor A

6.1.3. Efficiency Modeling

A surrogate model for efficiency faces two significant challenges: firstly, the problem of identifying an appropriate boundary condition, and secondly, the difficulty of evaluating the overall shape of the response surface in the unstable region. As the value in question is the result of a calculation, it can be obtained from other, more direct parameters, which provide a more reliable and robust solution. Recalling eqn. 2.15 for the isentropic efficiency and considering the surrogate model for the pressure ratio, the only unknown variable is the total temperature at compressor outlet T_{2T}. However, this variable cannot be modeled directly, as T_{2T} is not defined at a mass flow of zero. Nevertheless, it can be derived using the definition of shaft work W_{Shaft}, as given in equation 6.5. The equation for shaft work also provides a boundary condition for a mass flow of zero [15].

$$W_{Shaft} = \dot{m}_{ref} c_p (T_{2T} - T_{1T}) \tag{6.5}$$

The combination of eqn. 6.5 and 2.15 lead to eqn. 6.6. Since c_p is dependent on T_{2T}, the equation is solved iterative.

$$\eta_{is} = \frac{T_{1T} \dot{m}_{ref} c_p}{W_{Shaft}} \left[(\Pi_{TT})^{\frac{\gamma-1}{\gamma}} - 1 \right] \tag{6.6}$$

Several algorithms, including Polynomial Regression, Kriging and Deep Learning, were

[15] It is noted that this follows from the standard adiabatic treatment used for the test bench and compressor maps, and does not reflect the actual physics at zero mass flow, where the process is strongly diabatic.

compared in terms of their CoP value and the general form of their response surface. The response of the surrogate model and a comparison between predicted and measured shaft work is shown in Fig. 6.6.

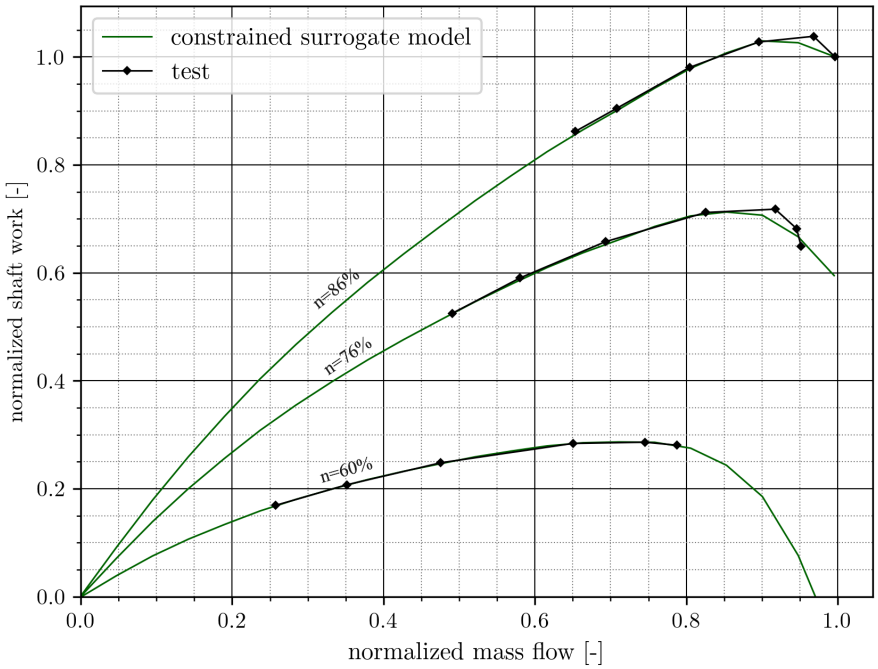


Figure 6.6.: shaft work surrogate model and HGTR measurement

As with the Π_{TT} surrogate model, the applied boundary condition stabilises the response surface over a wide range of the compressor map. If the deviations due to the steep gradient in the choke area are not taken into account, the surrogate model is within the measurement accuracy of the test rig. Since the efficiency calculation is based on two surrogate models, the final result is presented and discussed in the next section.

6.1.4. Validation of the Methodology

The methodology is validated by running the surrogate model in regression mode, using compressor A. This enables the prediction errors of the surrogate model to be minimized and the coupling of the methods, their accuracy and form to be evaluated. Figures 6.7 and 6.8 show the surrogate models and the URANS simulations in a pressure and efficiency map.

The derived Π_{TT}-model follows the measurements within measurement accuracy for the second speedline. The transition point of the coupled model, at which the surrogate model transitions to the analytical equation is smooth and imperceptible. Furthermore, the calculated curve is within the measurement accuracy of the test rig results, thereby

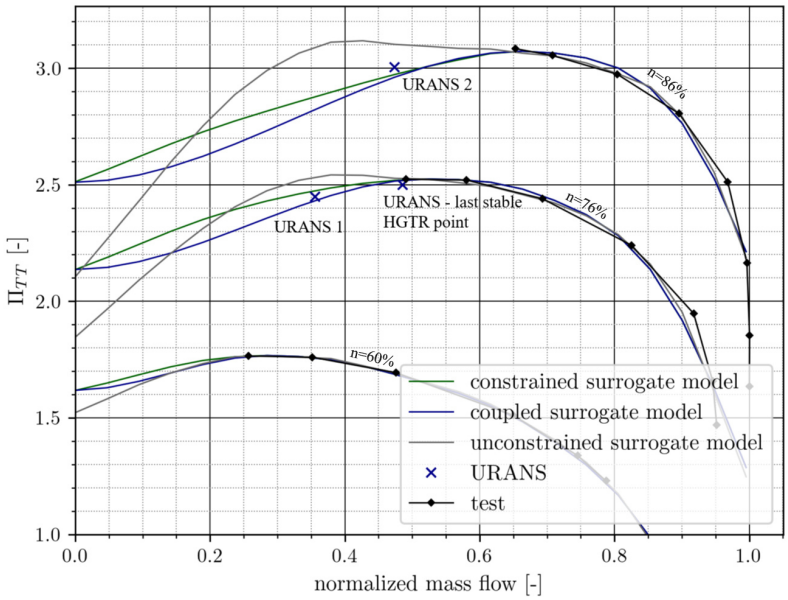


Figure 6.7.: surrogate model regression and HGTR result- pressure ratio, compressor A

corroborating the validity of the coupling.

The URANS simulations, in which all downstream piping was removed to obtain a "stable" solution in the otherwise unstable regime, demonstrate only minor differences in comparison to the new methodology. URANS No. 1 is almost on point with less than 1% deviation in the pressure ratio, while URANS No. 2 shows a deviation of 2%. This deviation is related to the fact that the surrogate model for the high compressor speed is at the edge of its design space. This becomes clear from the difference between regression and measurement, leading to the conclusion that the methodology is valid for Π_{TT}.

The calculated efficiency exhibits a maximum deviation of 1.8% (normalized), which is observed at the optimal operating point. The error is reduced to the measurement accuracy at the last stable test bench point. Once more, the maximum deviation is observed at the highest compressor speed, which is related to the limitation of the Π_{TT}-surrogate model design space. It is most accurate at the lowest speed.

The URANS simulations demonstrate a high degree of agreement with the extrapolation technique. The normalized deviation is 3% for the second speed line and 1% for the highest speed, which are within the deviation between URANS and the test rig at the last stable point.

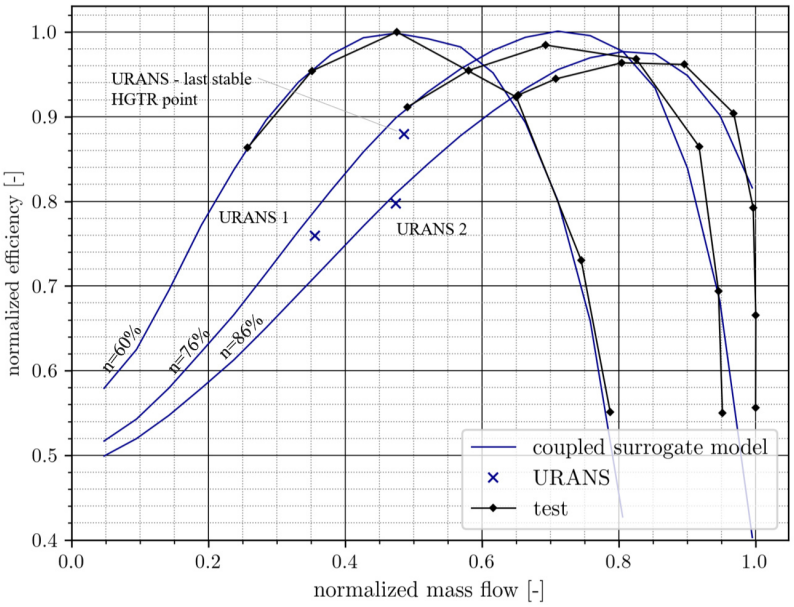


Figure 6.8.: surrogate model regression and HGTR result- efficiency, compressor A

6.1.5. Suitability for Prediction

Following the confirmation of the model's regression capabilities, the prediction is tested with compressor B, which was excluded from the training data. The results are presented in Fig. 6.9 and 6.10.

The constrained Π_{TT}-surrogate model demonstrates a high degree of agreement with the measurements. The pressure ratio is slightly overestimated, but the constrained model follows the measurements with an almost constant offset in the area of interest. However, the constrained model does not agree well with the results of the URANS simulations, which is most obvious for the last speed line.

The coupled surrogate model agrees well with the URANS results but shows an unfavorable slope in the surge critical region when compared to test bench data. This is most obvious for the second speed line, where the measured and predicted curve intersect. It is therefore concluded that the coupled surrogate model should not be used in an attempt to improve the accuracy of the model in the most critical area for test bench and engine surge.

A speed line obtained by RANS CFD is also included in the figure. In the numerically stable region, the RANS speed line is comparable, or more accurate, than the model; the accuracy improves as the operating points shift closer to the compressors design point. Nevertheless, the RANS becomes numerically unstable for mass flows below 0.4, rendering it incapable of providing any useful information in the vicinity of surge.

The efficiency prediction based on the constrained surrogate model is in good agreement with test data for the last two speed lines, but there is a discrepancy for the first one. An error analysis indicates that this is due to uncertainty in the shaft work surrogate

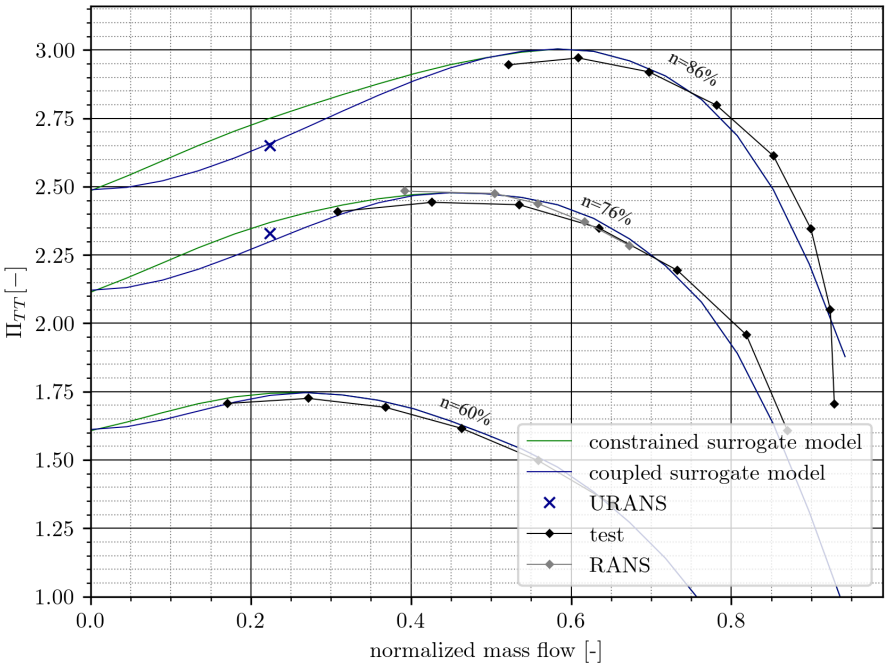


Figure 6.9.: surrogate model prediction and HGTR result- pressure ratio, compressor B

model, which overestimates the shaft work by 8% for the first speedline. Consequently, T_{2T} is overestimated, resulting in a maximum decrease in normalized efficiency of 6%. The overestimation is a consequence of the diabatic nature of the test bench, which is most pronounced at low compressor speeds. This phenomenon has been demonstrated, amongst others, by Haug [28]. This, in turn, affects measurement accuracy and introduces noise into the training data, reducing the surrogate models' accuracy. Nevertheless, it is notable that the shape of the response surface closely aligns with the measurements for all speed lines, particularly in the surge region.

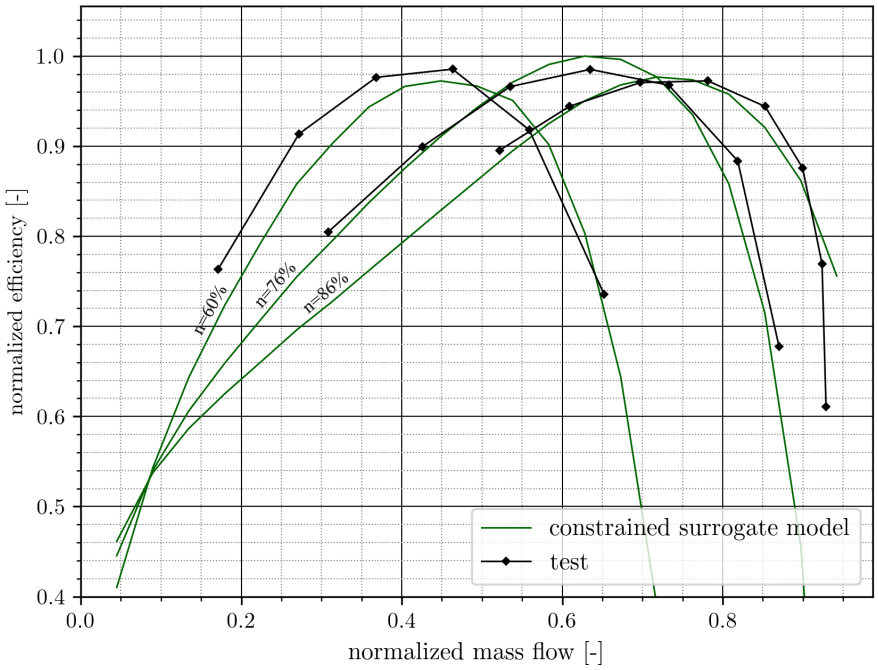


Figure 6.10.: surrogate model prediction and HGTR result- efficiency, compressor B

6.1.6. Addendum: Detection of Erroneous Geometry and Test Bench Stall by the Compressor Performance Prediction Model

The original test bench results of the compressor B hardware is shown in Figure 6.11. For all speedlines, the compressor achieves a higher pressure ratio than the surrogate model predicted. The difference is not constant, but increases with increasing compressor circumferential speed. Also, the shape of the response surface does not follow the measurements, which is most obvious for the 77% speedline.

With the difference between surrogate model and test, as well as the rougher shape of the test bench speedline, a hardware anomaly is likely. Hence, the impeller and the volute were measured with an ATOS optical measurement system and the obtained data overlaid with the CAD model using the "best fit orientation". The relevant results are shown in Figure 6.12.

While the blade geometry is within specified tolerances, the impeller shroud contour is increased. Hence, the gap between impeller blade and the housings‘ shroud contour is significantly reduced, leading to a reduction of the spillage flow driven by the pressure gradient between pressure and suction side of the blade. Thus, the compressor achieves a higher efficiency and pressure ratio, leading to the discrepancy to the surrogate model.

A new compressor wheel was manufactured and the testing was repeated with the new hardware. The results are shown in Figure 6.13.

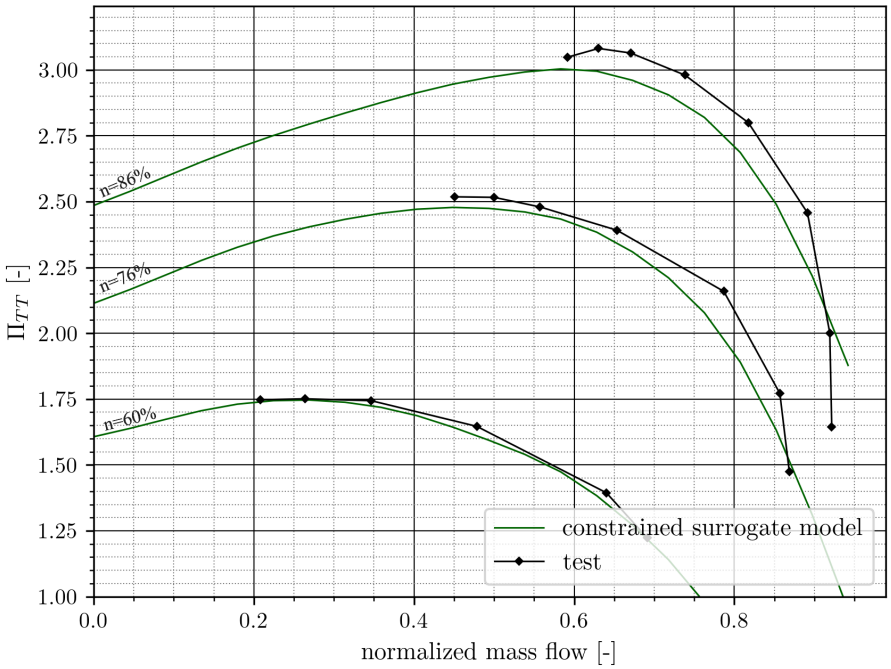


Figure 6.11.: HGTR result: erroneous hardware, compressor B

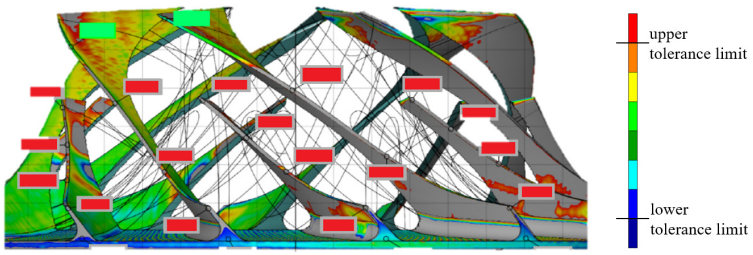


Figure 6.12.: impeller GOM scan

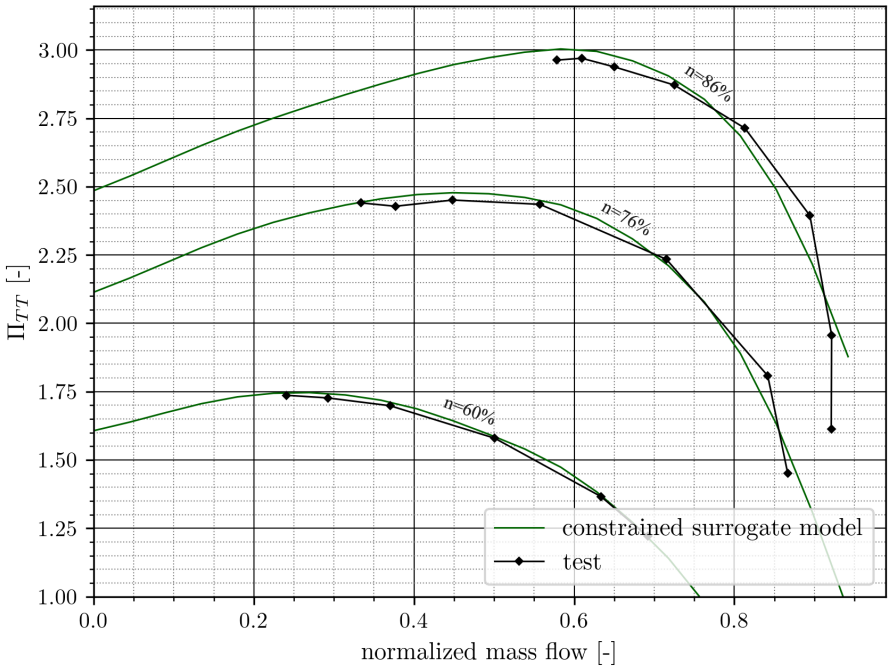


Figure 6.13.: HGTR result: new impeller, compressor B

The new hardware agrees much better with the prediction. The lowest speedline matches perfectly with the surrogate model, and the difference in pressure ratio has significantly reduced for the 77% and 86% speedline. However, for both speedlines, a bump can be seen in the area close to surge, which is in disagreement with the surrogate model.

A bump of this shape is usually considered as a stable stall effect, that reduces the compressor efficiency and pressure ratio. A further indication for the stall is the surge margin improvement, in which the bump occurs. Compared to the original hardware, an 11% improvement in surge mass flow can be reported.

Since the stall can be excited by outer disturbances, e.g. test bench vibrations, turbocharger speed fluctuations or throttle closing steps, testing was repeated on a HGTR designed for passenger car applications. This reduces the outer disturbances to the technical minimum of a HGTR, but also reduces the systems B parameter as the inlet and outlet ducting are smaller. As a result, the surge line will shift to the left. Nevertheless, the shift in surge margin will not have an effect on the quasi-steady compressor characteristic [55, 32].

The measurements on the passenger car test cell showed almost no deviation to the surrogate model and were used for the validation of the surrogate models predictive capability as presented in the section before. It is emphasized that this approach is valid as an undesired, transient effect of the HGTR was the origin of the altered compressor characteristic. It hence violated the requirement of a steady measurement environment,

which was solved by using a different test rig.

The findings highlight the predictive capabilities of the compressor model and the reliability of the results. With the compressor model, an erroneously manufactured compressor geometry could be identified, and a stall, linked to the greater outer disturbances of the bigger test cell, could be detected. Thus, the developed model can not only be used as a predictive development tool, but also for validation purposes. This results in a much more reliable set of data while at the same time drastically reducing the amount of time and effort spent currently on geometric measurements and analysis.

6.1.7. Summary

This section introduced a surrogate model to predict compressor maps and presented a method for extending the design space and hence the reliability of the surrogate model in surge-critical areas. The method is based on the RET and uses K as an optimization parameter to stabilize the Π_{TT}-surrogate model. It was further investigated whether an analytical function improves prediction accuracy. Compressor efficiency is calculated via shaft work, which provides a natural boundary condition for zero mass flow.

The findings show that the model is of order four faster than a comparable URANS simulation and can predict compressor maps in less than a minute. Its accuracy is comparable to URANS simulations in the vicinity of surge, and, if the coupled model is considered, it is also comparable to URANS simulations in the deep unstable area. The analysis also showed that the RANS simulations were not able to capture the compressor characteristics in the vicinity of surge, thus significantly reducing their suitability as a source for surge simulations.

A comparison with test data showed that the method can accurately predict the pressure ratio. The efficiency prediction agrees well with the measurements. The slightly larger deviations compared to the pressure ratio prediction are due to an error summation of the two underlaying surrogate models.

The coupled model was found to be accurate for standard high-efficiency compressors and showed little deviation to URANS simulations in the unstable area. However, it was observed that the use of surge-optimized geometries resulted in an unfavorable deviation. Hence, it is recommended that the constrained surrogate model be used, although this may introduce significant errors in the deep unstable area of the compressor.

Additionally, the predictive capabilities of the surrogate models were proven by the detection of erroneous hardware and the occurrence of a measurement error at the test bench. With the hardware error corrected and the test bench swapped to a passenger car turbocharger test bench, a very good fit between prediction and measurement could be achieved. This led to the further use of the surrogate models not only as a predictive

tool, but also a verification tool for hardware testing, significantly increasing the test data reliability.

6.2. 1D System Model

With the compressor model successfully established, a 1D system model is required to model the interaction of the compressor with the HGTR environment. Given the findings in Chapter 5, showing that pulse interaction is highly non-linear and accurate modeling is currently not feasible, the model does not need to account for transient environments. This consideration allows for the potential use of lumped parameter models.

Considering the extensive availability of well-documented models [32, 54, 33, 123, 118, 124], partially available models [125, 121], and proprietary models, a literature survey is conducted to evaluate the feasibility of using an existing model rather than developing a model from first principles.

With a suitable model selected, its determining parameters are derived based on fundamental assumptions and test bench measurements. Last, the model's surge prediction is validated using test bench measurements, and the results are discussed.

6.2.1. Compression System 1D Modeling Approach

Greitzer Model

The Greitzer Model has already been introduced in Chapter 2. However, a comparison between the original test environment and the one used in the work herein has not been presented. Thus, the main differences are highlighted here.

The Greitzer model was originally derived for axial compressors, which introduces differences between the test benches used for testing compressors. As shown in the original paper [52], the design of the axial compressor test rig can be clearly divided into an inlet section, plenum, and outlet section.

This contrasts with a turbocharger HGTR, which resembles a pipeline system. For example, the plenum and outlet pipe are not distinguishable, as the measurement pipe directly connects to a throttle valve of the same diameter. Furthermore, the inlet piping on an industrial turbocharger test stand is much more complex, containing multiple elbows, filters, and sometimes even throttle valves.

These differences lead to challenges in modeling, as no characteristic lengths can be directly acquired. Instead, the B parameter is often the result of numerical tuning, leading to the risk of over-fitting the model.

Another issue that must be addressed in a predictive surrogate-model context is the flow field time constant τ, which represents the time lag between the compressor steady-state curve and its transient behavior. This requires knowledge of the compressor's stall behavior, which, in the optimization context, is not provided. As this time constant is also used as a fitting parameter [46], there is a significant risk of over-fitting.

Commercial 1D Codes

Commercial 1D codes play an important role in the development of combustion engines by offering numerically robust environments that allow heuristic optimization procedures. They partially rely on methods such as the one introduced by Theotokatos and Kyrtatos [118][121], which are extended Greitzer models specifically designed for turbocharging applications.

However, the emphasis on numerical robustness presents challenges in surge prediction. To achieve numerically stable results, an artificial negative slope is introduced in the compressor model to replace the "real" steady-state positive slopes of a compressor map in its unstable regime [121]. Additionally, damping parameters based on the overall system are incorporated [121].

This approach is generally sufficient for modeling compressor unsteady behavior near, or in, surge. However, a true predictive modeling, where the surge line is unknown, is not feasible with this method.

To address this limitation, De Bellis et al. [126] propose the use of 0D capacities upstream and downstream of the compressor template, which account for mass and energy storage. It is suggested that the volume of these storages is related to the inlet ducting, compressor volume, and downstream ducting. However, the artificial negative slope remains, becoming a tuning parameter that must be carefully adjusted.

Simplified Greitzer Model by Buehler et al. [46]

Driven by the strong industrial demand for fast and accurate surge prediction, Buehler et al. [46] developed a Greitzer-based model that more accurately represents the geometry of a HGTR environment and omits the compressor's time lag. In this approach, an inlet throttle is added to the inlet pipe, while the outlet pipe is removed. Instead, the plenum is connected directly to the outlet throttle.

The inlet throttle accounts for the extensive inlet piping and measurement equipment of the test bench. The absence of the outlet pipe is addressed by removing the corresponding term from Greitzers original set of equations. Both the compressor's time lag and Fink's correction for compressor speed are neglected, as the industrial focus is on predicting the onset of instability rather than modeling instability cycles.

A small perturbation analysis of the resulting set of equations leads to a "generally

valid stability criterion D", as shown in eqn. 6.7, derived from the system's eigenvalues. A detailed derivation can be found in [54].

$$D = \left(\frac{L_c}{A_c} - \frac{V(c - g_1)g_2}{a_3^2} \right) \tag{6.7}$$

Here, L_C, V and A_C represent the inlet piping length and cross-sectional area, and volume of the outlet plenum, respectively. c, g_1 and g_2 denote the quasi-steady compressor and throttle characteristics.

The model was validated with experiments, demonstrating its ability to accurately capture changes in the outlet plenum volume and inlet piping [46].

An initial numerical analysis conducted by the author showed that the model follows the same trends as those discovered experimentally by Schäfer et al. [55]. This is noteworthy because the experimental results in the original study could not be connected to 1D results based on a more complex Theotokatos-Kyrtatos-based model [55]. This indicates that the main surge feature in an HGTR environment can be captured with the simplified model.

Haeckel et al. [47] extend the work of Buehler et al. [54] by combining the parameter D with RANS generated compressor wheel maps. A negative value of D is interpreted as system surge. While the approach does not yield time-resolved data, the authors argue that such temporal resolution is not required in industrial settings, where both stall and surge must be avoided. Therefore, the classification of the instability is considered secondary to the fast and accurate prediction of its onset. [47]

Turbodyna

Turbodyna [123] uses a modeling technique that meshes the compressor in a true 1D fashion instead of applying classic interfaces, see Figure 6.14. In the rotor section, source terms are added to the Euler equations, thus dropping the direct use of look-up performance maps. As a result, the rotor unsteadiness is correctly modeled, leading to successful and accurate simulations of compressors operating under pulsating conditions or in surge [60, 61, 127].

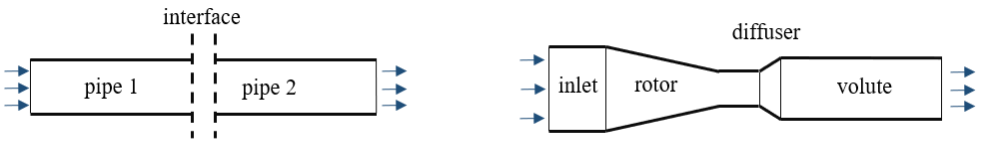


Figure 6.14.: Turbodyna 1D domain. Left: classic modeling[16], Right: Turbodyna[17]

However, Turbodyna has not yet been employed in a test-based manner, as simulated

[16]Used with permission from ASME, from [123], permission conveyed through Copyright Clearance Center, Inc.
[17]Used with permission from ASME, from [127], permission conveyed through Copyright Clearance Center, Inc.

compressor maps have been used as inputs. Therefore, it is necessary to evaluate whether Turbodyna's inputs can be determined from test bench measurement derived models.

Two of Turbodyna's three source terms are Π_{TT} and W_{shaft}, which can be directly modeled by surrogate models (see section 6.1). The third source term is the flow angle θ, which, in the original publication [123], is calculated using W_{shaft}, Δs, and η_{ts}. This approach, however, cannot be applied to test bench data.

On a HGTR, total and static values at the compressor outlet are obtained through an iterative scheme rather than direct measurement, except for static pressure. This is due to the highly turbulent nature of the flow, which cannot be accurately measured. Instead, a fully developed flow in the outlet pipe is assumed, and total and static values are derived by enforcing mass conservation in an iterative scheme. Thus, the calculated flow angle based on η_{ts} will always be zero[18].

Electric test benches partially mitigate this issue, as shaft work (and hence T_{2T}) can be measured indirectly via electric power consumption or by using a torque meter, as demonstrated in [117]. Although θ would still compensate for measurement errors due to mechanical friction, the measurement should be more accurate. However, since all data for the surrogate models were acquired on a HGTR, this information is not available. Therefore, an investigation was not conducted, although it is recommended for future research.

Given the presence of a non-removable, systematic error in the HGTR data, θ must be set to zero to maintain consistency with the assumed physics. Consequently, it is necessary to investigate the system's sensitivity to this adjustment. A stable, representative compressor operating point is considered for this analysis. The pressure ratio is fixed, as it represents the most accurate data available, while the shaft work is varied. With the mass flow rate known and θ set to zero, the sensitivity can be evaluated. The results are presented in Fig. 6.15. All values are normalized with respect to the corresponding target value.

It becomes evident that the mass flow rate is highly sensitive to the shaft work input. A variation of merely 1% causes the mass flow rate to span almost the entire compressor map- from zero to close to the choke limit. This behavior is not unphysical: if the shaft work falls below a certain threshold, the compressor cannot overcome the pressure gradient defined by the pressure ratio. Once this critical value is reached, the mass flow rate jumps towards its design operating point. With no further restrictions, as would be provided by θ, even a marginal increase in shaft work results in a significant increase in mass flow rate.

This finding indicates that Turbodyna cannot be effectively used in a HGTR based

[18] θ actually becomes an indicator of test bench quality: the closer it gets to zero and the more constant the offset, the better the test bench and subsequent data processing.

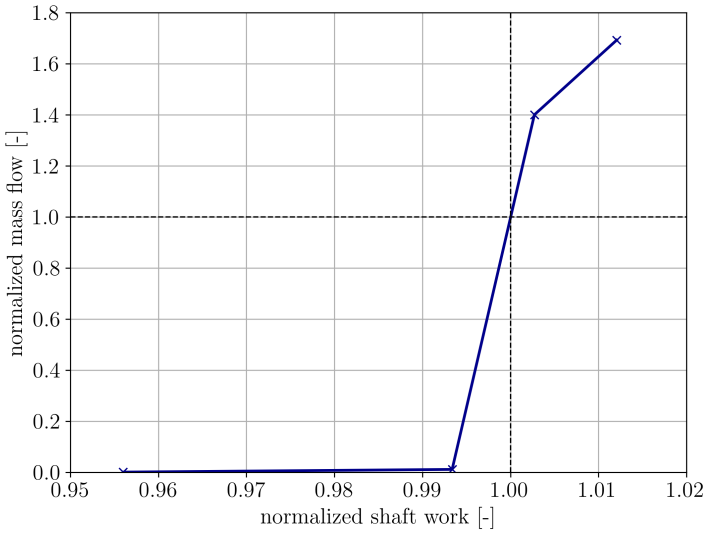


Figure 6.15.: mass flow sensitivity on shaft work when $\theta = 0$

surrogate modeling context. Turbodyna is designed to address the "interface" compressor modeling, which is physically inconsistent, and to enable proper simulation of pulse interaction. To achieve this, Turbodyna requires physically consistent data. However, this consistency cannot be achieved using HGTR-based surrogate models. The HGTR, by design, introduces a systematic error, leading to consistent but simplified data. A surrogate model will then introduce estimation errors which, when compared to Turbodyna's sensitivity due to the HGTR simplification, are too large and prevent stable operation.

1D Compression Model by Powers

Powers developed a mathematical model for surge in radial compressors and validated it with measurements [128, 49, 51, 124]. Unlike many other approaches, this method strictly adheres to the averaging of the 1D Navier-Stokes equation and does not employ lumped-parameter models. The work can be divided into two parts: the derivation of a compressor model and the derivation of a set of equations for the compressor inlet and outlet ducting.

The final model is capable of simulating both mild and deep surge using three tuning parameters: one for friction, one for diffuser stall, and one for impeller stall. In the presented case, the estimated surge is within 5% of the measured surge point.

However, the model requires substantial computational resources compared to the other models, as the PDEs of the system are solved using the Method of Lines. This also necessitates the introduction of a fourth damping parameter to mitigate numerical oscillations, as the resulting ODEs are non-linear [124].

This can become critical, as the damping parameter may also dampen physical oscillations. The risk increases with the variety of compressor setups and decreasing expert interaction, as is common in automated development environments.

Conclusion
Various modeling techniques known in literature were presented and evaluated for their ability to capture the dominant physical effects. Additionally, numerical costs, stability, and robustness of the methods were assessed.

It was found that commercial codes are the most stable option but sacrifice true predictive capability. This is because commercial codes focus on enabling holistic optimization of systems rather than determining stability limits, which would severely constrain optimization capabilities.

The Greitzer model was found to be suitable for some applications but lacks proper modeling of the inlet piping. However, adaptations by Haeckel et al. and Buehler et al. overcome this limitation and even improve the numerical cost and robustness of the solution.

Turbodyna was identified as the most accurate and the only true 1D code capable of capturing surge as a system phenomenon while providing time-resolved data. However, it is very sensitive to the flow angle θ, a parameter that cannot be captured by an HGTR. Thus, its sensitivity precludes its use in an HGTR-based surrogate modeling approach.

Lastly, the simplified Navier-Stokes equation approach by Powers was evaluated. Although the model showed very good agreement with test bench data, its stability is critical as non-linear ODEs must be solved. The model includes damping based on physical assumptions, but it remains unclear how reliable this damping is when different compressors are considered, increasing the risk of over-fitting. Additionally, the numerical costs are comparatively high.

Thus, the model by Buehler et al. is selected as the system response modeling technique.

6.2.2. Model Data Acquisition

With the model by Buehler et al. determined to be the most suitable model for a fast surge feedback methodology, its defining parameters and characteristics can be derived. Referring to equation 6.7, the model necessitates three geometric scalar values and two throttle characteristics. Thus, assumptions must be made to simplify the HGTR geometry into appropriate scalar values, while the throttle characteristics need to be experimentally obtained.

Inlet Pipe Reduced Modelling
The HGTR inlet pipe geometry varies along its path and hence must be simplified to allow a correct representation in the model. Thus, four hypotheses are formulated from which the model's pipe length is derived:

1. *Incompressibility of the Fluid*: The fluid is considered incompressible. Hence, a surge cycle (reversal of the flow) immediately affects the entire inlet piping, leading to the conclusion that the overall enclosed volume must remain constant.

2. *Inlet Throttle Representation*: The inlet throttle represents all pressure losses in the pipe, measured between ambient and directly in front of the compressor. It is not possible to determine each component's contribution. However, it is assumed that the main contributors are the air filter and mass flow meter, while the pipe and elbows have negligible influences. Thus, no modifications are required to adapt the original model for multiple inlet throttles at different positions.

3. *Modeling and Measurement Restriction*: As a direct result of the modeling and measurement constraints, the compressor only perceives the final pipe diameter.

4. *Inlet Pipe Eigenfrequencies*: Although surge is a system phenomenon and can be triggered by acoustic interferences, the inlet pipe eigenfrequencies due to bends are not surge drivers. This is supported by comparing the typical mild surge ranges with the expected pipe section eigenfrequencies.

All four hypotheses lead to the following equation to calculate the dominant inlet piping length:

$$L = \frac{\sum V_i}{A_{inlet}} \tag{6.8}$$

This equation provides a characteristic length that is approximately 1.8 times larger than the geometric length. Nevertheless, a numerical study confirmed its superior accuracy. It is also important to note that the characteristic length is based on physical assumptions rather than a shooting method, as is often used in B-parameter estimations. Therefore, it does not introduce the typical uncertainties associated with a true tuning parameter.

Inlet Throttle Characterization

One of the key features of the model is the integration of the system's inlet throttling. The characterization of the throttle curve is relatively straightforward, as the throttle is a geometrically constant component with an almost quadratic characteristic. To calculate the polynomial constants, a series of 10 compressors was measured, and the difference between $p_{ambient}$ and p_1 calculated. A quadratic regression yielded a CoP value of 99.8, indicating a very good approximation. A manual adjustment in the quadratic equation ensures zero pressure loss at zero mass flow, accounting for measurement inaccuracies.[19]

Outlet Throttle Characterization

As the outlet throttle is used to define the compressor operating point, its characteristic is not constant but dependent on the throttle's variable cross-section. This inevitably leads

[19] The adjustment (shift in the ordinate direction) is less than 0.5% of the measured value and is therefore within the overall measurement accuracy as defined in the SAE Test Stand Code [87].

to modeling challenges.

Firstly, for very small cross-sections, the throttle throughflow will be dominated by highly turbulent flows. Consequently, the throttle characteristic does not follow a quadratic regression, and divergence will occur at zero mass flow.
Additionally, the design space is well-sampled for areas of high efficiency but not for areas close to surge.
Finally, the regression model of the throttle must respond very quickly to queries, as it will be called by the 1D code multiple times for a single speed line. Therefore, it should be of a low-order type.

To overcome the design space limitation, a turbocharger for medium-duty applications is added to the design set (see Figure 6.16). Its efficiency parabola loosely follows the surge line of typical heavy-duty compressors and significantly widens the throttle valve support point area.

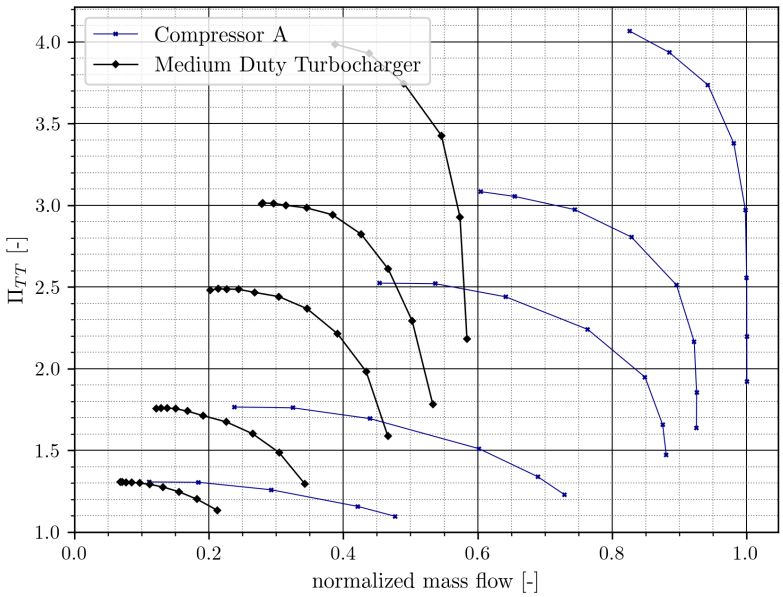


Figure 6.16.: data samples for outlet throttle characterization

After evaluating different regression models, a quadratic regression model with linear coupling terms between mass flow rate and throttle cross-section was selected. An evaluation of the model's response at low mass flow rates shows the expected divergence and source of the main error. However, the affected areas lie below technically relevant compressor speeds ($< 0.5 n_{max}$) or far to the left of even surge-optimized geometries (< 50% of surge mass flow). Hence, the approximation error will not play a significant role. The accuracy in the critical area is comparable to more sophisticated models like Kriging, and the analytical equation allows direct implementation of its derivative in the code, leading to significant computational benefits. The CoP value of the regression model is 98.9%.

6.2.3. Comparison of Measurements with Surge Calculations

With the model being integrated and connected with the compressor map surrogate models, its accuracy for surge calculation is determined.

First, the eigenfrequency f of the model is calculated based on the characteristic polynomial, see eqn. 6.10 [54].

$$\omega = \left(\frac{A_c a_3^2}{LV} \frac{g_1 + g_2 - c}{g_2} \right)^{0.5} \tag{6.9}$$

$$f = \frac{\omega}{2\pi} \tag{6.10}$$

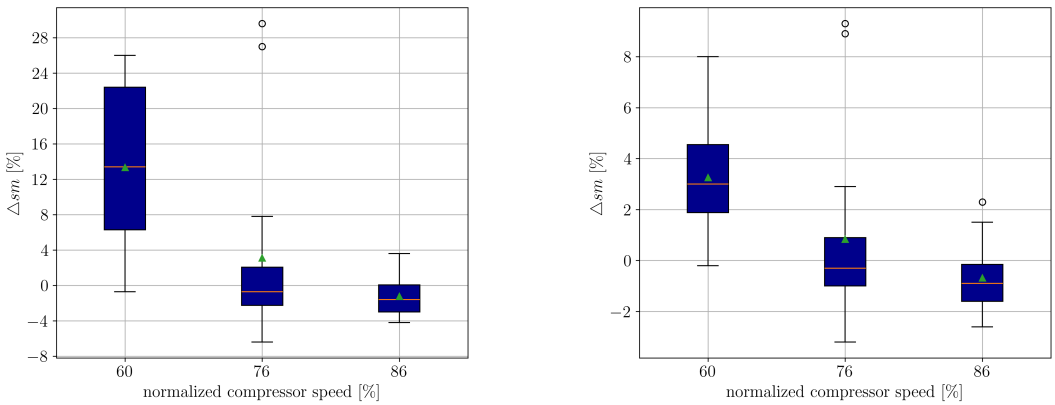
The difference between the predicted and measured mild surge frequency is less than 10 Hz, which is a good approximation considering the simplicity of the model. The original publication [54] demonstrated an even better fit (<2 Hz), but the inlet piping did not require any simplification. It can thus be concluded that the model is capable of sufficiently modeling the eigenfrequency, with the error being attributed to the simplified inlet pipe.

Next, all available surge measurements from the test bench are compared to the calculated values. The required speed lines are provided by the compressor model developed in section 6.1.

To facilitate comparison between different speeds and compressors, the results are normalized using the measured choke mass flow and surge mass flow, as presented in Figure 6.17. Both normalizations are necessary because the surge mass flow varies for each compressor and speed line, leading to significant deviations. However, it provides crucial information about the expected deviation of the model for a compressor at a specific speed. Conversely, the choke-normalized plots enable the comparison of model accuracy across different speed lines. Positive values indicate a lower surge mass flow rate measured at the HGTR, while negative values indicate a higher surge mass flow rate, which is less desirable.

The lowest and highest speed lines of the compressor map are excluded due to the model's boundaries: the lowest speed line is close to the outlet throttle's model uncertainties, as discussed in the previous subsection, and the highest speed line is not well captured by the compressor map surrogate model due to the temperature limitations of the HGTR. Thus, only the three intermediate speed lines of the compressor map are evaluated, which is sufficient for all technical evaluations of surge in heavy-duty applications.

In the surge mass flow rate normalized plot, the 60% speed data shows a large scatter and a positive shift (i.e., a shift of the surge line towards the right). Although this is partially due to the small normalizing values, the same trend is observed in the choke-



(a) $\triangle sm$ - normalized w. surge margin

(b) $\triangle sm$ - normalized w. choke

Figure 6.17.: measured vs. calculated surge mass flow

normalized data, which negates this error source. As the compressor model is most accurate in this region, it indicates a systematic error in the system model, especially since the mean values and medians are comparable in both plots, highlighting no significant outliers.

The systematic under-prediction of the surge line is due to the model's and test bench's inability to distinguish between *stall* and *surge*. At low speeds, the compressors develop some form of stall prior to surge. This is indicated by an increase in the temperature at the compressor inlet, which was, for example, experimentally measured with compressor B at the electric rig. However, although instability or even backflow arises, compressors can operate in a "steady" manner when pressure ratios are sufficiently low [22]. Since the surge detection algorithm of the HGTR ignores sufficiently low amplitude, high-frequency oscillations and the model unable to differentiate between stall and surge, the shift in the surge line can be attributed to this effect. As this speed line is not as relevant for technical evaluation and including the time-dependent response of the compressor in the model would substantially increase calculation time, no adaptation of the model is performed.

The scatter and accuracy improve significantly for the 76% and 86% speed lines of the compressor. Both medians are comparable, but the 76% speed line shows two significant outliers, which correspond to two different, yet very similar compressors. Both compressors exhibit a very flat compressor characteristic. Upon evaluation, the outliers occur due to the onset of instability just below the test bench's surge detection thresholds, somewhat similar to the discussion of the compressor B stall behavior at the HGTR in section 6.1.

The smallest scatter and best calculation results are observed for the 86% speed line. At this speed, sufficient pressure is built up so that a stall event almost immediately leads to deep surge at the test bench. Thus, the binary instability signal of HGTR and model align very well. Importantly, this speed is also the most relevant speed for surge in engine-like

environments.

It is interesting to see how the accuracy of the model closely aligns with the different surge behaviors. For the lowest speed line, surge is underpredicted due to stall effects. At the 76% speed line, deep surge is easily detectable and always occurs; however, stall can still occur prior to this event, leading to a larger scatter. For the 86% speed line, deep surge is triggered almost immediately, resulting in the smallest scatter. However, due to this, the compressor cannot handle randomly occurring disturbances as they happen on the test rig during testing. Thus, the model estimates a slightly better surge mass flow rate than actually measured.

6.2.4. Summary

In this section, different 1D system models were reviewed. Focus was laid on the physical assumptions, numerical stability and cost. It was found that a simplified Greitzer approach presented by Buehler et al. [54] is most suitable due to its low numerical cost and high accuracy according to literature.

In the next step, the HGTR environment was modeled following this approach. Inlet and outlet throttle characteristics were experimentally acquired and implemented into the code as second order polynomial models.

Finally, the system model was validated by comparing calculated data with measured data. The surrogate models derived in section 6.1 served as input data. It was found that large deviations occur for the 60% speed lines, which could be linked to the onset of stall, not detectable by the HGTR nor the model. The accuracy improved with increasing speed, aligning well with the diminishing occurrence of stall and immediate occurence of deep surge.

For the most relevant surge point, the average mean deviation between measured and calculated surge mass flow was found to be -1.8%, with all samples within ± 4%. This result is remarkably accurate given the reduced-order nature of the model and is within the range of other work [124]. Thus, it is concluded that the system model is accurate, fast, and robust enough to be utilized in automated optimization processes.

6.3. Surge Feedback for Surrogate-Model-Based Compressor Design Approaches

In this section, the surge feedback process for automated surrogate-model-based compressor design approaches is described. The feedback process combines the compressor component modeling introduced in section 6.1, and the 1D system modeling introduced in section 6.2.

First, the methodology is derived and the optimization strategy introduced. Next, an optimization run is performed and the results are evaluated for thermodynamic and mechanical validity. Prototypes are then manufactured, measured at the HGTR and compared to the manually improved compressor B and its unconstrained optimization start design B*.

6.3.1. Surge Feedback Methodology

Optimization Procedure

The compressor optimization procedure uses the efficiency optimization scheme proposed by Abel [7], but incorporates a surge feedback loop, as illustrated in Fig. 6.18. The methodology comprises the following steps:

1. An evolutionary algorithm generates a parameter set, which includes the geometric parameters of the compressor and the critical turbocharger speed at which surge is to be evaluated.

2. The geometric parameters are transferred to the CFD surrogate model solver. This solver encompasses multiple CFD-based surrogate models that predict the compressor geometry's partial and full load performance, as well as choke mass flow.

3. The design is also forwarded to the compressor performance map models from section 6.1. A compressor performance curve is estimated for each design.

4. The compressor performance curve is input into the surge prediction model, as introduced in section 6.2, to determine its surge point at the HGTR.

5. All thermodynamic characteristics are relayed back to the optimization algorithm, which evaluates the response and generates new design sets until convergence is achieved. A post-processor facilitates the analysis of the results.

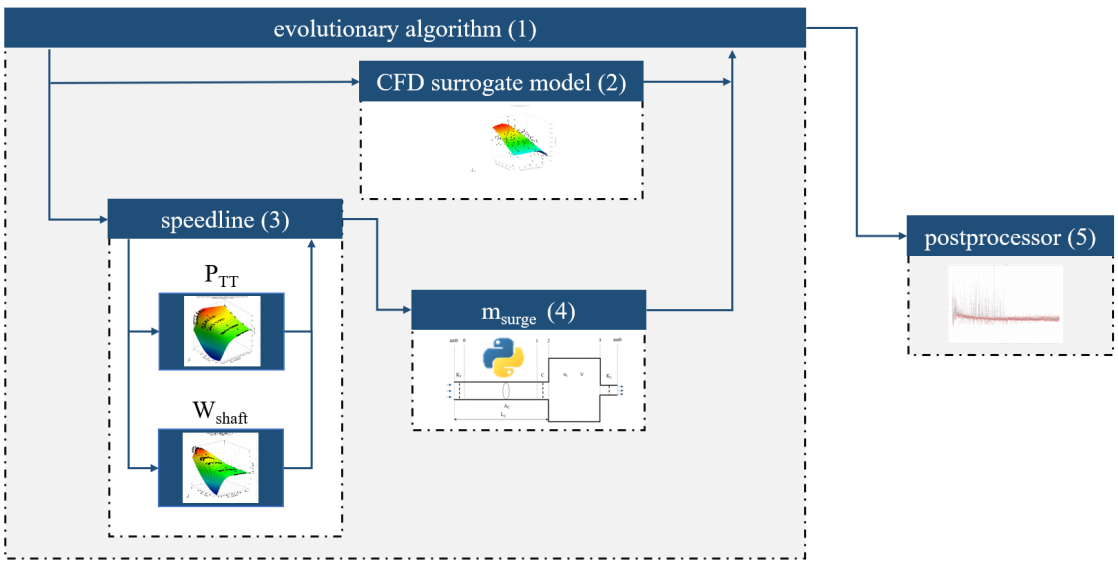


Figure 6.18.: surge constraint compressor optimization scheme

Optimization Objective and Constraints

Setting the appropriate optimization objectives and constraints is particularly important in this optimization setup, as it encompasses all areas of the map, including the conflicting requirements surge, choke, and efficiency at full and partial load operating points. To enable a robust comparison and competition between designs during the optimization process, the objectives and constraints defined in Table 6.1 are utilized.

parameter	handling
full load efficiency	weighted objective
partial load efficiency	weighted objective
full load pressure ratio	constraint
partial load pressure ratio	constraint
choke	constraint
surge	constraint

Table 6.1.: optimization objectives and constraints

The driving factor in turbocharger compressor development is the enhancement of efficiency in engine-relevant areas, which defines the global optimization target. As demonstrated by Abel [7], load collectives from real-world driving cycles of class 8 vehicles can be simplified to a full load and a partial load point. These points represent where the majority of fuel consumption occurs and, consequently, where the optimization potential is highest. The pressure ratios at these points are treated as constraints, as they are dictated by engine requirements. This narrows the main focus to two efficiency values. However, with precise knowledge of the real-world scenario, the multi-objective optimization can be simplified to a single-objective optimization by applying weighting factors, as shown in equation 6.11.

$$\eta_{weighted} = x_1\, \eta_{fullload} + x_2\, \eta_{partialload} \quad x_1, x_2 \in [0,1] \wedge x_1 + x_2 = 1 \tag{6.11}$$

The choke mass flow rate is a requirement of the engine brake and not driver of a new compressor development. Thus, it is handled as a constraint.

The surge margin could theoretically serve as an optimization objective, as a more surge-resilient compressor can enhance engine performance and enable alternative engine control strategies. However, theoretical considerations in engine development and optimization strategies necessitate the definition of a *surge constraint*:

1. The engine control and combustion cycle strategy is established during the early design phase, providing a fixed surge margin. Subsequent improvements in surge margin, although theoretically advantageous, are likely not usable in later design phases due to the significant modifications required in other components. Thus, a surge-optimized geometry may result in reduced overal engine efficiency.

2. Incorporating a surge optimization objective can destabilize the mathematical solver. The compressor performance model, being hardware-based, cannot encompass the same design space as a CFD-based model, necessitating some degree of extrapola-

tion. This can lead to designs that are either unrealistically good or bad. If surge margin were an objective, the optimizer might converge on poorly sampled design space regions. Conversely, a set of constraints can filter out evidently incorrect predictions, imposing penalties on the optimization algorithm without actively rewarding exploration of critical areas. Preliminary test runs confirmed this improved handling of failed geometries.

All constraints are set in such a way that a valid design must achieve the same, or better performance as the manually optimized compressor B, excluded from the surrogate models database.

Design Space

It is important to note that no geometric constraints are imposed. Instead, the geometric parameters listed in Table 6.2 are treated as independent optimization variables. Figure 6.19 illustrates the resulting CFD domains for the upper and lower limit designs.

parameter	reference	upper limit	lower limit
shroud inlet radius	100%	110%	90%
shroud inlet blade angle	100%	119%	74.6%
shroud outlet blade angle	100%	133%	66.7%
diffuser width	100%	130%	80%
diffuser outlet radius	100%	109%	80%
diffuser outlet angle[20]	100%	83.3%	133%
impeller outlet radius	100%	103%	100%

Table 6.2.: specification of the design space

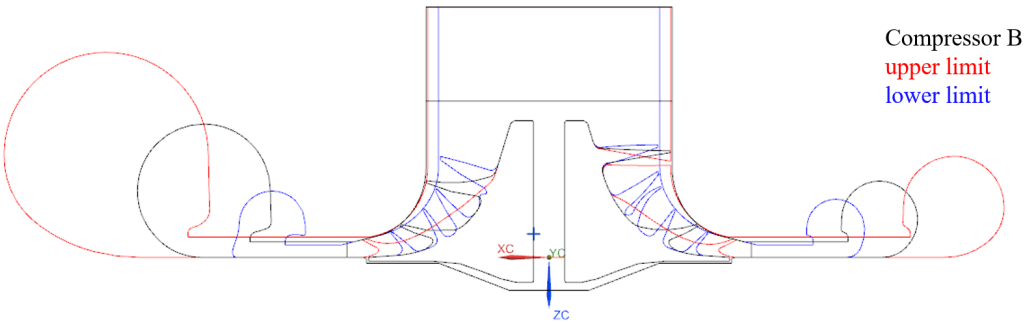


Figure 6.19.: CFD domains for the upper and lower limit case of the design space

6.3.2. Optimization Convergence

The methodology was implemented in Ansys optiSLang and required six hours on a personal computer to achieve convergence. A total of 1950 geometries were generated, of which 767 were duplicates. The convergence history (excluding duplicates) for the parameters, constraints, and objective is depicted in Figures 6.20 and 6.21. The impeller outlet radius is excluded from the analysis as a late turbine matching requirement limited it to the baseline value.

[20] The diffuser outlet angle represents the COPAX analogue to the conventional A/R-ratio. COPAX is a proprietary, parameterized modelling framework for automatic generation of compressor housing CAD geometries. [7]

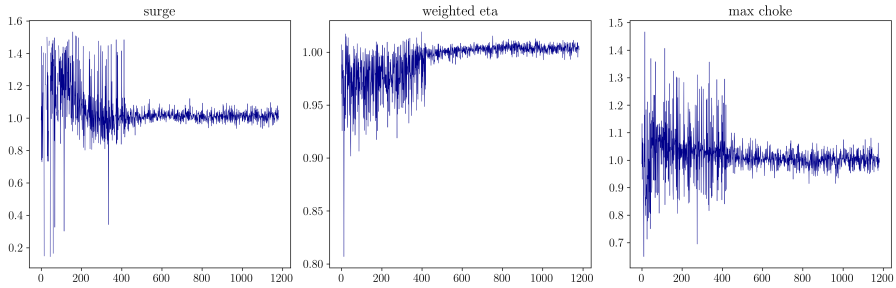


Figure 6.20.: Surge constraint optimization convergence -constraints and objectives. Data normalized with compressor B reference values.

From Figure 6.20, it is evident that the surge constraint significantly influences the numerical cost. During the initial sampling phase, there is a large fluctuation, with results ranging from unrealistically good to unusable geometries. This fluctuation is due to the relatively small design space of the surge model compared to the CFD models, which have thousands of well-distributed data points. Thus, the optimizer must navigate numerous steep gradients and failed designs.

All geometric parameters, except for the diffuser outlet radius, converge to values well within the design space. The diffuser outlet radius, however, converges to its upper limit. This is reasonable, as the diffuser allows for a more controlled expansion than the volute, thereby enhancing efficiency. However, when combined with a relatively large diffuser width, this raises concerns about surge stability.

Both parameters have a very limited effect on the total-total pressure ratio [12], as also seen by the very low CoP matrix value of the pressure ratio surrogate model. This makes the detection of diffuser stall more challenging, as stall is identified based on the shape of the compressor curve.

Although extensive literature on diffuser stall exists, there is no clear consensus, as Hunziker [129] and Casey and Robinson [12] point out. Some studies report surge margin improvements for large diffuser width- to length ratios b/d, while others report the opposite. For well-designed compressors, Casey and Robinson [12] recommend that the diffuser inflow angle should not exceed 65° at the design point, as this should allow stable operation up to 50% of the design mass flow rate. This constraint has been applied in an optimization study for compressors of similar size and application [74] and is thus considered a more reliable parameter for evaluating diffuser stall. Consequently, this criterion is used in the evaluation of the target designs.

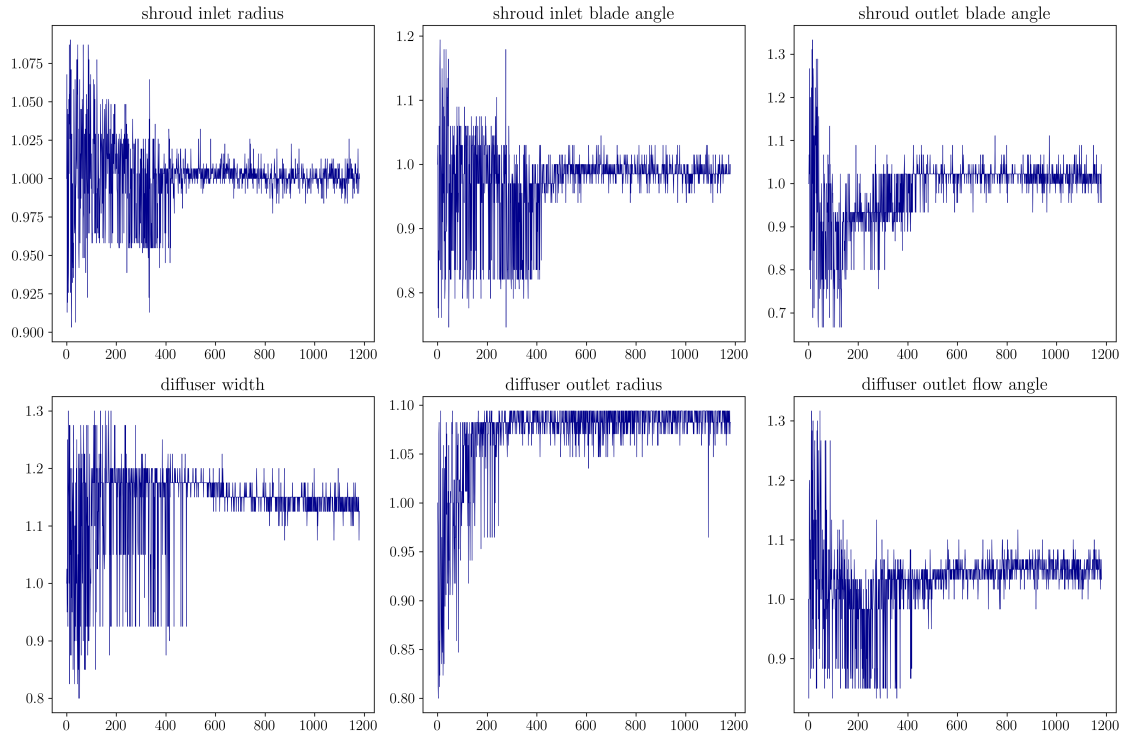


Figure 6.21.: Surge constraint optimization convergence - parameters. Data normalized according to the reference values listed in Table 6.2.

6.3.3. Design Selection

Based on the resulting 3D Pareto front, a design selection for geometry G1849 and G675 is made. The Pareto front and its projection onto the three corresponding 2D planes (normalized with compressor B) can be seen in Figure 6.22.

G1849 shows significant improvements in surge (+2.6% compared to compressor B) and efficiency (+0.9% absolute), while missing the target choke mass flow rate by -1.1%. [21]

G675 fulfills all constraints, while showing a slight efficiency improvement (+0.2% absolute) and surge margin (0.2% compared to compressor B).

It is noteworthy that the surge model is outside the design space for G1849 and at its limits for G675. Therefore, the selected geometries not only provide insights into the surge prediction capability but also indicate whether trends towards new design space areas can be identified. The geometries and parameter sets are illustrated in Figure 6.23 and detailed in Table 6.3.

To address the uncertainty of diffuser stall, RANS simulations were conducted at the design point and the flow angle at the impeller outlet was calculated prior to manufactur-

[21] Given the efficiency and surge improvements and the fact that the splitter blades are likely not well matched, compare Chapter 4, it was decided to use this geometry although it violated the choke constraint. A RANS analysis with adapted splitter blades later confirmed choke mass flow increase, fulfilling the constraint.

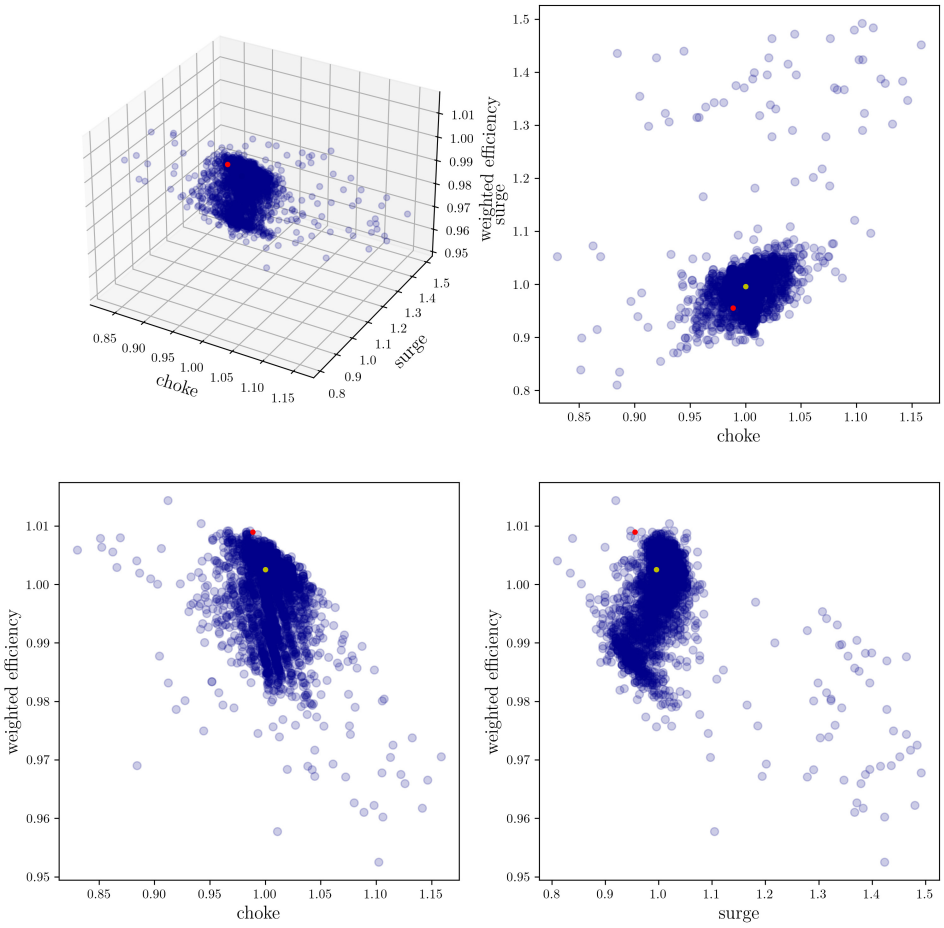
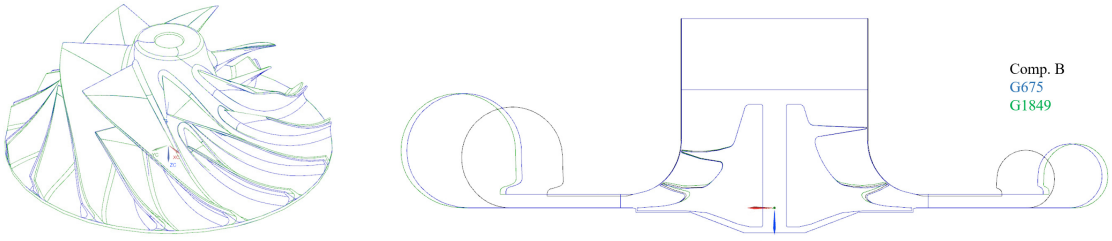


Figure 6.22.: 3D Pareto front and 2D projections. Red: G1849, yellow: G675



(a) impellers G1849, G675

(b) cross-section fluid volume G1849, G675, Comp. B

Figure 6.23.: comparison of compressor B, G1849 and G675

ing the geometries. For geometry G1849, the flow angle is -1.2° below the 65° threshold. In contrast, geometry G675 has a flow angle of 65.5°, slightly exceeding the threshold. Both values are higher than the baseline of 63°, indicating a more critical diffuser and hence higher chance of surge.

parameter	G1849	G675
shroud inlet radius	100%	100%
shroud inlet blade angle	101.5%	101.5%
shroud outlet blade angle	92%	68%
diffuser width	115%	115%
diffuser outlet radius	109%	107%
diffuser outlet angle	105%	103.3%
impeller outlet radius	100%	100%

Table 6.3.: geometry parameters G1849, G675

6.3.4. FEA Evaluation

Due to the higher backsweep of the impeller blades compared to compressor B, mechanical stresses increase [12]. Thus, a FEA was conducted following the methodology outlined by [74] for the G1849 impeller, which represents the most critical design case. The results are shown in Figures 6.24 and 6.25.

Figure 6.24 shows the principal stress distribution at maximum rotational speed, representing the most demanding mechanical load case. The stress levels remain within acceptable limits for thermodynamic testing. Increased stresses are observed at the suction-side main blade fillets but remain within the material's fatigue endurance range. If necessary, increasing the fillet radius could further reduce stress concentrations with minimal influence on aerodynamic performance, thereby enhancing fatigue resistance.[22] The highest stress concentrations occur at the bore hole; however, these are mitigated by a special surface treatment and are not considered critical.

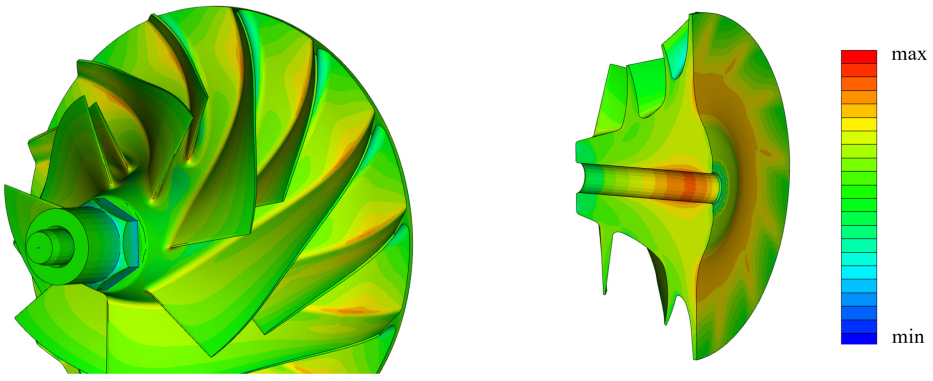


Figure 6.24.: principal stresses of G1849 at maximum speed

Additionally, a modal analysis was conducted to investigate the vibrational characteristics of the impeller. The Campbell diagram (Figure 6.25) shows the lowest and most critical eigenfrequency plotted against the excitation harmonics. The impeller is free of 5th-order excitation and intersects the 6th harmonic only at speeds exceeding 110,000 rpm. This indicates that the design is effectively resonance-free and even outperforms

[22] Aluminum, as a face-centered cubic metal, is not fatigue-resistant and fails over time under cyclic loading. In this context, 'fatigue-resistant' refers to the ability to withstand repeated stress cycles without failure over a period longer than the expected lifetime of the engine.

compressor B in this regard.

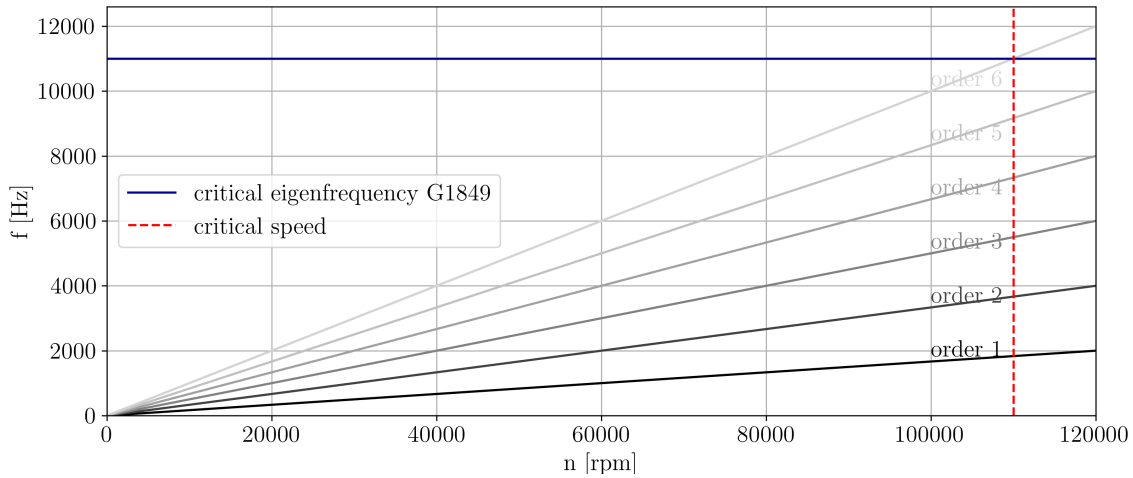


Figure 6.25.: Campbell diagram of G1849

The FEA results confirm that the geometric changes do not violate the mechanical constraints. The impeller can be tested at the HGTR without requiring geometric adjustments. Even for endurance testing, only minor modifications, expected to have negligible thermodynamic impact, are necessary. Therefore, the new designs are deemed valid, and further thermodynamic evaluation at the HGTR can be conducted.

6.3.5. Measurements at the HGTR: Optimization Outcome

All measurements were sequentially conducted using the same base turbocharger to minimize measurement errors. Before the thermodynamic measurements, the impellers were optically measured to ensure they meet the specified tolerances. The false color comparison to the CAD geometries is provided in annex C.

The thermodynamic results can be seen in Figures 6.26, 6.28, 6.27, and 6.29. The mass flow rate is normalized with the design choke mass flow rate, whereas the efficiency comparison shows the absolute (non-normalized) efficiency deviation to compressor B.

First, the map width is evaluated, compare Fig. 6.26, 6.28. Table 6.4 provides the relevant parameters.

Geometry G1849 exhibits the best absolute surge margin at 86% speed, followed by G675, aligning with the predicted trend by the optimizer. It is noteworthy how the prediction accuracy $\triangle sm$ varies among the three geometries. While compressor B and G675 fall within the surge model design space, G1849 required geometric extrapolation beyond the sampled design space. Consequently, G675 and compressor B are within the expected surge deviation (see Figure 6.17), whereas G1849 lies outside this range. Nevertheless,

the prediction accuracy remains comparable to other models' regression capabilities [124].

Given the intentional alteration of the maximum choke mass flow for G1849, a direct comparison of the surge points would yield misleading conclusions. Instead, the map widths normalized by the corresponding design choke mass flow are used. From Table 6.4, it is evident that the map width improved for both optimized geometries at the 86% speed case, as well as for the design map width, defined as the difference between the maximum choke mass flow and the 86% surge point. However, due to the larger surge prediction error and smaller design choke mass flow of G1849, G675 exhibits the best map width. Nevertheless, the optimization run successfully demonstrated that the surge boundary constraint leads to superior map width results compared to manually surge-optimized geometries such as compressor B.

variant	HGTR surge @ 86% speed	HGTR choke @ 86% speed	HGTR choke max speed	HGTR map width @ 86% speed	HGTR design map width	Prediction design map width	$\triangle sm$ [%]
G1849	0.569	0.916	0.984	0.378	0.421	0.455	-5.4
G675	0.572	0.929	0.997	0.384	0.426	0.44	-1.9
Comp. B	0.588	0.932	1.002	0.369	0.414	-	-4

Table 6.4.: map width defining points - optimization results

Next, the efficiency improvements or deteriorations are assessed. For geometry G1849, Figure 6.27 clearly demonstrates that the optimization was highly successful, with significant efficiency gains across the compressor map, except for the anticipated, and fuel-consumption-irrelevant, deterioration at choke.

Similarly, geometry G675 exhibits improvements up to pressure ratios of 3, beyond which the baseline compressor outperforms it. However, the partial and main operating points of the engine, which are the optimization targets, fall within the improved area. It is also noteworthy that the improvement again spans a large portion of the compressor map, proofing that the improvement is not merely a shift of the efficiency parabola closer to the design points. This further underscores the success of the optimization run.

Thus, it can be concluded that the optimization run, set to outperform the manually optimized compressor B, proved to be highly successful. Both designs demonstrate significant improvements in efficiency while maintaining, and even enhancing, the design map width.

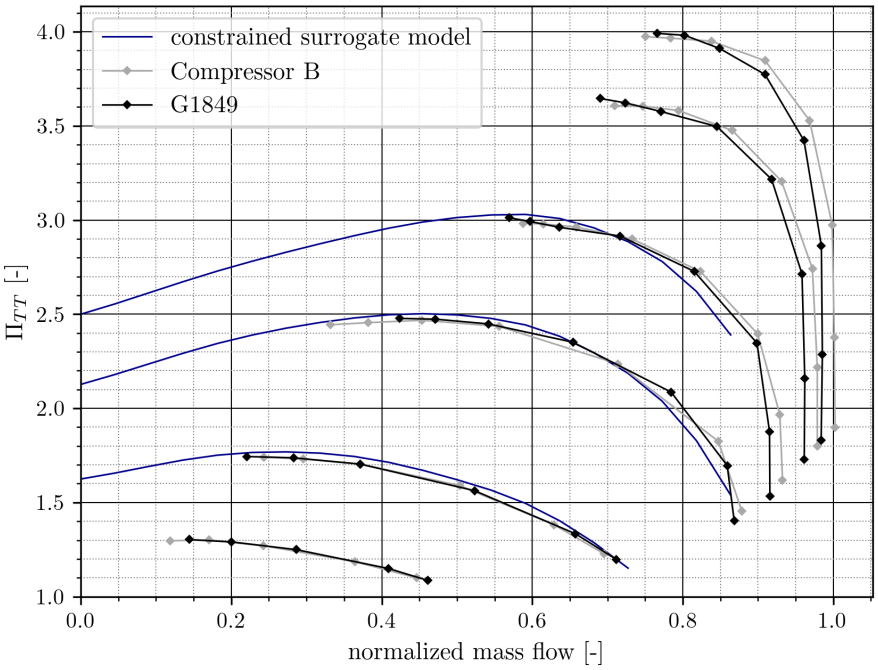


Figure 6.26.: compressor map G1849

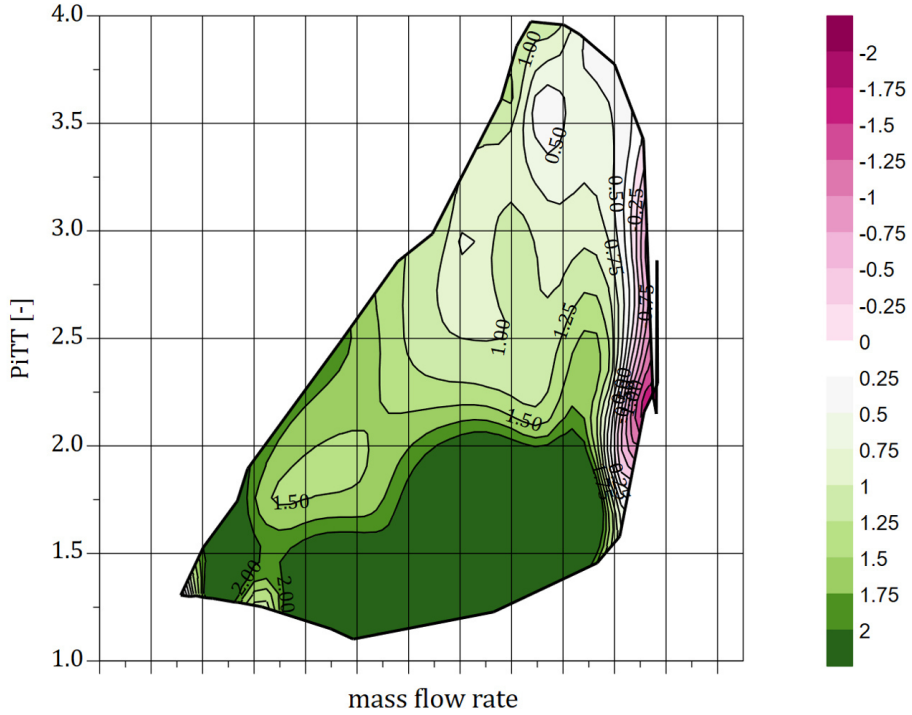


Figure 6.27.: difference map: G1849 - compressor B

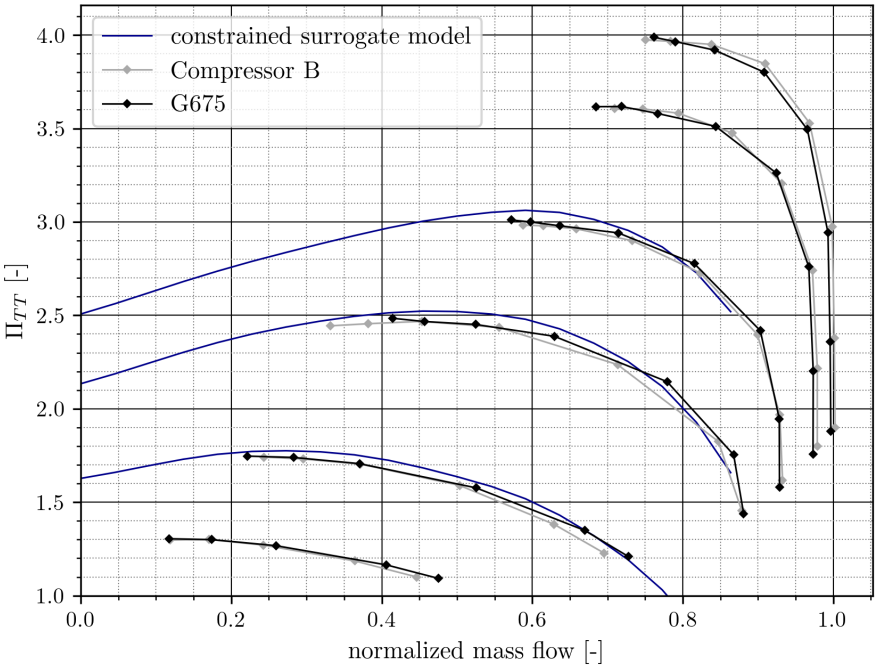


Figure 6.28.: compressor map G675

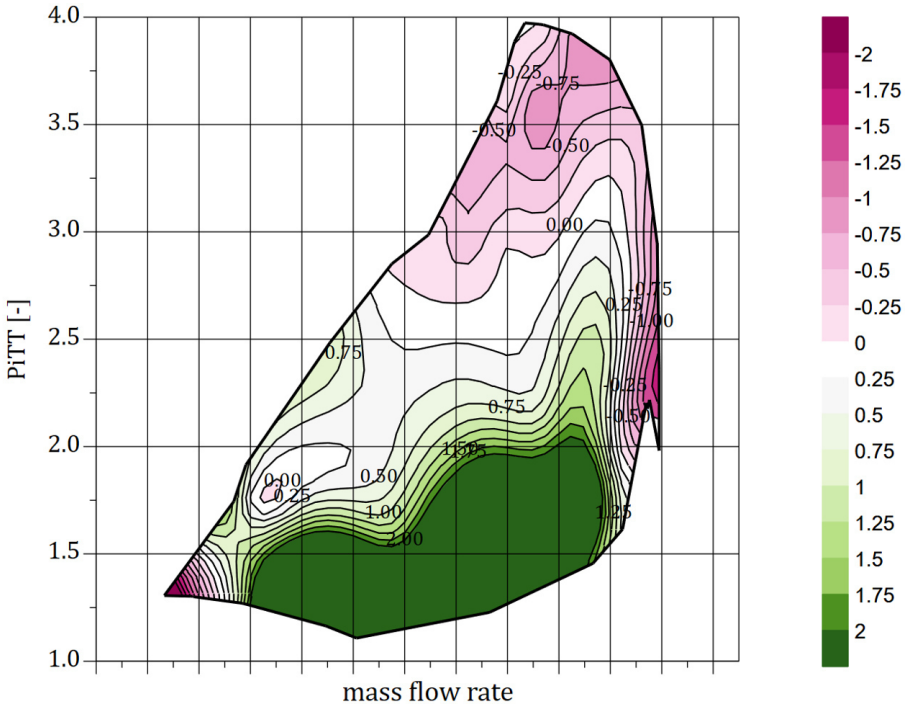


Figure 6.29.: difference map: G675 - compressor B

6.3.6. Comparison with an Unconstrained Optimization Run

Although the optimization run successfully achieved its target, the comparative effectiveness of the proposed method relative to its unconstrained counterpart requires further evaluation. Therefore, the HGTR data for geometries G1849 and G675 are compared against a set of unconstrained optimization designs. The results are illustrated in Figure 6.30. Additionally, the manually optimized design, compressor B, and its unconstrained optimization baseline, compressor B*, are presented for reference.

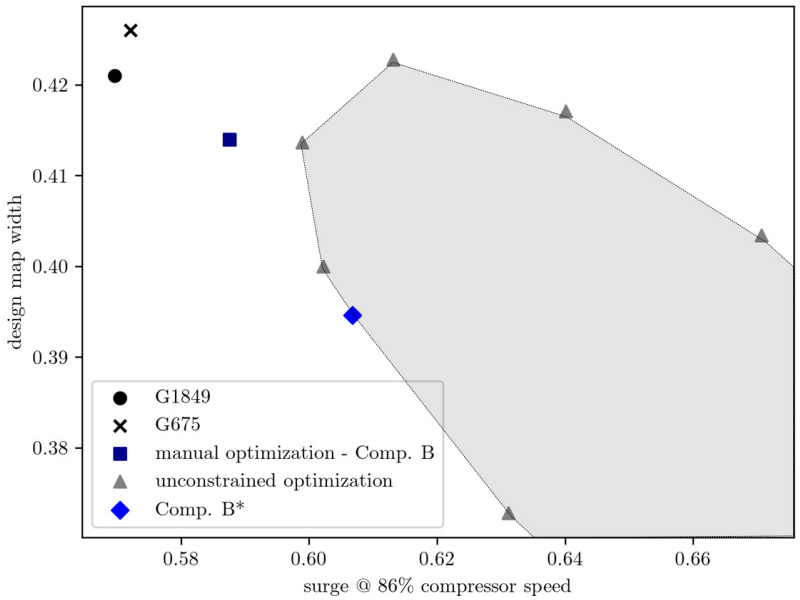


Figure 6.30.: comparison of different design methods

For the unconstrained optimization, only the limit designs are plotted, resulting in an enveloping curve from which clear trends emerge.

No design achieves surge stability for mass flows below 60%. This is particularly critical for applications in engines, where practically no surge margin is available, rendering the resulting designs fairly critical.

An upper limit forms that achieves a wide map width but exhibits high surge mass flows. This is a consequence of the unconstrained optimization. With the choke mass flow set as a constraint, the optimizer includes designs that meet or exceed the choke constraint. Consequently, larger compressors are created, naturally exhibiting a greater design map width. However, in the context of an engine, this is unfavorable as the compressor fails to achieve the required critical surge mass flow rate. Additionally, compressors located close to this edge tend to have lower engine operating point efficiencies.

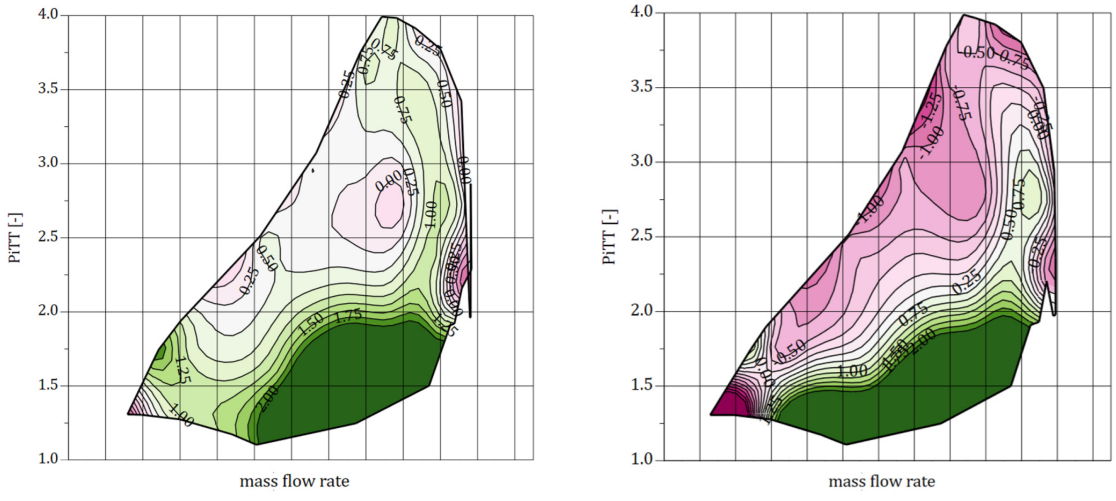
A lower limit forms that exhibits small design map width and lower surge mass flow rates. This limit is also linked to the unconstrained optimization. Generally, a small map width leads to increased efficiency, causing the optimizer to converge towards small map

widths. Additionally, the engine operating points are far to the left in the compressor map, leading the optimizer to shift the compressor's efficiency optimum parabola towards the left as well. This contradicts large choke mass flows, resulting in an increased tendency towards small design map widths.

As a result, compressors with good efficiencies are usually found along this lower edge, such as compressor B*. While the unconstrained optimization design does not provide good map width and surge mass flow rate, a manual optimization leading to compressor B overcame this limitation. However, it also came with a notable drop in efficiency.

The constrained optimization, represented by the two designs G1849 and G675, achieves the greatest design map width at the lowest surge mass flow rate. This is a direct result of the additional map constraint, where the optimizer must fulfill both choke and surge criteria. Consequently, the constrained optimization results in superior designs compared to the unconstrained optimization run.

Most significantly, the proposed method demonstrates the ability to optimize efficiency within a given map width. The manual optimization sacrificed efficiency to achieve map width. The constrained optimization run, however, not only improved the efficiency, map width and surge mass flow rate compared to compressor B but also closed the gap towards the efficiency of unconstrained optimization design compressor B*, as shown in Figure 6.31.



(a) absolute efficiency deviation, G1849 - Comp. B*

(b) absolute efficiency deviation, G675 - Comp. B*

Figure 6.31.: efficiency comparison - G1849, G675, comp. B*

Thus, the surge feedback methodology effectively combines the optimal efficiencies, previously only observed in impractical designs, with the desired map width and surge margin, thereby demonstrating the method's effectiveness. This not only validates the robustness of the proposed approach but also highlights its potential to significantly improve compressor development cycles by automatically achieving a balance between

efficiency and surge stability.

6.3.7. Summary

In this section, an automated, surrogate-model-based optimization procedure was introduced that considers all aspects of a compressor map: choke, surge, efficiency and pressure ratio. An optimization run was performed, yielding designs that, according to model predictions, outperformed the reference compressor B.

Analysis of the resulting geometries revealed comparably large diffusers and diffuser inflow angles, often reported as being more surge critical in literature. Thus, the optimization identified new design sets that would likely not have been considered in a manual design process.

Following verification of mechanical robustness, the designs were manufactured and tested on the HGTR. The measurements confirmed the optimization predictions, with both compressors exhibiting superior performance in terms of surge margin and efficiency relative to the baseline.

A comparison with an unconstrained optimization run showed that the constrained optimization successfully combined high efficiencies with the required map width, effectively ensuring that efficiency gains were not achieved at the expense of surge margin. This stands in contrast to the unconstrained optimization, which failed to produce a single design with an adequate surge margin.

It was also observed that the compressor performance model operated at, or beyond the boundaries of its design space, necessitating extrapolation into unsupported regions. While this led to an increased deviation between prediction and measurement, the prediction remained remarkably accurate and correctly predicted surge margin improvements. This is an important finding as it underscores the model's ability to detect trends and enhances confidence that the compressor performance surrogate model found correct relations between the geometric parameters and performance characteristic.

6.4. Design Space Investigation and Manual Optimization

The design methodology led to two automatically designed compressor geometries that showed significant improvements in surge and efficiency. Yet, it was discovered that the edge of the compressor models geometric design space limited the optimization run due to the increasing prediction error. Hence, further improvement might be possible when manually analyzing the test results.

From Figure 6.26 it is evident that some type of stall happens at high compressor speeds for G1849, although the compressor remains globally stable. This can be seen best for the fourth speed line, where the speed line exhibits more the shape of a cubic, rather than a quadratic polynomial. This is a typical indicator for a stall in the vaneless diffuser [51].

Although the flow is compressible, some basic incompressible considerations of the vaneless diffuser help in identifying the stall-relevant parameters [12].

Mass conservation at in- and outlet of the diffuser leads to:

$$c_{m1} r_1 = c_{m2} r_2 \tag{6.12}$$

For conservation of angular momentum:

$$c_{u1} r_1 = c_{u2} r_2 \tag{6.13}$$

This leads to a flow path that follows a logarithmic spiral:

$$tan\alpha_1 = \frac{c_{u1}}{c_{m1}} = tan\alpha_2 \tag{6.14}$$

With the length of the flow path in the diffuser given by:

$$L = \frac{r_2 - r_1}{cos\alpha_1} \tag{6.15}$$

The (ideal) static pressure recovery coefficient can be determined with:

$$Cp = 1 - \frac{c_2^2}{c_1^2} = 1 - \frac{r_1^2}{r_2^2} \tag{6.16}$$

Considering a diffusers operating condition close to surge, hence low mass flows, c_{m1} reduces significantly, while c_{u1} remains constant. This increases α_1, leading to a substantially longer flow path in the diffuser. While the radial pressure gradient stays the same, the already reduced radial velocity component in the boundary layer is further decelerated due to friction. At some point, the boundary layer detaches and develops a stall.

Based on these considerations, either a decrease in α_1, or decrease in r_2 will provide better stall stability. However, α_1 is a result of the exducer blade angle, diffuser height and mass flow rate. Since the outlet blade angle is already at its technical limit, and the diffuser already being pinched, α_1 is not a feasible parameter.

On the other hand, r_2 can easily be varied as it is an independent geometric parameter. Even more important, r_2 is large for G1849 due to the mathematical optimization procedure. While a large r_2 will lead to better Cp, at some point, the efficiency gain will become negligible. Nevertheless, the mathematical optimizer favors such a design due to its marginally better performance. Thus, the overall impact on efficiency is considered small, while a substantial influence in stall resistance can be expected.

Consequently, r_2 should be reduced. To achieve this, the impeller from G1849 is com-

bined with the compressor housing of G675, as both share the same shroud contour. This configuration results in the design parameters listed in Table 6.5. The slightly smaller volute of G675 is expected to further enhance surge stability. This configuration is referred to as compressor C.

parameter	manual optimization
shroud inlet radius	100%
shroud inlet blade angle	101.5%
shroud outlet blade angle	92%
diffuser width	115%
diffuser outlet radius	107%
diffuser outlet angle	103.3%
impeller outlet radius	100%

Table 6.5.: geometry parameters compressor C

The HGTR results of the new compressor are shown in Figures 6.32 and 6.33. As estimated, the compressor maintains its high efficiency and superiority over compressor B. However, the 86% speedline surge point is significantly shifted towards the left, showcasing a 4.9% improvement over compressor B. Since the compressor chokes in the impeller, the choke mass flow rate remains unchanged.

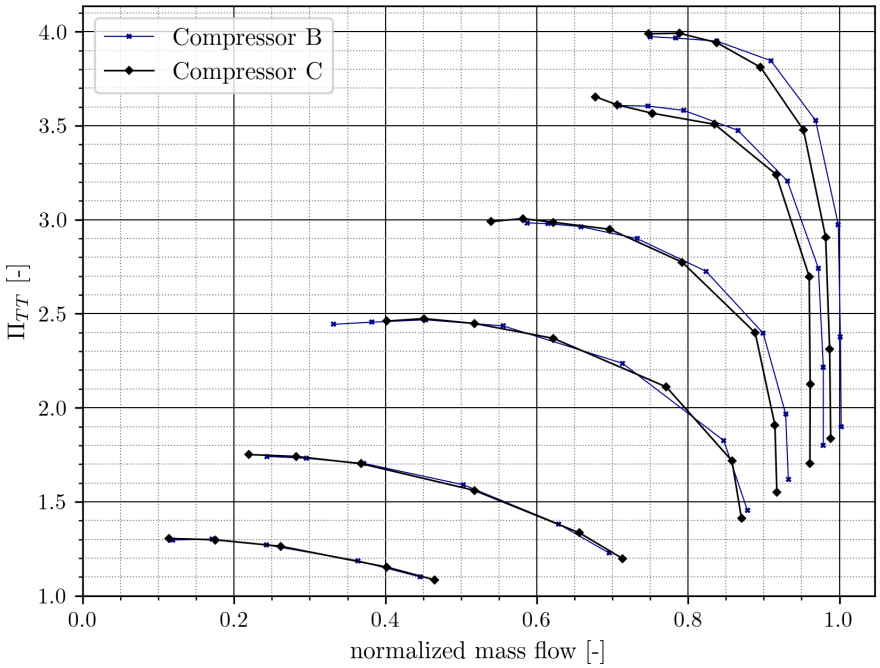


Figure 6.32.: compressor map compressor C

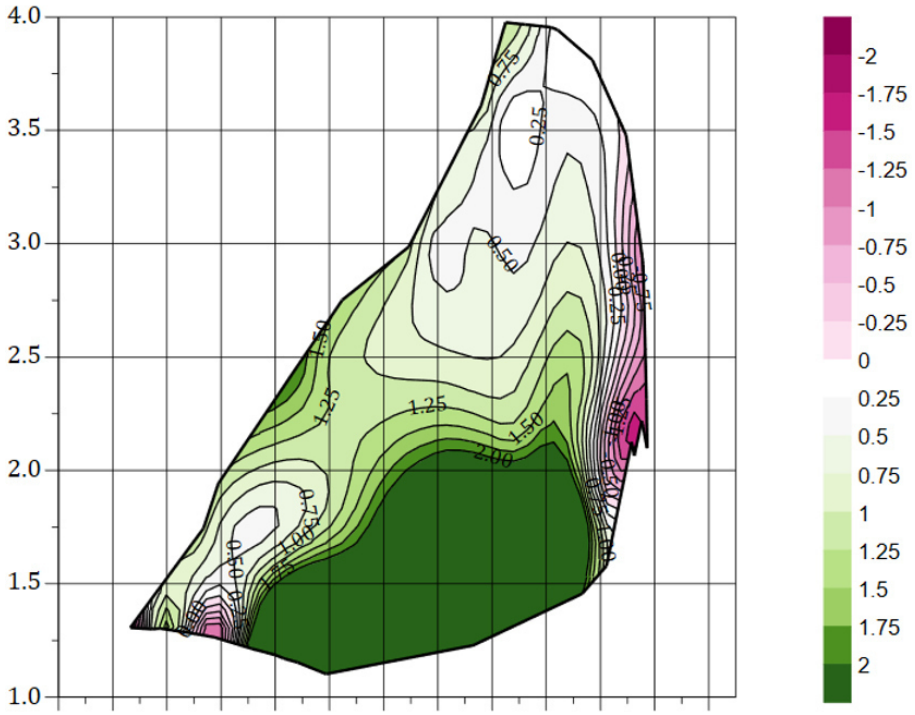


Figure 6.33.: difference map: compressor C - compressor B

The improved map width is showcased in Figure 6.34. The compressor exhibits a 3% surge improvement even compared to G1849, while achieving a design map width of 0.455, representing a 2.9% enhancement over the previously best-performing geometry, G675.

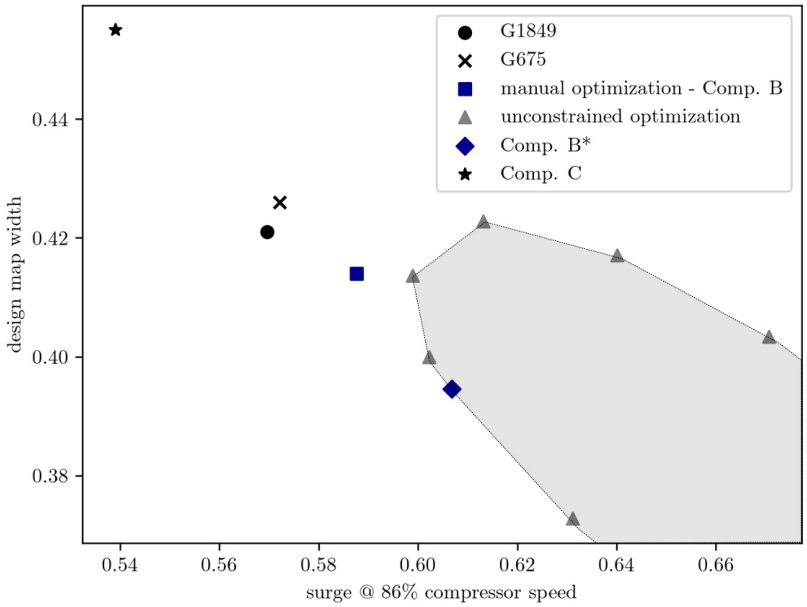


Figure 6.34.: manual optimization improvements

Thus, the manual optimization can be considered highly effective. While the automated process accurately detected trends, it was unable to converge on the optimal parameter combination due to limitations imposed by the design space boundaries and the occuring steep gradients in that region. However, a simple analysis of the automated optimization results correctly identified the diffuser as the surge trigger. By reducing the diffuser outlet radius -along with a corresponding reduction in volute size- surge was significantly delayed, while the compressor retained much of its efficiency advantage over Compressor B.

Importantly, the surge point measured on the HGTR aligns with the model prediction for G1849 within measurement accuracy, confirming that the model previously lacked sufficient data at this design space edge. This lack of data can now be addressed by integrating the three new designs into the model.

6.5. Conclusion

In this chapter, a reduced-order model for predicting compressor performance and a reduced-order model for predicting surge in HGTR environments were introduced. Both models were extensively validated using HGTR and URANS results. The compressor performance surrogate model demonstrated such a high degree of accuracy that, in predictive mode, it enabled the identification and correction of hardware anomalies. With this, the model independently contributes to, and significantly enhances, the compressor

development process.

Upon achieving sufficient accuracy, the models were integrated into an automated compressor optimization process that considers all thermodynamic requirements, including choke, design point efficiencies, pressure ratios, and surge mass flow rate. An optimization run was conducted, and two promising designs were identified. After ensuring mechanical validity and prototype compliance, the geometries were tested at the HGTR.

The measurements showed that, in both cases, the map width was improved compared to the baseline compressor B, which had been manually optimized for greater surge stability. Both designs were close to the predicted surge point showing deviations of -1.9% and -5.4%, respectively. One geometry met all requirements while enhancing efficiency compared to compressor B. The second design significantly improved the efficiency across the entire compressor map, while being slightly, but purposely smaller than the required maximum choke mass flow (-1.6%). Notably, this geometry required the model to extend beyond the known design space, thereby validating and highlighting the compressor model's capabilities even at the edge or beyond its known range.

A comparison with a set of unconstrained optimization designs not only showed the improvement in map width, highlighting a successful efficiency improvement not on cost on surge margin, but also showed a significant diminishing gap in efficiency. The constrained model successfully converged towards new designs to overcome the surge constraint. Thus, new parameter sets were discovered that, on basis of engineering experience, would not have been selected.

Furthermore, a manual analysis of the surge trigger for G1849 was conducted and the diffuser identified as the main driver. A combination of the G1849 impeller with the G675 housing led to a new design that maintained much of the efficiency gain, while significantly improving surge margin, setting a new benchmark. Importantly, this minor change in geometry led to the exact surge value the model predicted for G1849. This confirmed the suspected steep gradient of the surge - geometry relationship in this area, which could not be well captured by the compressor model due to lack of training data. However, the model correctly predicted the trend despite the extrapolation, enabling the discovery of this improved design. The model can now be refined by incorporating these results into its design space.

This demonstrates that surrogate-model-based optimization procedures can be effectively safeguarded against converging towards surge-critical geometries without necessitating overly conservative engineering guidelines. The proposed method proved capable of meeting the demanding development goals, outperforming both manual and unconstrained approaches. With this, compressors can now be better tailored to specific engines, reducing fuel consumption and emissions while at the same time, significantly cutting development time, costs, and testing effort.

7. Summary

This phd thesis aimed to answer the following research question:

Describe and model the main influences relevant to compressor surge at both component and system levels in heavy-duty commercial vehicle applications, so that new optimization potentials for surge and efficiency can be identified and utilized using currently applied design approaches.

This main research question was broken down into four objectives, which were worked on in the previous chapters.

Validation of the URANS Simulation Methodology (Chapter 4)
As outlined in Chapter 3, flow phenomena associated with surge pose significant challenges for CFD. At the same time, there is strong industrial demand for CFD setups that are computationally inexpensive, fast and robust. Thus, the first objective of this work was to investigate the capabilities and limitations of a typical industry-grade URANS setup.

The URANS setup contains the full-annulus compressor, the test rigs' whole downstream piping, and a reduced upstream piping in order to keep numerical effort adequate. The spatial CFD domain is a fully rule-based hybrid grid and employs a high-Re-approach to avoid numerical instabilities and reduce numerical costs. The *realizable* $k-\epsilon$ turbulence model is used based on industrial best practice, experience and comparison with literature.

First, a grid independence study was conducted. The spatial discretization was found to be adequate with approximately 8 million cells,which is in line with other work. The temporal discretization showed a global parameter independence for a 10deg time step, yet it was decided based on a recent study that for detailed flow field analysis, a 1deg time step is required.

Upon ensuring grid independence, investigations were carried out on the electric test rig to obtain detailed transient measurements and enable comparison between test and CFD data. Steady static pressure measurements in the diffuser showed a very good agreement between URANS and experimental result, with maximum deviations of 2.5% at the impeller outlet. Analysis of the pressure field attributed the increased deviation at impeller outlet to the significant radial pressure gradient. In combination with manufacturing tolerances in the positioning of the sensor holes, this was identified as the main cause of the deviations.

Transient pressure measurements were conducted at the onset of surge and compared with the simulation. Analysis of the three pressure transducers showed a very good agreement. In both the simulation and experiment, the pressure signals from the two

diffuser transducers diverged, with the position "diffuser transient" exhibiting a higher pressure. Moreover, once clearly distinguishable oscillation occurred, the phase shift between both transducers was exceptionally well captured, with even slight crossovers of the pressure signals being captured in simulation and experiment.

A more detailed look at the diffuser sensor data revealed that the time from initial disturbance to fully developed stall matches very good, with the simulation requiring 20 rotor revolutions and the test 19 revolutions. Additionally, the amplitude and oscillation frequency during stall inception showed remarkable comparability. Only after the stall was fully developed did the signals exhibit a sudden phase shift, attributed to the now unstable flow field, where any random disturbance from the test rig could grow undamped. This, naturally, could not be captured by the URANS setup.

Also, a comparison with global HGTR data was conducted at engine-relevant speeds. Global data of the surge cycle matched well, leading to the conclusion that the CFD setup is suited for investigating the fluid field near, or during surge. Furthermore, the setup can be employed to validate global performance data from other, less sophisticated modeling approaches.

Investigation of the Surge Mechanism of a High-Performance Compressor and Outline of Potential Optimization (Chapter 4)
With the URANS simulation validated, the surge mechanism of compressor B, equipped with a ported shroud, was investigated.

Initially, a diffuser stall was observed that developed due to the non-axisymmetric pressure distortion induced by the volute. Simultaneously, a flow feature emerged in the compressor inlet and inducer region. It was revealed that this flow feature originated from the ported shroud, which increases its recirculation flow as the compressor's mass flow rate decreases. During recirculation, part of this flow then interacted with the ported shroud ribs, generating jet-like vortical structures reaching into the compressor inlet. As a result, the inlet flow conditions became significantly disturbed.

Eventually, the combination of the sudden adverse pressure gradient from the diffuser stall and the incoming flow disturbance from the ported shroud triggered a rapidly growing exducer stall. This initiated two self-reinforcing feedback loops: the stalled exducer increased recirculation through the ported shroud, as the inducer continued to pump flow; simultaneously, the diffuser stall intensified due to a reduced mass flow caused by the blockage in the exducer, amplifying the pressure distortion. This led to rapid flow breakdown and the onset of deep surge.

With the surge trigger mechanism understood, optimization potential was identified.

The ported shroud can be aerodynamically improved to reduce the jet-like vortical

structures that disturb the flow entering the impeller. Such modifications have been demonstrated in literature, and further optimization depends on mechanical, acoustic, containment, manufacturing and durability constraints.

For the impeller, the splitter blade axial position was found to be a viable optimization parameter, as it does not influence surge inception. Experimental validation confirmed this, enabling automated optimization for improved efficiency and choke performance without compromising surge margin.

For the volute, a redesigned overhang volute acting as a self-regulating recirculation channel was proposed, which reduces losses at low mass flow rates and mitigates circumferential pressure distortion, thereby enhancing both efficiency and stall resistance.

With this, not only compressor B but also the entire compressor family can be improved. This can be achieved by integrating new design features such as a redesigned ported shroud or volute. Additionally, the parameter space of the surrogate-based design approach can be expanded by including the non-surge-critical parameters, offering greater flexibility and hence, lead to new designs with improved performance.

Investigation of Transient Environments and their Consideration in Early Stages of Compressor Development (Chapter 5)
It is well established that steady-state conditions on a HGTR deviate from the transient environment encountered in an ETR or in a vehicle, and that this can significantly alter compressor performance and surge. Despite considerable research effort aimed at understanding pulse interactions, literature remains seemingly contradictory and industry experience often opposes published work. Thus, it was essential to investigate the origin of this discrepancy and determine at which stage of compressor development pulses need to be considered.

To address this, an extensive experimental campaign was conducted to examine typical geometric components in turbocharger compressors and assess the influence of pulse amplitude and frequency. To enable fair comparisons, a surge margin correction scheme was proposed that accounts for the pressure drop under pulsating conditions, thereby allowing the determination of the actual surge margin shift.

The first geometric feature investigated was the in- or exclusion of a ported shroud. Large data testing revealed that compressors equipped with a ported shroud typically exhibit a significant deterioration in surge margin. In contrast, tests using identical compressor hardware without a ported shroud showed improvements in surge margin. This finding is very important for interpreting much of the existing literature and reconciling it with industry experience, as most academic studies have been conducted using compressors without ported shrouds. Hence, findings and observations do not contradict, but are due to fundamentally different setups. Moreover, this finding holds substantial relevance

for industry practice, as ported shrouds are a design feauture added at late design phases. Given the fundamentally different behavior of the compressor, pulse interaction cannot be evaluated at earlier, less cost-intensive phases of development.

The second geometric feature investigated was the diffuser design, with both a vaned and vaneless diffuser tested under increasing pulsation amplitudes. Results showed that this plays a crucial role, as the vaned diffuser design's surge margin deteriorated significantly under increasing pulses, whereas the vaneless diffuser design's surge margin first decreased, but then increased. This behaviour was attributed to the differing stall mechanisms in the compressors. In a vaned diffuser design, stall in one component rapidly triggers stall in the other component, leading to a swift and catastrophic flow breakdown resulting in deep surge. Vaneless diffuser designs, however, can exhibit large "stable" rotating stall areas and have a slow transition to deep surge. This slower progression allows the imprinted pulse to counteract and delay surge. To the author's knowledge, this behaviour has not been previously reported, making it a novel and important finding. It may also help reconcile contradictory literature, particularly in cases where stationary equipment (where vaned diffuser designs are more common) is used.

Furthermore, the influence of pulsation amplitude and frequency was investigated for a compressor featuring a vaneless diffuser and a ported shroud. The experiments showed that even a simple parameter set leads to a highly non-linear surge margin shift behaviour, that is further affected by eigenfrequency interactions within the test rig. Again, this finding helps to bridge the gap between seemingly contradictory results in literature, as even marginal shifts in the setup can lead to vastly different results.

Lastly, the operating conditions of a compressor in an ETR environment were investigated. Transient pressure measurements revealed that, due to the EGR system of the engine, pulses not only vary in amplitude but also undergo a significant shape change. It was further observed that the EGR affects the entire charging system, again contrasting with some literature that focuses on non-EGR systems.

As a result, it was concluded that pulses can only be considered at late design stages, when detailed information about the engine and final compressor geometry is available. Importantly, and, to the best of the authors knowledge, for the first time, a theory based on geometric design features is proposed to explain the many contradictory reports on pulsation effects. Future work is recommended to further investigate this theory and to focus detailed flow field studies on the effect of pulses on compressors equipped with ported shrouds.

Investigation of Surge Feedback for Surrogate-Model Based Design Approaches Without Geometric Constraints (Chapter 6)
With the URANS setup established as a suitable method to validate lower-order approaches and the system-level behaviour thoroughly investigated, the foundation was

laid to explore whether surrogate-model-based optimization can be safeguarded against converging towards more-surge critical designs when maximizing efficiency.

In order to do so, a compressor model was developed that generates a complete compressor map extending down to zero mass flow. This was achieved by utilizing a proprietary set of compressors, with test data linked to geometric parameters through surrogate modeling. To prevent numerical overshoots in the unstable area of the quasi-steady compressor characteristic, the RET was used as a boundary condition, successfully enforcing the characteristic positive slope. The tuning parameter K of the RET was used in an optimization scheme to further increase the surrogate models accuracy in the vicinity of surge.

When comparing the surrogate model's prediction in the unstable area of the map with the limited experimental data available in literature, discrepancies were found in the shape of the characteristic curve. While literature suggests a third-order-polynomial, the model predicted an almost linear pressure drop. Therefore, a coupled model was developed that uses the same surrogate model, but replaces the positive slope region with the analytical Moore-Greitzer polynomial.

URANS simulations of the compressor alone, thereby enabling stable operation within the otherwise unstable regime, showed better agreement with the coupled model than with the constrained model. However, while the coupled model exhibited higher accuracy in the deeply unstable region, it degraded the model's accuracy near the surge line, where reliable experimental data are available. Thus,the constrained model was selected for further use.

In a direct comparison between the model in predictive mode and RANS simulation, the model achieved comparable performance in the numerically stable region. However, the RANS became numerically unstable in the vicinity of surge while the model closely matched the test data. As a result, the model not only outperformed the RANS, but also predicted the speedline within seconds.

The models true predictive capabilities were revealed when, by coincidence, a faulty impeller was tested. This led to a deviation between test and model, on which a geometric measurement was conducted and a reduced tip gap was found. After remanufacturing, a second anomaly was found and linked to the test rig, which had triggered a stall event. A passenger car test bench with less volume and more precise control validated the model's prediction. This is a remarkable finding, as it demonstrates the model's utility not only as a development tool but also as a means of actively monitoring test data to enhance data quality.

In the next step, the compression system was modeled. As established in Chapter 5, pulses cannot be modeled in early stages of development. Therefore, it was decided to model the HGTR environment. The reduced Greitzer model proposed by Buehler et al.

[46] was identified as the most suitable model, and its defining parameters and characteristics were derived accordingly.

An evaluation of the models's accuracy showed that the model is very accurate for high compressor speeds, but looses accuracy at lower speeds. It was revealed that this is due to the models and test rigs inability to distinguish between different types of instabilities. While the model predicts the mathematical onset of instability, the test rig permits a degree of instability before reporting surge. This limitation is not critical at high compressor speeds, where deep surge is triggered almost immediately upon instability onset. However, at lower compressor speeds, minor instabilities occur below the detection threshold of the HGTR. Given that engine-surge critical regions are at high compressor speeds, this behavior was deemed not-critical. Thus, no adaption for the surge feedback was made, although future improvements are recommended.

Finally, the compressor and system models were combined with the optimization framework proposed by Abel et al. [99]. All constraints and objectives were of thermodynamic nature, with no geometric constraints set. The optimization goal was to surpass the performance of the baseline compressor B.

The optimization converged to unconventional geometries characterized by large diffusers and volutes,wich, according to engineering guidelines, suggested a reduced surge margin. Nevertheless, after confirming mechanical integrity, two designs were manufactured and tested on the HGTR.

Both designs outperformed compressor B in terms of surge margin. While G1849 showed significant efficiency improvements across the entire compressor map, it did not meet the choke requirement. In contrast, G675 achieved efficiency gains up to pressure ratio of three while satisfying all imposed constraints. In both cases, the designs exceeded compressor B in the fuel-consumption-relevant weighted efficiency of part and full load. Additionally, both designs exhibited increased map width.

A comparison with an unconstrained design run showed that both designs achieved superior surge margin relative to any of the unconstrained designs, comparable or better map width than the best unconstrained design in this regard, while significantly reducing the efficiency penalty typically associated with compressors designed for large map width.

A surge trigger analysis for G1849 identified the diffuser as the main source of instability. Given that G1849 and G675 share the same shroud contour, the compressor housing of G675 was combined with the impeller of G1849 to form compressor C. This design has a slightly shortened diffuser an minimally reduced volute size. Despite these little changes, compressor C set a global benchmark in surge margin performance, surpassing compressor B by 5% and the best unconstrained design by 6%. Importantly, this improvement came with only a minimal reduction in efficiency compared to G1849.

Since the compressor model was operating out of its design space for G1849, it was hypothesized that prediction accuracy might be compromised. However, it was anticipated that the model would still capture the trend. Compressor C validated this expectation and further highlighted the steep gradient the geometry-surge relationship exhibits in this region. The experimental results can now be incorporated into the surrogate model, expanding the design space in this critical area.

Conclusion

This work successfully addressed all four objectives that were set.

First, it demonstrated that URANS simulations, with emphasis on numerical robustness and high levels of automation, can reliably capture the relevant flow phenomena leading to surge. This finding supports broader application of URANS in compressor development, enabling more frequent use with reduced computational cost and increased confidence.

Second, the surge trigger of a high-performance compressor with ported shroud was derived. Based on its understanding, optimization potential was outlined, including both new design features and new variables in surrogate-model based approaches recommended. These findings enable improvements not only for a specific design but for the entire compressor family.

Third, in a large experimental campaign, influences of pulses and geometric features on surge were investigated. Importantly, it was found that many seemingly contradictory results in literature and industry stem from the in- or exclusion of specific compressor design features. Moreover, it was shown that even in simple setups, the surge shift is highly nonlinear, making generalization across configurations nearly impossible.

Finally, this work demonstrated that surrogate-model based optimization procedures can be constrained purely by thermodynamic criteria. This approach enabled the discovery of superior compressor designs that defy conventional engineering guidelines. In the presented case, a geometry declared invalid by both experience and engineering recommendations achieved a new benchmark in surge margin within its compressor family.

With this, multiple critical gaps in compressor development are addressed. Industry can apply the improvement recommendations and implement surrogate-model-based optimization constrained solely by thermodynamic criteria. Simultaneously, a solid experimental foundation was laid for academia to support future research in transient environments and to enable more targeted investigations into specific effects or compressor types. As a result, this work directly impacts engine fuel consumption, offering significant benefits to both the economy and the environment.

Bibliography

[1] Maria-Esperanza Barrera-Medrano. *The effect of exit pressure pulsation on the performance and stability limit of a turbocharger centrifugal compressor*. Phd thesis, Imperial College London, 2017. doi:10.25560/49451.

[2] Statista. transportvolumen des weltweiten logistikmarktes, 10.12.2024. URL: https://de.statista.com/statistik/daten/studie/870589/umfrage/transportvolumen-des-weltweiten-logistikmarktes/.

[3] DHL Freight. Gueterverkehr statistik weltweit, 10.12.2024. URL: https://dhl-freight-connections.com/de/trends/gueterverkehr-statistik-weltweit-deutschland-europa-und-international/.

[4] Statista. Transport und logistik, 10.12.2024. URL: https://de.statista.com/themen/733/transport-und-logistik/.

[5] Hermann Hiereth and Peter Prenninger. *Charging the Internal Combustion Engine*. Powertrain. Springer-Verlag, Wien, Vienna, 2007. doi:10.1007/978-3-211-47113-5.

[6] Michael Wöhr. *Entwicklung eines variablen Turbolader-Verdichters für schwere Nutzfahrzeugmotoren*. Phd thesis, Technische Universität Dresden, 2016. URL: https://nbn-resolving.org/urn:nbn:de:bsz:14-qucosa-215989.

[7] Matthias Abel. *Optimisation of a Turbocharger Compressor for Heavy-Duty Engines based on Aerodynamic Loss Analysis*. Phd thesis, Imperial College London, 2020. doi:10.25560/83103.

[8] Heiko Lettmann and Karl Maderthaner. *Grundlagen Verbrennungsmotoren: Funktionsweise und alternative Antriebssysteme : Verbrennung, Messtechnik und Simulation*. ATZ/MTZ-Fachbuch. Springer Vieweg, Wiesbaden and Heidelberg, 9., korrigierte edition, 2019.

[9] Jürgen Lehmann, Peter Kozuch, and Kleffel, Jens, Lorenz, L.M. Om471 – der maßgeschneiderte heavy-duty-nutzfahrzeugmotor für den weltweiten einsatz bei daimler trucks. *Wiener Motorensymposium*, 2022.

[10] I. J. Day. Stall, surge and 75 years of research. In *Proceedings of the ASME Turbo Expo 2015: Turbomachinery Technical Conference and Exposition*. ASME, 2015. doi:10.1115/GT2015-44109.

[11] Ronald H. Aungier. *Centrifugal Compressors: A Strategy for Aerodynamic Design and Analysis*. ASME, New York, N.Y, 2000. doi:10.1115/1.800938.

[12] Michael Casey and Chris Robinson. *Radial flow turbocompressors: Design, analysis, and applications*. Cambridge University Press, Cambridge, United Kingdom and New York, NY, USA, 2021.

[13] Teng Cao, Tadashi Kanzaka, Liping Xu, and Tobias Brandvik. Tip leakage flow instability in a centrifugal compressor. In *Proceedings of the ASME Turbo Expo 2019: Turbomachinery Technical Conference and Exposition 2019*. ASME, 2019. doi:10.1115/GT2019-90217.

[14] Bernhard Semlitsch and Mihai Mihaescu. Flow phenomena leading to surge in a centrifugal compressor. *Energy*, 103:572–587, 2016. doi:10.1016/j.energy.2016.03.032.

[15] Nobumichi Fujisawa, Daiki Ema, and Yutaka Ohta. Unsteady behavior of diffuser stall in a centrifugal compressor with vaned diffuser. In *Proceedings of the ASME Turbo Expo 2017: Turbomachinery Technical Conference and Exposition*, volume 2D: Turbomachinery. ASME, 2017. doi:10.1115/GT2017-63400.

[16] M. Hewkin-Smith, G. Pullan, S. D. Grimshaw, E. M. Greitzer, and Z. S. Spakovszky. The role of tip leakage flow in spike-type rotating stall inception. *Journal of Turbomachinery*, 141(6), 2019. doi:10.1115/1.4042250.

[17] Elias Sundström, Bernhard Semlitsch, and Mihai Mihăescu. Generation mechanisms of rotating stall and surge in centrifugal compressors. *Flow, turbulence and combustion*, 100(3):705–719, 2018. doi:10.1007/s10494-017-9877-z.

[18] Franz Durst. *Grundlagen der Strömungsmechanik: Eine Einführung in die Theorie der Strömungen von Fluiden*. Springer, Berlin and Heidelberg, 2006. doi:10.1007/978-3-540-31324-3.

[19] Dominik. Surek and Silke. Stempin. *Angewandte Strömungsmechanik: Für Praxis und Studium*. Springer eBook Collection Computer Science & Engineering. Vieweg+Teubner, Wiesbaden, 2007. doi:10.1007/978-3-8351-9094-8.

[20] Willi Bohl and Wolfgang Elmendorf. *Strömungsmaschinen 1: Aufbau und Wirkungsweise*. Kamprath-Reihe. Vogel Buchverlag, s.l., 11. edition, 2012.

[21] Rüdiger Schwarze. *CFD-Modellierung: Grundlagen und Anwendungen bei Strömungsprozessen*. Springer, Berlin and Heidelberg, 2013. doi:10.1007/978-3-642-24378-3.

[22] David Japikse. *Centrifugal compressor design and performance*. Concepts ETI Inc, Wilder, Vt, 1996.

[23] Hermann Schlichting. *Boundary-Layer Theory*. Springer Berlin Heidelberg, Berlin, Heidelberg, 9th edition, 2016.

[24] Moritz Werner. *Charakterisierung des Verdichterpumpens eines kleinen Abgasturboladers*. Phd thesis, Technische Universität Berlin, 2018. URL: https://depositonce.tu-berlin.de/items/ec46d197-3d75-45d9-9f56-7e7fbaa26c3b.

[25] Susann Hänsch. *Untersuchung des Einflusses geometrischer Parameter auf die Kennfeldbreite radialer Turboverdichter*. Diplomarbeit, Technische Universität Dresden, 2010.

[26] David Japikse. Turbomachinery performance modeling. *SAE Technical Paper*, 2009-01-0307, 2009. doi:10.4271/2009-01-0307.

[27] Michael V. Casey and Thomas M. Fesich. The efficiency of turbocharger compressors with diabatic flows. *Journal of Engineering for Gas Turbines and Power*, 132(7), 2010. doi:10.1115/1.4000300.

[28] Manuel Haug. *Entwicklung eines diabaten Verdichterprüfstandmodells*. Masterthesis, Universität Stuttgart, Stuttgart, 2024.

[29] Rainer Kurz, Russell K. Marechale, Edward J. Fowler, Min Ji, and Michael J. Cave. Operation of centrifugal compressors in choke conditions. In *Asia Turbomachinery & Pump Symposium*. 2016. doi:10.21423/R16D89.

[30] Flexware Inc. Monitoring choke. URL: https://www.flexwareinc.com/inforeq_files/monitoringchoke.pdf.

[31] Ronald C. Pampreen. *Compressor surge and stall*. Concepts ETI, Norwich, Vt., 1. edition, 1993.

[32] E. M. Greitzer. Surge and rotating stall in axial flow compressors—part i: Theoretical compression system model. *Journal of Engineering for Power*, 98(2):190–198, 1976. doi:10.1115/1.3446138.

[33] D. A. Fink, N. A. Cumpsty, and E. M. Greitzer. Surge dynamics in a free-spool centrifugal compressor system. *Journal of Turbomachinery*, 114(2):321–332, 1992. doi:10.1115/1.2929146.

[34] Klaus H. Lüdtke. *Process Centrifugal Compressors: Basics, Function, Operation, Design, Application*. Springer Berlin Heidelberg, Berlin, Heidelberg, 2004. doi:10.1007/978-3-662-09449-5.

[35] Wenli Wang, Ce Yang, Chenxing Hu, and Hang Zhang. Investigation of tip leakage flow unsteadiness and rotating instability in a centrifugal compressor impeller. *Proceedings of the Institution of Mechanical Engineers, Part D: Journal of Automobile Engineering*, 236(4):621–638, 2022. doi:10.1177/09544070211025902.

[36] Ahsanul Karim, Matthew Mckean, Rick Dehner, Ahmet Selamet, Chris Tiernan, Anthony Morelli, Keith Miazgowicz, and Ted Mull. Turbocharger centrifugal compressor casing treatment for improved bpf noise using computational fluid dynamics. *SAE Technical Paper*, 2019-01-1484, 2019. doi:10.4271/2019-01-1484.

[37] *The Jet Engine*. Rolls-Royce plc, Derby, 5. edition, 1996.

[38] Simon Bareiß. *Circumferential groove casing treatments in centrifugal compressor aerodynamics*. Phd thesis, Universität Stuttgart, 2021. doi:10.18419/OPUS-11664.

[39] H. W. Emmons, C. E. Pearson, H. P. Grant, H. W. Emmons, C. E. Pearson, and H. P. Grant. Compressor surge and stall propagation. *Journal of Fluids Engineering*, 77(4):455–467, 1955. doi:10.1115/1.4014389.

[40] D. A. Hoying, C. S. Tan, Huu Duc Vo, and E. M. Greitzer. Role of blade passage flow structurs in axial compressor rotating stall inception. *Journal of Turbomachinery*, 121(4):735–742, 1999. doi:10.1115/1.2836727.

[41] Sungho Yoon and Patricia Cargill. Casing treatment: Its potential and limitations. *Journal of Turbomachinery*, 145(4), 2023. doi:10.1115/1.4055928.

[42] Ce Yang, Wenli Wang, Hanzhi Zhang, Yanzhao Li, Ding Tong, Changmao Yang, and Weilin Yi. Investigation of stall process in a centrifugal compressor with a volute under transonic conditions. In *Proceedings of the ASME Turbo Expo 2019: Turbomachinery Technical Conference and Exposition 2019*. ASME, 2019. doi:10.1115/GT2019-90713.

[43] Ce Yang, Yingjun Wang, Ding Tong, Changmao Yang, and Yanzhao Li. Stall inception induced by the volute tongue at centrifugal compressor inlet. In *Proceedings of the Institution of Mechanical Engineers, Part G: Journal of Aerospace Engineering*, volume 231, pages 931–940. Sage Journals, 2017. doi:10.1177/0954410016645127.

[44] Zhenhong Sun, Xinqian Zheng, Zelin Linghu, Tomoki Kawakubo, Hideaki Tamaki, Baotong Wang, and Zhenzhong Sun. Influence of volute design on flow field distortion and flow stability of turbocharger centrifugal compressors. *Proceedings of the Institution of Mechanical Engineers, Part D: Journal of Automobile Engineering*, 233(3):484–494, 2019. doi:10.1177/0954407017746281.

[45] Xinqian Zheng, Lei Jin, Hideaki Tamaki, and Xinqian Zheng. Influence of volute distortion on the performance of turbocharger centrifugal compressor with vane diffuser. *Science China Technological Sciences*, 56(11):2778–2786, 2013. doi:10.1007/s11431-013-5326-y.

[46] Johannes Bühler, Sebastian Leichtfuß, Heinz-Peter Schiffer, Thomas Lischer, and Simon Raabe. Surge limit prediction for automotive air-charged systems. *International Journal of Turbomachinery, Propulsion and Power*, 4(4):34, 2019. doi:10.3390/ijtpp4040034.

[47] Tobias Haeckel, Dominik Paul, Sebastian Leichtfuß, Heinz-Peter Schiffer, and Werner Eißler. Determination of a numerical surge limit by means of an enhanced greitzer compressor model. *International Journal of Turbomachinery, Propulsion and Power*, 8(4):48, 2023. doi:10.3390/ijtpp8040048.

[48] Beat Ribi. *Radialverdichter im Instabilitätsbereich*. Phd thesis, ETH Zurich, 1996. doi:10.3929/ETHZ-A-001696274.

[49] Katherine H. Powers, Ian J. Kennedy, Chris J. Brace, Paul A. Milewski, and Colin D. Copeland. Development and validation of a model for centrifugal compressors in reversed flow regimes. In *Proceedings of the ASME Turbo Expo 2020: Turbomachinery Technical Conference and Exposition*, volume 8, [S.l.], 2021. ASME. doi:10.1115/GT2020-16005.

[50] Antoine Godard, Isabelle Trebinjac, and Mathieu Roumeas. Experimental characterization of the surge onset in a turbo-compressor for fuel cell application. In European Turbomachinery Society, editor, *12th European Conference on Turbomachinery Fluid dynamics & Thermodynamics*, 2017. doi:10.29008/ETC2017-040.

[51] Katherine H. Powers, Ian J. Kennedy, Jamie Archer, Paul Eynon, John Horsley, Chris J. Brace, Colin D. Copeland, and Paul A. Milewski. A new first-principles model to predict mild and deep surge for a centrifugal compressor. *Energy*, 244(Part B), 2022. doi:10.1016/j.energy.2021.123050.

[52] E. M. Greitzer. Surge and rotating stall in axial flow compressors—part ii: Experimental results and comparison with theory. *Journal of Engineering for Power*, 98(2):199–211, 1976. doi:10.1115/1.3446139.

[53] Maria Esperanza Barrera-Medrano, Peter Newton, Ricardo Martinez-Botas, Srithar Rajoo, Isao Tomita, and Seiichi Ibaraki. Effect of exit pressure pulsation on the performance and stability limit of a turbocharger centrifugal compressor. In *Proceedings of the ASME Turbo Expo 2016: Turbomachinery Technical Conference and Exposition*. ASME, 2016. doi:10.1115/GT2016-56109.

[54] Johannes Buehler. *Über den Einfluss aerodynamischer Effekte und systemischer Größen auf das Kennfeld von Radialverdichtern*. Phd thesis, Technische Universität Darmstadt, 2020. doi:10.25534/tuprints-00011456.

[55] C. Schäfer, I. Sandor, M. Klaus, and R. Baar. Influence of the hot gas test bench piping system on the surge line of an automotive turbocharger compressor. In *12th European Conference on Turbomachinery Fluid Dynamics and Thermodynamics*. European Turbomachinery Society, 2017.

[56] M. Whittlesea and E. Roberts. Turbo charger compressor inlet and outlet pipe length and volume, and the effects on the characteristics and location of surge. In *The 12th International Conference on Turbochargers and Turbocharging*, pages 47–65. Institution of Mechanical Engineers, 2016.

[57] José. Galindo, Héctor. Climent, Carlos. Guardiola, and Andrés. Tiseira. On the effect of pulsating flow on surge margin of small centrifugal compressors for automotive engines. *Experimental Thermal and Fluid Science*, 33(8):1163–1171, 2009. doi:10.1016/j.expthermflusci.2009.07.006.

[58] Klaus Brun, Sarah Simons, and Rainer Kurz. The impact of reciprocating compressor pulsations on the surge margin of centrifugal compressors. In *Proceedings of the ASME Turbo Expo 2016: Turbomachinery Technical Conference and Exposition*, volume 9: Oil and Gas Applications; Supercritical CO2 Power Cycles; Wind Energy. ASME, 2016. doi:10.1115/GT2016-56025.

[59] Mengying Shu, Mingyang Yang, Kaiyue Zhang, Kangyao Deng, Bijie Yang, and Ricardo F. Martinez-Botas. Experimental study on performance of centrifugal compressor exposed to pulsating backpressure. *Aerospace Science and Technology*, 95, 2019. doi:10.1016/j.ast.2019.105450.

[60] Mengying Shu, Bijie Yang, Mingyang Yang, Ricardo F. Martinez-Botas, Deng Kangyao, and Kangyao Deng. Investigation on the unsteadiness of centrifugal compressor exposed to pulsating backpressure. *Proceedings of the Institution of Mechanical Engineers, Part D: Journal of Automobile Engineering*, 235(8):2212–2225, 2021. doi:10.1177/0954407020984593.

[61] Mengying Shu, Bijie Yang, Mingyang Yang, Ricardo F. Martinez-Botas, and Weilin Zhuge. Compressor stability at pulsating condition via gas dynamics responses analysis. *Journal of Engineering for Gas Turbines and Power*, 144(2), 2022. doi:10.1115/1.4052664.

[62] Mingyang Yang, Mengying Shu, Xingcheng Wang, Kangyao Deng, Bijie Yang, and Ricardo Martinez-Botas. Rotor-stator aerodynamic interaction of centrifugal compressor at pulsating backpressure conditions. *International Journal of Heat and Fluid Flow*, 96:109009, 2022. doi:10.1016/j.ijheatfluidflow.2022.109009.

[63] C. Rodgers. Centrifugal compressor inlet guide vanes for increased surge margin. *Journal of Turbomachinery*, 113(4):696–702, 1991. doi:10.1115/1.2929136.

[64] Luca Mantelli, David Tucker, and Mario Luigi Ferrari. Dynamic effect of cold-air bypass valve for compressor surge recovery and prevention in fuel cell gas turbine hybrid systems. In *SUPEHR'19*, volume 113. doi:10.1051/e3sconf/201911302014.

[65] Neil Figurella, Rick Dehner, Ahmet Selamet, Keith Miazgowicz, Ahsanul Karim, and Ray Host. Effect of aerodynamically induced pre-swirl on centrifugal compressor acoustics and performance. *SAE International Journal of Passenger Cars - Mechanical Systems*, 8(3):995–1002, 2015. doi:10.4271/2015-01-2307.

[66] J. E. Ffowcs Williams and X. Y. Huang. Active stabilization of compressor surge. *Journal of Fluid Mechanics*, 204(-1):245, 1989. doi:10.1017/S0022112089001746.

[67] Matthieu Gancedo, Ephraim Gutmark, and Erwann Guillou. Piv measurements of the flow at the inlet of a turbocharger centrifugal compressor with recirculation casing treatment near the inducer. *Experiments in Fluids*, 57(2), 2016. doi:10.1007/s00348-015-2105-5.

[68] Xuwen Qiu, Eric M. Krivitzky, and Peter Bollweg. Meanline modeling of ported shroud turbocharger compressor. In *Proceedings of the ASME Turbo Expo 2012: Turbomachinery Technical Conference and Exposition*, volume 8: Turbomachinery, Parts A, B, and C, pages 725–733. ASME, 2012. doi:10.1115/GT2012-68915.

[69] Bernhard Semlitsch, Jyothish Kumar V, Mihai Mihaescu, Laszlo Fuchs, Ephraim Gutmark, and Matthieu Gancedo. Numerical flow analysis of a centrifugal compressor with ported and without ported shroud. *SAE Technical Paper*, 2014-01-1655, 2014. doi:10.4271/2014-01-1655.

[70] Erwann Guillou, Matthieu Gancedo, Ephraim Gutmark, and Ashraf Mohamed. Piv investigation of the flow induced by a passive surge control method in a

radial compressor. *Experiments in Fluids*, 53(3):619–635, 2012. doi:10.1007/s00348-012-1310-8.

[71] Christoph Schäfer, Mathias Bogner, Jan Ehrhard, and Matthias Dunzer. Aerodynamic design of a ported shroud casing treatment for a turbocharger compressor of a miller-cycle gasoline engine. In *Proceedings of the ASME Turbo Expo 2018: Turbomachinery Technical Conference and Exposition 2018*, volume 8: Microturbines, Turbochargers, and Small Turbomachines; Steam Turbines, page V008T26A001. ASME, 2018. doi:10.1115/GT2018-75033.

[72] Mingyang Yang, Xinqian Zheng, Yangjun Zhang, Takahiro Bamba, Hideaki Tamaki, Joern Huenteler, and Zhigang Li. Stability improvement of high-pressure-ratio turbocharger centrifugal compressor by asymmetric flow control: Part i—non-axisymmetric flow in centrifugal compressor. In *Proceedings of the ASME Turbo EXPO 2010: Power for Land, Sea, and Air*, volume 7: Turbomachinery, Parts A, B, and C, pages 1891–1902. ASME, 2010. doi:10.1115/GT2010-22581.

[73] Xinqian Zheng, Yangjun Zhang, Mingyang Yang, Takahiro Bamba, and Hideaki Tamaki. Stability improvement of high-pressure-ratio turbocharger centrifugal compressor by asymmetric flow control: Part ii—non-axisymmetric self recirculation casing treatment. In *Proceedings of the ASME Turbo EXPO 2010: Power for Land, Sea, and Air*, volume 7: Turbomachinery, Parts A, B, and C, pages 1903–1912. ASME, 2010. doi:10.1115/GT2010-22582.

[74] Michael Wöhr, Peter Wahl, Markus Schneid, Andreas Dillmann, and Markus Müller. Compressor development at daimler trucks. In *23. Aufladetechnische Konferenz 2018*, pages 143–165, 2018.

[75] Thomas Hildebrandt, Peter Thiel, and Ingolf Lehmann. Entwicklung eines leistungsgesteigerten radialverdichters mit abgasturbolader: Von der cfd basierten optimierung mit fine / turbo bis zum serienreifen prototyp im hause kbb. In *14. Aufladetechnische Konferenz*, pages 389–406. Dresden, 2009.

[76] Thomas Hildebrandt, Leonhard Gresser, and Mario Sievert. Kennfeldverbreiterung eines radialverdichters für abgasturbolader durch multidisziplinäre cfd-fem-optimierung mit fine /turbo. In *16. Aufladetechnische Konferenz*, pages 131–149. Dresden, 2011.

[77] Anna Pietrenko-Dabrowska and Slawomir Koziel. *Response Feature Technology for High-Frequency Electronics. Optimization, Modeling, and Design Automation*. Springer International Publishing, Cham, 2024. doi:10.1007/978-3-031-43845-5.

[78] Johannes Will and Thomas Most. Metamodell of optimized prognosis (mop) - an automatic approach for user friendy parameter optimization. In *Weimar Optimization and Stochastic Days 6.0*, 2009. URL: https://library.dynardo.de/fileadmin/Material_Dynardo/bibliothek/WOST_5.0/WOST_5_Paper_Most.pdf.

[79] Dynardo GmbH. Methods for multi-disciplinary optimization and robustness analysis: Optislang user manual.

[80] Ansys inc. Optislang user manual.

[81] Weifei Hu. *Design Optimization Under Uncertainty*. Springer International Publishing and Imprint Springer, Cham, 1st edition, 2023. doi:10.1007/978-3-031-49208-2.

[82] Karl Siebertz, David van Bebber, and Thomas Hochkirchen. *Statistische Versuchsplanung*. Springer Berlin Heidelberg, Berlin, Heidelberg, 2017. doi:10.1007/978-3-662-55743-3.

[83] Thomas Most and Johannes Will. Sensitivity analysis using the meta-model of optimal prognosis. In *Weimar Optimization and Stochastic Days 8.0*, 2011. URL: https://library.dynardo.de/fileadmin/Material_Dynardo/WOST/Paper/wost8.0/Paper_Most.pdf.

[84] John D. Denton. Some limitations of turbomachinery cfd. In *Proceedings of the ASME Turbo EXPO 2010: Power for Land, Sea, and Air*, pages 735–745. ASME, 2010. doi:10.1115/GT2010-22540.

[85] KS Engineers. Tornado user guide.

[86] Daimler AG. Analyse und experimentelle betrachtung zur absicherung der vermessungsqualität von turboladern an heißgasprüfständen: internal document.

[87] Engine Power Test Code Committee. Turbocharger gas stand test code: J1826 / 202204, 2022.

[88] Silvia Marelli, Giulio Marmorato, and Massimo Capobianco. Evaluation of heat transfer effects in small turbochargers by theoretical model and its experimental validation. *Energy*, 112:264–272, 2016. doi:10.1016/j.energy.2016.06.067.

[89] Xunan Gao. *Model of aerodynamics and heat transfer of a turbocharger*. Phd thesis, 2019. doi:10.14279/depositonce-9140.

[90] José R. Serrano, Pablo Olmeda, Francisco J. Arnau, and Vishnu Samala. A holistic methodology to correct heat transfer and bearing friction losses from hot turbocharger maps in order to obtain adiabatic efficiency of the turbomachinery. *International Journal of Engine Research*, 21(8):1314–1335, 2020. doi:10.1177/1468087419834194.

[91] J. R. Serrano, P. Olmeda, A. Páez, and F. Vidal. An experimental procedure to determine heat transfer properties of turbochargers. *Measurement Science and Technology*, 21(3):035109, 2010. doi:10.1088/0957-0233/21/3/035109.

[92] Economic Commission for Europe of the United Nations. Regulation no 49- uniform provisions concerning the measures to be taken against the emission of gaseous and particulate pollutants from compression-ignition engines and positive ignition engines for use in vehicles: R049r4e. URL: https://eur-lex.europa.eu/eli/reg/2013/49(2)/oj/eng.

[93] International Organization for Standardisation. Iso 15550:2016: Internal combustion engines - determination and method for the measurement of engine power - general requirements, 2016. URL: https://www.iso.org/standard/70030.html.

[94] Elias Sundström, Bernhard Semlitsch, and Mihai Mihăescu. Similarities and differences concerning flow characteristics in centrifugal compressors of different size. In *Proceedings ofthe 5th International Conference on Jets, Wakes and Separated Flows*, volume 185, pages 457–464. doi:10.1007/978-3-319-30602-5_57.

[95] Tuncer Cebeci and Jean Cousteix. *Modeling and Computation of Boundary-Layer Flows*. Springer Berlin Heidelberg, Berlin, Heidelberg, 2005. doi:10.1007/3-540-27624-6.

[96] Herbert Oertel and Eckart Laurien. *Numerische Strömungsmechanik: Grundgleichungen, Lösungsmethoden, Softwarebeispiele*. Studium Technik. Vieweg, Braunschweig, 2., neu bearb. edition, 2003.

[97] Bertrand Kerres, Sergio Sanz, E. Sundstrom, and Mihai Mihaescu. A comparison of performance predictions between 1d models and numerical data for a turbocharger compressor. In *12th European Conference on Turbomachinery Fluid Dynamics and Thermodynamics*. European Turbomachinery Society, 2017. doi:10.29008/ETC2017-350.

[98] Siemens. Simcenter star-ccm+ 2410 user guide.

[99] Matthias Abel, Torsten Palenschat, Peter Wahl, Galin Nakov, Michael Benz, Börge Nielsen, and Markus Müller. Automated turbocharger development for future engine generations at daimler truck ag. In Johannes Liebl, editor, *Verbrennungsmotoren und Hybridantriebe : 15. Int. MTZ-Fachtagung Großmotoren*, pages 273–293, Wiesbaden, Germany and Heidelberg, 2021. Springer Vieweg. doi:10.1007/978-3-658-34362-0_16.

[100] Ernesto Casartelli, Luca Mangani, David Roos Launchbury, and Armando Del Rio. Application of advanced rans turbulence models for the prediction of turbomachinery flows. *Journal of Turbomachinery*, 144(1), 2022. doi:10.1115/1.4051938.

[101] Elias Sundström, Bernhard Semlitsch, and Mihai Mihaescu. Assessment of the 3d flow in a centrifugal compressor using steady-state and unsteady flow solvers. *SAE Technical Paper*, 2014-01-2856, 2014. doi:10.4271/2014-01-2856.

[102] Elias Sundström, Bertrand Kerres, Sergio Sanz, and Mihai Mihăescu. On the assessment of centrifugal compressor performance parameters by theoretical and computational models. In *Proceedings of the ASME Turbo Expo 2017: Turbomachinery Technical Conference and Exposition*. ASME, 2017. doi:10.1115/GT2017-65230.

[103] Philippe R. Spalart. Detached-eddy simulation. *Annual Review of Fluid Mechanics*, 41(1):181–202, 2009. doi:10.1146/annurev.fluid.010908.165130.

[104] Ibrahim Shahin, Mohamed Gadala, Mohamed Alqaradawi, and Osama Badr. Large eddy simulation for a deep surge cycle in a high-speed centrifugal compressor with vaned diffuser. *Journal of Turbomachinery*, 137(10), 2015. doi:10.1115/1.4030790.

[105] Rick Dehner and Ahmet Selamet. Physics of deep surge in an automotive turbocharger centrifugal compression system. *Journal of Engineering for Gas Turbines and Power*, 141(6), 2019. doi:10.1115/1.4042303.

[106] Guillaume Després, Ghislaine Ngo Boum, Francis Leboeuf, David Chalet, Pascal Chesse, and Alain Lefebvre. Simulation of near surge instabilities onset in a turbocharger compressor. *Proceedings of the Institution of Mechanical Engineers, Part A: Journal of Power and Energy*, 227(6):665–673, 2013. doi:10.1177/0957650913495537.

[107] David Schwarz, Vivek Harsha, Somasekhar Reddy Dantla, Thikshana Reddy Yeruva, Galin Nakov, and Ricardo Martinez-Botas. A novel method for predicting compressor performance in the vicinity of surge. In *THIESEL 2024 Conference on Thermo- and Fluid Dynamics Processes for clean Propulsion Powerplants*, pages 510–521, 2024. doi:10.4995/Thiesel.2024.679601.

[108] Zitian Niu, Zhenzhong Sun, Baotong Wang, and Xinqian Zheng. Effects of nonaxisymmetric volute on rotating stall in the vaneless diffuser of centrifugal compressors. *Journal of Engineering for Gas Turbines and Power*, 144(5), 2022. doi:10.1115/1.4053389.

[109] Yoshihiro Hayashi and Teng Cao. An investigation of non-linear surge characteristic in a high-speed centrifugal compressor. *Journal of Turbomachinery*, 145(5), 2023. doi:10.1115/1.4056089.

[110] Bernhard Semlitsch, V. Jyothishkumar, Mihai Mihaescu, Laszlo Fuchs, and Ephraim J. Gutmark. Investigation of the surge phenomena in a centrifugal compressor using large eddy simulation. In *Proceedings of the ASME 2013 International Mechanical Engineering Congress and Exposition*. doi:10.1115/IMECE2013-66301.

[111] H. Mohtar, P. Chesse, D. Chalet, J.-F. Hetet, and A. Yammine. Effect of diffuser and volute on turbocharger centrifugal compressor stability and performance: Experimental study. *Oil & Gas Science and Technology – Revue d'IFP Energies nouvelles*, 66(5):779–790, 2011. doi:10.2516/ogst/2011139.

[112] Silvia Marelli, Chiara Carraro, and Massimo Capobianco. Effect of pulsating flow characteristics on performance and surge limit of automotive turbocharger compressors. *SAE International Journal of Engines*, 5(2):596–601, 2012. doi:10.4271/2012-01-0715.

[113] Mingyang Yang, Mengying Shu, Bijie Yang, Ricardo F. Martinez-Botas, Kangyao Deng, and Ricardo Martinez-Botas. Unsteady response of performance for centrifugal compressor under pulsating backpressure condition. *Aerospace Science and Technology*, 126:107589, 2022. doi:10.1016/j.ast.2022.107589.

[114] Wolfgang Krüger, Jens Kleffel, Philipp Dietrich, and David Koch. 10.7-l daimler hd truck engine for euro vi and tier 4. *MTZ worldwide*, 73(12):4–10, 2012. doi:10.1007/s38313-012-0246-y.

[115] David Schwarz. The role of metamodels in heavy-duty turbocharger compressor testing: How metamodels ensure high-quality measurement data. In *21st Weimar Optimization and Stochastic Day 2024*, Weimar, 2024.

[116] Galindo J., J. R. Serrano, H. Climent, and A. Tiseira. Experiments and modelling of surge in small centrifugal compressor for automotive engines. *Experimental Thermal and Fluid Science*, 32(3):818–826, 2008. URL: `https://doi.org/10.1016/j.expthermflusci.2007.10.001`.

[117] Karim Gharaibeh. *Experiments and modelling of surge in turbocharger compressors*. Phd thesis, Imperial College London, 2020. `doi:10.25560/99659`.

[118] G. Theotokatos and N. P. Kyrtatos. Diesel engine transient operation with turbocharger compressor surging. *SAE Technical Paper*, 2001-01-1241, 2001. `doi:10.4271/2001-01-1241`.

[119] Rick Dehner, Ahmet Selamet, Philip Keller, and Michael Becker. Simulation of mild surge in a turbocharger compression system. *SAE International Journal of Engines*, 3(2):197–212, 2010. `doi:10.4271/2010-01-2142`.

[120] J. A. Nelder and R. Mead. A simplex method for function minimization. *The Computer Journal*, 7(4):308–313, 1965. `doi:10.1093/comjnl/7.4.308`.

[121] Gamma Technologies LLC. Gt suite flow theory manual.

[122] F. K. Moore and E. M. Greitzer. A theory of post-stall transients in axial compression systems: Part i—development of equations. *Journal of Engineering for Gas Turbines and Power*, 108(1):68–76, 1986. `doi:10.1115/1.3239887`.

[123] Bijie Yang and Ricardo Martinez-Botas. Turbodyna: Centrifugal/centripetal turbomachinery dynamic simulator and its application on a mixed flow turbine. *Journal of Engineering for Gas Turbines and Power*, 141(10), 2019. `doi:10.1115/1.4044681`.

[124] Katherine H. Powers. *Development and Validation of a Mathematical Model for Surge in Radial Compressors*. Phd thesis, University of Bath, Bath, 2021. URL: `https://purehost.bath.ac.uk/ws/portalfiles/portal/220577115/PhD_Thesis_KHP_05_2021_Redacted.pdf`.

[125] Vincenzo de Bellis, Fabio Bozza, Silvia Marelli, and Massimo Capobianco. Experimental investigation and 1d simulation of a turbocharger compressor close to surge operation. *SAE International Journal of Engines*, 8(4):1866–1878, 2015. `doi:10.4271/2015-01-1720`.

[126] Vincenzo de Bellis, Fabio Bozza, Silvia Marelli, and Massimo Capobianco. Experimental investigation and 1d simulation of a turbocharger compressor close to surge operation. *SAE International Journal of Engines*, 8(4):1866–1878, 2015. `doi:10.4271/2015-01-1720`.

[127] Bijie Yang, Mengying Shu, Ricardo Martinez-Botas, and Mingyang Yang. Turbodyna: A generic one-dimensional dynamic simulator for radial turbomachinery.

Journal of Engineering for Gas Turbines and Power, 144(9), 2022. doi:10.1115/1.4055018.

[128] Katherine H. Powers, Chris J. Brace, Chris J. Budd, Colin D. Copeland, and Paul A. Milewski. Modelling axisymmetric centrifugal compressor characteristics from first principles. In *Proceedings of the ASME Turbo Expo 2019: Turbomachinery Technical Conference and Exposition 2019*, volume 2A: Turbomachinery. ASME, 2019. doi:10.1115/GT2019-90091.

[129] Rene Hunziker. *Einfluss der Diffusorgeometrie auf die Instabilitätsgrenze des Radialverdichters*. Phd thesis, ETH Zurich, 1993.

A. Radial Equilibrium Theory

We assume an adiabatic compression and reshape to pressure ratio:

$$\frac{T_2}{T_1} = \left(\frac{P_2}{P_1}\right)^{\left(\frac{\gamma-1}{\gamma}\right)} \tag{A.1}$$

$$\frac{P_2}{P_1} = \left(\frac{T_2}{T_1}\right)^{\left(\frac{\gamma}{\gamma-1}\right)} = \left(\frac{T_1 + dT}{T_1}\right)^{\left(\frac{\gamma}{\gamma-1}\right)} = \left(1 + \frac{dT}{T_1}\right)^{\left(\frac{\gamma}{\gamma-1}\right)} \tag{A.2}$$

We know that:

$$dh = c_p dT \tag{A.3}$$

which leads to:

$$\frac{P_2}{P_1} = \left(1 + \frac{dh}{c_p T_1}\right)^{\left(\frac{\gamma}{\gamma-1}\right)} \tag{A.4}$$

We now consider Gibbs equation and apply it over the impeller radius:

$$\frac{dh}{dr} = \frac{1}{\rho}\frac{dp}{dr} + T\frac{ds}{dr} \tag{A.5}$$

We then construct the balance of pressure and inertial forces on a fluid element in the impeller. We conclude, that, in case of axisymmetric flow, the balance is given by the following equation.

$$-\frac{1}{\rho}\frac{dp}{dr} = C_r\frac{dC_r}{dr} + C_x\frac{dC_r}{dx} - \frac{C_\theta^2}{r} \tag{A.6}$$

This is now substituted into aforementioned equation.

$$\frac{dh}{dr} = T\frac{ds}{dr} - C_x\frac{dC_r}{dx} - C_r\frac{dC_r}{dr} + \frac{C_\theta^2}{r} \tag{A.7}$$

We consider the entropy change negligible compared to the other terms. This reduces the equation to:

$$\frac{dh}{dr} = -C_x\frac{dC_r}{dx} - C_r\frac{dC_r}{dr} + \frac{C_\theta^2}{r} \tag{A.8}$$

Since the mass flow is zero, C_x and C_r are zero. This further simplifies the equation to:

$$\frac{dh}{dr} = \frac{C_\theta^2}{r} \tag{A.9}$$

We substitute C_θ with ωr:

$$\frac{dh}{dr} = \omega^2 r \tag{A.10}$$

We now integrate over r to get the enthalpy change from one to two:

$$h_{12} = \int_1^2 \omega^2 r dr = \frac{\omega^2}{2}(r_2^2 - r_1^2) \tag{A.11}$$

Finally, we combine the derived enthalpy equation with A.4.

$$\frac{P_2}{P_1} = \left(1 + \frac{\omega^2}{2c_p T_1}(r_2^2 - r_1^2)\right)^{(\frac{\gamma}{\gamma-1})} \tag{A.12}$$

B. Program Flow Chart- Compressor Performance Prediction Surrogate Model

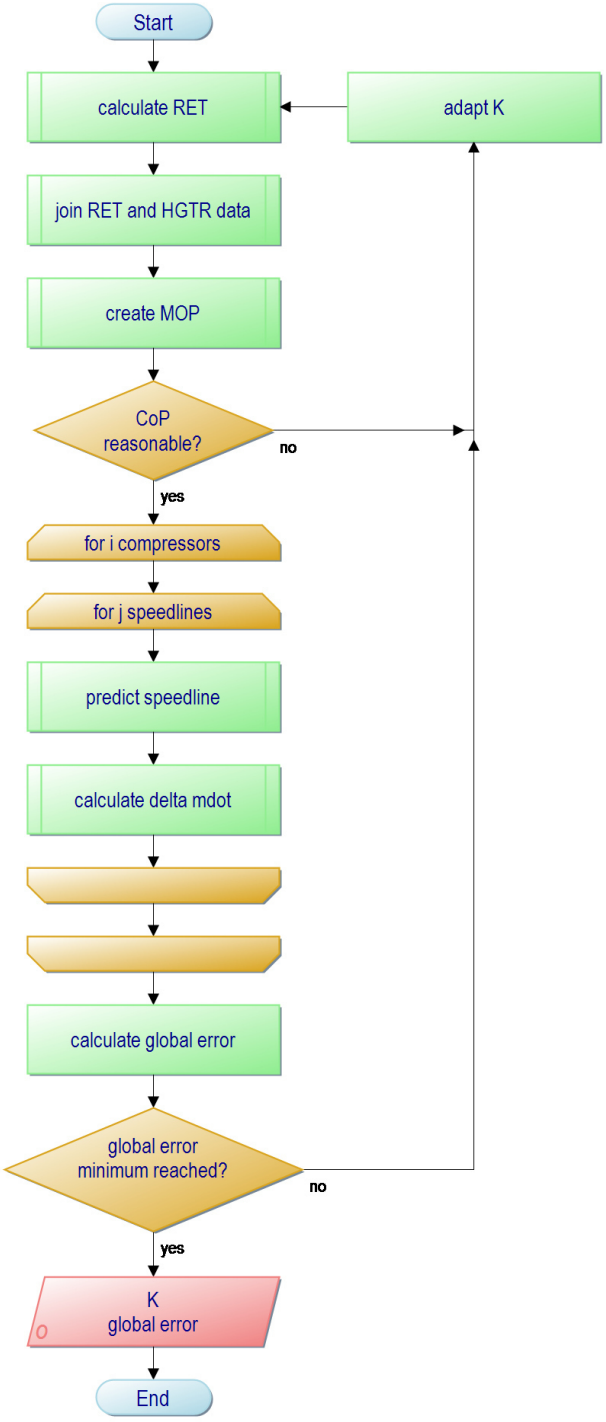


Figure B.1.: Surrogate model optimization flow chart

C. False Color Comparison G1849, G675

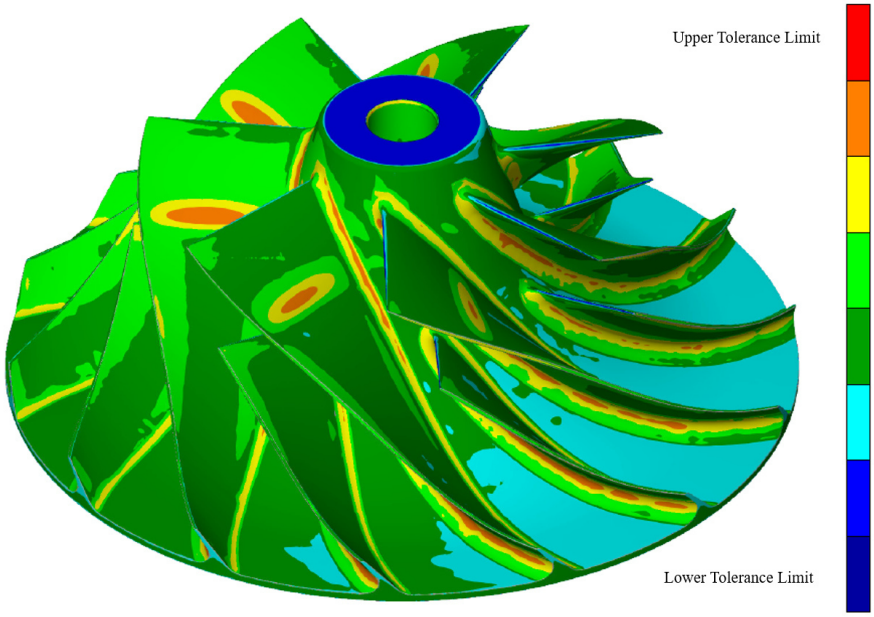


Figure C.1.: false color comparison G1849 Prototype vs. CAD

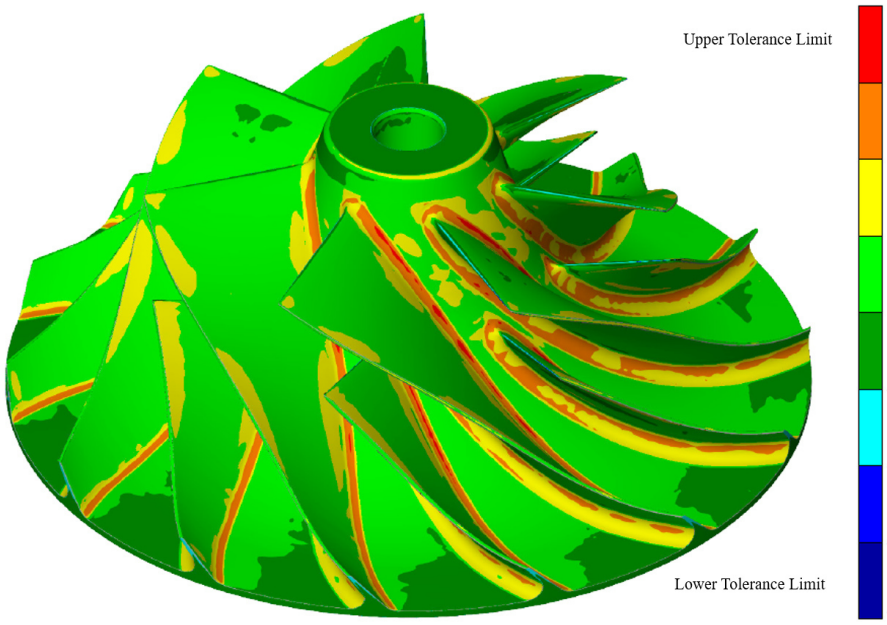


Figure C.2.: false color comparison G675 Prototype vs. CAD